# Analyses of canopy photosynthesis derived from three-dimensional model simulations of sun-induced chlorophyll fluorescence

Sicong Gao

A thesis submitted in fulfilment of the requirements for the degree of Doctor of Philosophy

Faulty of Science

University of Technology Sydney

January 2020

# Certificate of original authorship

I certify that the work in this thesis has not previously been submitted for a degree nor has it been submitted as part of requirements for a degree except as fully acknowledged within the text.

I also certify that the thesis has been written by me. Any help that I have received in my research work and the preparation of the thesis itself has been acknowledged. In addition, I certify that all information sources and literature used are indicated in the thesis. This research is supported by Australian Government Research Training Program.

Signature of student: Production Note: Signature removed prior to publication.

Date: 31-01-2020

# Acknowledgements

This research is supported by an Australian Government Research Training Program.

First of all, I would like to thank my principle supervisor Distinguished Professor Alfredo Huete for his support during my three and a half years of PhD study. My major was not remote sensing before I came to UTS. I truly appreciate Professor Huete's trust and guide to enter the remote sensing area. He offered a free research environment and his professional suggestions encouraged me to discovery scientific questions.

Secondly, I would like to say thank you to Dr. Hideki Kobayashi for providing the FLiES model and giving suggestions to my study, Professor Jim Tang for providing field measured SIF data at Harvard forest and Professor Elise Pendall for providing the LiDAR data.

Also, many thanks to Professor Qiang Yu, Professor Derek Eamus, Dr. James Cleverly, Dr. Xuanlong Ma, Dr. Zunyi Xie, Dr. Xiaolu Tang and Dr. Weiwei Liu for their help and share of their experience. Thanks to Jie He, Dr. Wenjie Zhang, Song Leng, Dr. Xunhe Zhang, Dr. Qinggaozi Zhu and Dr. Zheyuan Du, Minxi Zhang, Hong Zhang for their encouragement, delicious food and joyful mahjong parties. I am also grateful to my team members Dr. Rakhesh Devadas, Dr. Leandro Giovannini, Ekena Rangel, Dr. Nguyen Ngoc Tran, and Dr. Paras Sidiqui for their help and all my friends in China, Dr. Xin Li, Chao Zhang, Weihong Wang, and Dr. Xianghu Ji for encouraging me to finish my study.

Additionally, I would like to especially thank my wife Man Bao. Thank you for your love, trust, encouragement and 100% support. Every time when I am stressful, you always stay with me and give me confidence. And our pet Mascarpone (the cutest and most gorgeous cat in the world), thank you for waking me up early in the morning and being my motivation to work hard.

Lastly, I would like to deeply thank my parents for their cultivation and education. Your love gives me the courage to face all difficulties in my life and get through the tough times. And my brother and his wife, thank you for your support throughout my study.

# Publications

Wu, J., Kobayashi, H., Stark, **S.C.**, Meng, R., Guan, K., Tran, N.N., **Gao, S.**, Yang, W., Restrepo-Coupe, N., Miura, T. and Oliviera, R.C., 2018. Biological processes dominate seasonality of remotely sensed canopy greenness in an Amazon evergreen forest. *New Phytologist*, *217*(4), pp.1507-1520.

# Table of contents

# List of Figures

# List of Tables

# Abbreviations

| | |
|---|---|
| 1D | 1 Dimensional |
| 3D | 3 Dimensional |
| APAR | Absorbed Photosynthetic Active Radiation |
| Biome-BGC | Biome BioGeochemical Cycles |
| BRDF | Bidirectional Reflectance Distribution Function |
| Cab | total chlorophyll content |
| Cca | Carotenoid content |
| Cd | leaf dry matter |
| CHM | Canopy Height Model |
| $CI_{green}$ | green Chlorophyll Index |
| Cw | leaf water thickness |
| DART | Discrete Anisotropic Radiative Transfer |
| EF-matrix | Excited Fluorescence Matrices |
| ESA | European Space Agency |
| EVI | Enhanced Vegetation Index |
| FLD | Fraunhofer Line Discrimination |
| FLiES | Forest light environmental simulator |
| FluorWPS | Fluorescence model with Weighted Photon Spread method |
| FOV | Field Of View |
| fPAR | Fraction of Photosynthetically Active Radiation |
| fqeI | fluorescence quantum efficiency for photosystem I |
| fqeII | fluorescence quantum efficiency for photosystem II |
| FVC | Fraction of Vegetation Cover |
| GOME-2 | Global Ozone Monitoring Experiment–2 |
| GOSAT | Greenhouse Gases Observing Satellite |
| GPP | Gross Primary Productivity |
| GPR | Gaussian Processes Regression |
| IA | Inner Antenna |
| LAI | Leaf Area Index |
| IGBP | International Geosphere-Biosphere Programme |

| | |
|---|---|
| LiDAR | Light Detection And Ranging |
| LUE | Light Use Efficiency |
| MODIS | MOderate resolution Imaging Spectroradiometer |
| N | leaf structure |
| NEE | Net Ecosystem Exchange |
| NDVI | Normalized Difference Vegetation Index |
| NPQ | NonPhotochemical Quenching |
| OA | Outer Antenna |
| OCO-2 | Orbiting Carbon Observatory-2 |
| PAR | Photosynthetic Active Radiation |
| PRI | Photochemical Reflectance Index |
| PPFD | Photosynthetic Photon Flux Density |
| PSI | Photosystem I |
| PSII | Photosystem II |
| RBF | Radial-Basis Function |
| RMSE | Root Mean Square Error |
| RTM | Radiation Transfer Model |
| SAA | Solar Azimuth Angle |
| SCIAMACHY | SCanning Imaging Absorption SpectroMeter for Atmospheric CHartographY |
| SCOPE | Soil Canopy Observation, Photochemistry and Energy fluxes |
| SFM | Spectral Fitting Method |
| SI | Scenario I |
| SIF | Sun-Induced chlorophyll Fluorescence |
| SII | Scenario II |
| SWC | Soil Water Content |
| SZA | Solar Zenith Angle |
| Ta | air Temperature |
| TOC | Top Of Canopy |
| TROPOMI | TROPOspheric Monitoring Instrument |
| UAV | Unmanned Aerial Vehicles |
| VAA | View Azimuth Angle |
| VI | Vegetation Indices |

| | |
|---|---|
| Vmax | Maximum Carboxylation Velocity |
| VPD | Vapour Pressure Deficit |
| VPM | Vegetation Photosynthesis Models |
| VZA | View Zenith Angle |

# Abstract

Recently, measurements of sun-induced chlorophyll fluorescence (SIF) has become a new approach to estimate vegetation photosynthetic activity and detect vegetation stress. However, the environmental factors controlling SIF largely remain unknown for different vegetation biome types. In addition, SIF measured at the top of canopy (TOC) is confounded by interactions between solar radiation and vertical canopy structures. Hence, development of three-dimensional (3-D) radiative transfer models, capable of simulating SIF, would be of immense benefit to test and verify various hypothesises.

The goal of this thesis is to develop a new 3-D SIF model and apply it to assess the relationship between SIF and plant photosynthetic activity across different spatial and temporal scales. Specifically, I (1) developed a new SIF module for FLiES (Forest Light Environmental Simulator) model (FLiES-SIF) and validated it with SIF observations at the seasonal scale; (2) partitioned SIF signals to overstory and understory layers by using FLiES-SIF, and then analysed the impact of solar radiation and canopy structure on understory SIF; (3) normalized the OCO-2 SIF dataset at nadir, hotspot and darkspot viewing directions by using the FLiES model, and assessed the relationship between SIF and GPP; and (4) identified that SIF observed at the top of canopy was strongly influenced by understory reflectance and canopy structure.

Results showed (1) the TOC SIF simulated by FLiES-SIF was closely correlated with SIF observations at a forest test site, and its performance was better than a 1-D model (Soil Canopy Observation, Photochemistry and Energy fluxes, SCOPE) and 3-D model (Discrete anisotropic radiative Transfer, DART); (2) the SIF emitted from understory contributed more than 51 % to the total SIF in the wet season of a tropical savanna site, however, it only accounted for less than 10% of total SIF in an evergreen forest site; (3) SIF was most correlated with GPP in the hotspot direction, and the normalised SIF yield could better explain the variations of light use efficiency (LUE); (4) compared to canopy structure and leaf properties, the understory reflectance was the primary factor influencing the observed SIF at the top of the canopy.

This thesis highlights the advantage of FLiES-SIF in capturing vegetation photosynthetic activities of ecosystems with complex canopy structures. This will significantly improve

our understanding of vegetation responses to climate change, and this model can be implement for numerous related purposes.

# Chapter 1. Introduction

## 1.1. Research background

### 1.1.1. Global carbon cycle under climate change

#### 1.1.1.1. Carbon cycle

The carbon cycle plays a significant role in our environment (Braswell et al. 1997; Cao & Woodward 1998). There are five primary carbon pools: atmosphere, ocean, biosphere, soil organic matter and lithosphere (Dixon et al. 1994). Carbon is cycled among those pools. Atmospheric carbon dioxide ($CO_2$) turns into carbohydrates by the process of photosynthesis in vegetation (Figure 1.1). $CO_2$ is produced by animals and microorganisms through the consumption and oxidation of carbohydrates, via respiration, which will return to the atmosphere.

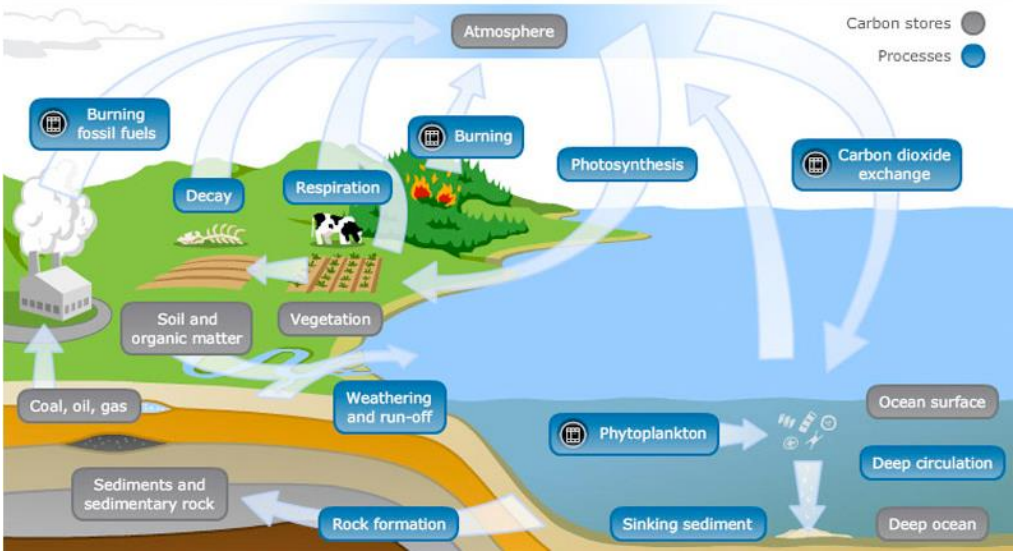


Figure 1.1. The global carbon cycle (https://www.sciencelearn.org.nz/resources/689-the-ocean-and-the-carbon-cycle, 2019)

Terrestrial ecosystems account for one-third of the earth's surface, and a large amount of carbon is absorbed from the atmosphere to vegetation by the process of photosynthesis (Falkowski et al. 2000). About half of the absorbed carbon is released to the atmosphere by vegetation's respiration function.

The carbon sink is the accumulation and storage of carbon-containing chemical compounds. Globally, forests constitute most of the main carbon sink which mainly happens in the terrestrial ecosystem, accounting for almost 80% of the aboveground

carbon sink and 40% of the belowground carbon sink (Dixon et al. 1994). The remaining carbon sink occurs in croplands, wetlands, grasslands and savannahs (Watson et al. 2000).

In recent years, global climate warming has become an emergency issue for human beings. The concentration of $CO_2$ dramatically increased to 414.83 parts per million (ppm) in 2019 from 285 ppm in 1850 (Dong et al. 2019). Consequently, land surface temperature has risen 0.8 °C above the global annual average. The high concentration of $CO_2$ and climate warming will bring extreme events and lead to the rising of sea levels and melting glaciers (Rosenzweig et al. 2001). Furthermore, it will impact people's health and living environment.

### 1.1.1.2. GPP in the global carbon budget

Gross primary productivity (GPP) is the amount of carbon biomass which is generated by primary producers. It is used to estimate the carbon sequestration capacity of the terrestrial ecosystems during photosynthesis (Beer et al. 2010; Magnani et al. 2007; Schimel et al. 2015). GPP impacts how much energy can be produced by vegetation, however, GPP cannot be measured directly, and thus eddy covariance data is used to partition GPP, as in the following formula:

$$GPP = NEE - R_{eco} \quad (1\text{-}1)$$

Net ecosystem exchange of carbon dioxide (NEE) is used for measuring carbon exchange between ecosystem and the atmosphere (Turner et al. 2006). When NEE value is negative, it means carbon dioxide uptake, while positive NEE value indicates $CO_2$ release to the atmosphere. The $R_{eco}$ term refers to the respiration of the ecosystem. With the development of eddy covariance studies, almost 500 flux sites have already been implemented worldwide to monitor the variation of $CO_2$, temperature, precipitation and windy days and nights (Baldocchi et al. 2001; Reichstein et al. 2007). The network of flux site covers all of the vegetation functional types.

Besides the field measurement approach, GPP data can also be obtained by MODIS (Moderate Resolution Imaging Spectroradiometer) satellite surface reflectance and Biome-BGC (biome biogeochemical cycles) models (Running et al. 2004). It offers an efficient way to estimate and evaluate GPP across the various temporal and spatial resolutions (Zhao, Running & Nemani 2006). However, some studies showed that MODIS GPP underestimated GPP when compared to the eddy covariance GPP in a highly productive area, and overestimated in a lower productive area (Turner et al. 2006; Turner

et al. 2003). Hence, vegetation photosynthesis models (VPM) were developed to estimate GPP by using vegetation indexes and temperature, showing excellent performance in forests and overcoming the shortage of the MODIS GPP (Zhang, Xiao, et al. 2017).

GPP can be presented by using the light use efficiency model, which simplifies the process of photosynthesis (Monteith 1972; Monteith 1977). It assumes photosynthesis is related to the light condition. Hence, GPP can be presented as follows,

$$GPP = LUE_p \times f_{PAR} \times PAR \quad (1\text{-}2)$$

$LUE_p$ means the light use efficiency for photosynthesis, $PAR$ represents the photosynthetic active radiation and $fPAR$ is the fraction of absorbed photosynthetic active radiation. This equation presents how much APAR (absorbed photosynthetic active radiation, $APAR = f_{PAR} \times PAR$) can be transferred to photosynthesis. $PAR$ can be measured from the satellite data, $f_{PAR}$ is retrieved from surface reflectance by an empirical model (Running et al. 2000; Wang et al. 2001). $LUE_p$ varies according to the vegetation functional types (Sims et al. 2008), growing season and environmental stresses, which makes $LUE_p$ estimation difficult (Nakaji et al. 2007). $LUE_p$ at the canopy scale is related to the latent heat flux, net radiation, carbon flux and water flux. Researchers also tried to use vegetation index, e.g. photochemical reflectance index ( $PRI = (\rho_{531} - \rho_{570})/(\rho_{531} + \rho_{570})$), to estimate $LUE_p$ (Drolet et al. 2008; Garbulsky et al. 2011; Penuelas, Filella & Gamon 1995). Although PRI can track the seasonal change of $LUE_p$, the coarse temporal resolution of satellite products produced PRI estimates divergent from previous studies, and besides, it needs further validation (Gamon et al. 2016; Nakaji et al. 2014; Stöckli et al. 2008). In addition, PRI's estimates, which explains LUE changes and is also varied within vegetation functional types, showed the best performance when analysed together with vapour deficit pressure (Nakaji et al. 2014).

In summary, eddy covariance measurements are the most accurate approach for estimating GPP. Due to the limited flux tower network in the world, it cannot estimate GPP globally using interpolation methods. Thus, light use efficiency models are more commonly applied and are currently the most reliable method to estimate vegetation productivity. However, there is still much uncertainty that needs to be addressed and results that need to be validated.

## 1.1.2. Photosynthesis and Chlorophyll fluorescence

### 1.1.2.1. Photosynthesis

Photosynthesis impacts the global carbon cycle and plays a critical role in supplying energy to life (Frank et al. 2015; Mercado et al. 2009). It takes place in the chloroplasts and converts $CO_2$ utilising light with water to sugar and oxygen (Figure 1.2). This process consumes greenhouse gas and releases the $O_2$ for supporting almost all life on Earth. Photosynthesis is prone to be influenced by climate change and extreme events, such as flooding, heat waves and drought (Fay et al. 2008; Heimann & Reichstein 2008), hence, it is a good indicator of vegetation responses to environmental stress. Gurney et al. (2008) suggested that global terrestrial photosynthesis can be used to identify the global terrestrial carbon sinks and sources and its estimation was consistent with long-term measurements of $CO_2$.

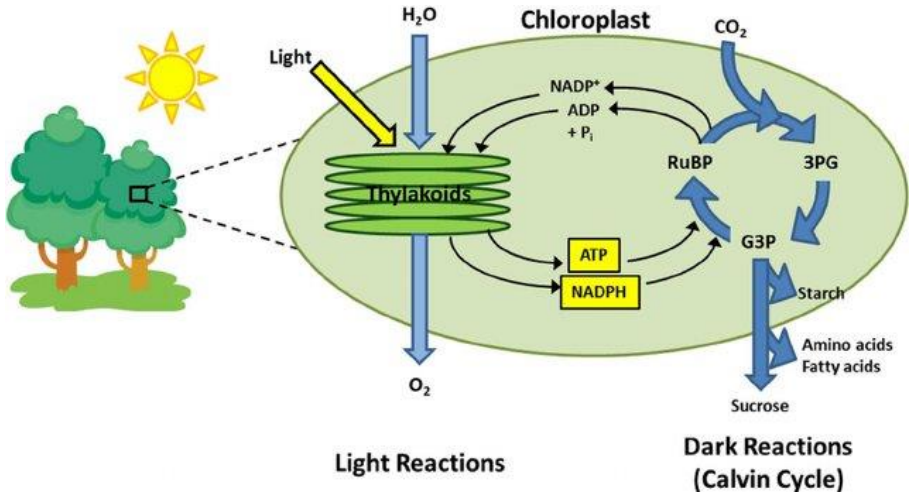


Figure 1.2. The process of photosynthesis (Rasmussen & Minteer 2014)

At the leaf level, there are three primary factors impacting photosynthetic activities: irradiance, carbon dioxide concentration and temperature (Bassow & Bazzaz 1998). At stable temperatures, the carbon assimilation relies on the variation of irradiance. The positive correlation between irradiance and carbon assimilation is reported, but carbon assimilation saturates at high levels of irradiance (LONG 1991). At low irradiance, the temperature affects the ability of the leaf to assimilate carbon. The positive patterns of carbon assimilation and temperature are reported at high irradiance levels (Beer et al. 2010).

However, photosynthesis at the canopy scale is affected by canopy structure (Ryu, Berry & Baldocchi 2019). The canopy density decides how much radiation can be absorbed by leaves and penetrate the canopy directly. The canopy interception can be presented as below,

$$i_0 = 1 - exp\left[-\frac{LAI\Omega(\theta)G(\theta)}{\cos(\theta)}\right] \quad (1\text{-}3)$$

where LAI is the leaf area index (the dimensionless quantity that characterises the density of plant canopies), $\Omega(\theta)$ is the clumping index at a giving angle, $G(\theta)$ is the leaf projection at a giving angle, and $\theta$ is the solar zenith angle. In order to calculate the canopy interception, LAI, leaf angle distribution and clumping index are essential (Myneni, Ross & Asrar 1989; Stenberg, Mõttus & Rautiainen 2016). LAI data can be provided by MODIS, but its sensors degradation brings difficulties for long-term analysis (Zhang, Song, et al. 2017). In addition, the non-conformity between MODIS LAI and GLOMAP LAI contributes to uncertainties for remote sensing studies using LAI (Jiang et al. 2017; Liu, Liu & Chen 2012). Fang et al. (2012) reported that the relative uncertainty of global LAI products is higher than twenty percent in forest environments. The various leaf angle distributions also increase the difficulties for modelling LAI (Knyazikhin et al. 1998).

In recent decades, LiDAR (Light Detection And Ranging) remote sensing has been used to successfully map LAI and canopy interception, because its high spatial resolution and cloud points provide accurate quantification of the leaf angle distribution and LAI (Bailey & Mahaffee 2017). However, the scan time cannot meet the requirements of the field studies. The clumping index varies with viewing angle and leaf density (Ryu et al. 2010). Different patterns of clumping index and viewing angle are reported in mature forests and sparse vegetation areas (Chen, Menges & Leblanc 2005).

### 1.1.2.2. Chlorophyll fluorescence

When sunbeams reach the surface of the leaves, part of the light photon is absorbed by their pigment system, and leaf emits the fluorescence (Meroni et al. 2009; Moya et al. 2004). The reemitted light is called sun-induced chlorophyll fluorescence (SIF). SIF is very weak and accounts for only about 1% of the total reflected sunlight. The SIF spectrum ranges from 650 nm to 800 nm. It has two peaks, one is at the 685 nm (red SIF),

which presents the information of photosystem II (PSII) (Iermak et al. 2016). The other peak is at 740 nm, which carries the information of both photosystems I (PSI) and II.

Chlorophyll fluorescence transferring from leaf cells to canopy level is a complex process (Porcar-Castell et al. 2014). First, excitation energy transfers between leaf pigments inter antenna (IA), outer antenna (OA), core and reaction centre (Engel et al. 2007). During the photochemistry process, part of the energy is excited as chlorophyll fluorescence and lost as heat. Second, at the photosystem scale, the photochemical and non-photochemical processes decide the quantum yield of fluorescence (Figure 1.3).

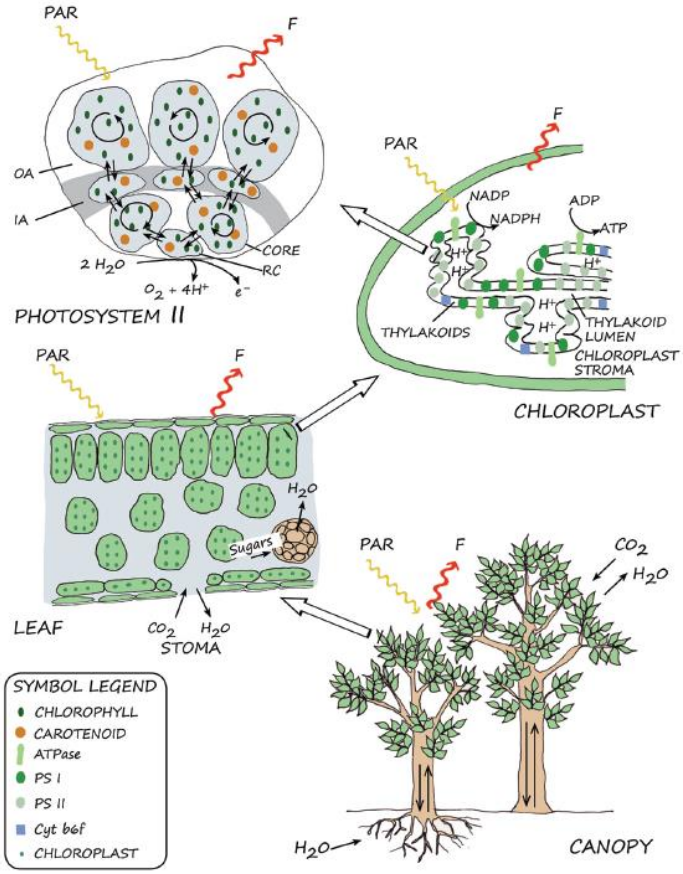


Figure 1.3. The generation of fluorescence from leaf to canopy scale (Porcar-Castell et al. 2014).

The fluorescence spectrum relies on the chlorophyll-protein and antenna structures. When we review at the chloroplast scale, both photosystem I and photosystem II affects the fluorescence signal, but their impacts on the spectral property and fluorescence quantum yield are non-uniform (Shinkarev & Govindjee 1993). Third, the leaf has its own mechanism which controls cell and chloroplasts to maximize the absorbed light usage for

photosynthesis. Lastly, at the canopy scale, the light intensity vertically influences the reemitted fluorescence.

From the energy aspect, light usage excitation and consumption keep unity (Frankenberg & Berry 2018). At the initial period of photosynthesis, chlorophyll molecules can process solar energy. The dedicated proteins can convert a part of this energy ($\phi_P$) and use it for photochemistry (Schlau-Cohen & Berry 2015). A fraction of energy, $\phi_F$, is reemitted as fluorescence. Part of the energy ($\phi_D$) is wasted and lost when photochemical centres are damaged by light saturation. The $\phi_P$ does not increase with light increases. Unused energy is not dissipated as $\phi_D$ because the leaf has its own mechanism to manage the excess through a regulatory process called nonphotochemical quenching (NPQ) (Fig.4.). This part of energy ($\phi_N$) is dissipated as heat. Because of the energy balance, energy usage and consumption can be written as,

$$\phi_P + \phi_F + \phi_N + \phi_D = 1 \tag{1-4}$$

The fluorescence quantum yield ($\phi_F$) can be calculated as,

$$\phi_F = \frac{K_F}{K_P + K_F + K_N + K_D} \tag{1-5}$$

where $K$ represents photosynthesis ($K_P$), fluorescence ($K_F$), NPQ ($K_N$) and heat dissipation ($K_D$). Normally, the fluorescence quantum yield accounts for a very small amount of the total energy (1%), so the sum of $\phi_P$, $\phi_N$, and $\phi_D$ is about one hundred fold of $\phi_F$. This explains why fluorescence is weak and is hard observe. Every quantum yield is not constant, and they vary with the environmental stresses (heat or drought) (Schlau-Cohen & Berry 2015). One can see from Figure 1.4 that light is mostly converted to photosynthesis (almost 80 %) in leaves that are deeply shaded. However, with the increase of light intensity, $\phi_P$ declines and $\phi_N$ increases. These estimates suggest that photosystems cannot fully use light under drought conditions. Also, $\phi_F$ can reflect the plant stress status even given the tiny fraction of total energy usage.

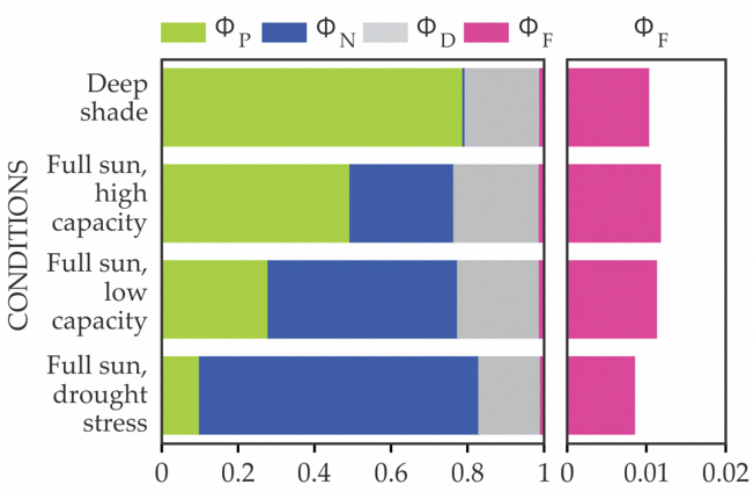


Figure 1.4. The fluorescence quantum yield (Schlau-Cohen & Berry 2015)

### 1.1.2.3. The link between photosynthesis activity and chlorophyll fluorescence

In the light use efficiency model, SIF can be represented as,

$$SIF = PAR \times f_{PAR} \times LUE_f \times f_{esc} \tag{1-6}$$

where $LUE_f$ is the light use efficiency for fluorescence and $f_{esc}$ is the escape ratio of fluorescence. When combined, equations 1-2 and 1-6, clearly show the relation between SIF and GPP:

$$GPP = SIF \times \frac{LUE_p}{LUE_f} \times f_{esc}^{-1} \tag{1-7}$$

Equation 1-7 illustrates how the relationship between SIF and GPP is related to the radiation, canopy structure and leaf biochemical parameters. Because chlorophyll content is mainly absorbed by APAR, SIF is better at predicting APAR, and presents a good correlation with GPP in crops and grasslands (Guanter et al. 2014b). SIF escape ratio ($f_{esc}$) is important for monitoring SIF in areas with a complex canopy structure. Because it shows the high probability of collision in the needle forest, Yang & van der Tol (2018) used the SCOPE (Soil canopy observation, photochemistry and energy fluxes) model to build a database of simulations and found that $f_{esc}$ is related to the reflectance, however, contribution of this method to correcting SIF is still uncertain.

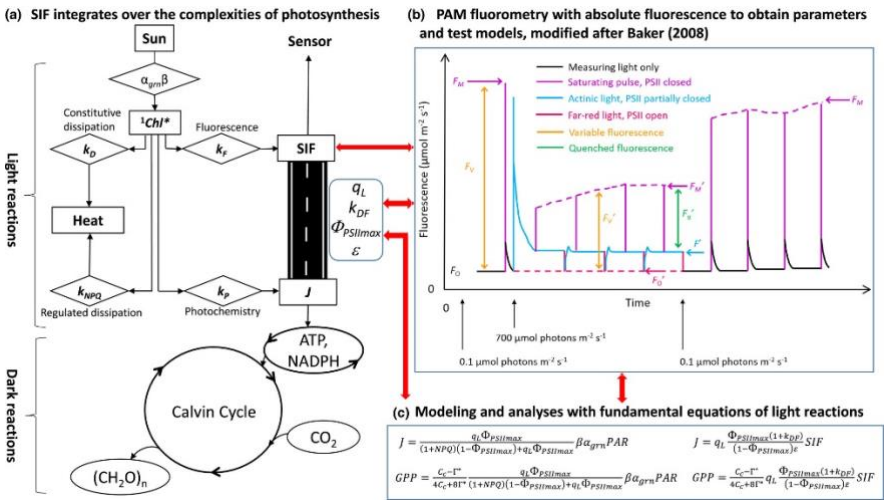


Figure 1.5. The relationship between SIF and photosynthesis (Gu et al. 2019a)

The relationship between SIF and GPP was found to vary with vegetation functional types and environmental factors (Frankenberg et al. 2011; Sun et al. 2017) (Figure 1.5). For example, the relationship of SIF and GPP is temporally diverse across the growth stage, the light conditions, fraction of cloud cover and temperature (Miao et al. 2018; Yang, Ryu, et al. 2018). Additionally, SIF was found to mainly carry the information of APAR, but cannot adequately explain the variation of $LUE_p$, hence, these findings do not support SIF as a proxy for photosynthesis (Wieneke et al. 2018c; Wohlfahrt et al. 2018b). The relationship between SIF and GPP is also present across cropland, grassland and forest (Damm et al. 2015b).

Sunny and cloudy days influence the relationship between SIF and GPP. Photosynthesis is prone to be saturated during high PAR for croplands, but this phenomenon does not appear in more complex canopy structures (Yang et al. 2015b). GPP on a cloudy day is slightly higher than on a sunny day in forests (Gu et al. 2003), indicating that high levels of diffuse radiation may increase fluorescence ability.

Although SIF presents a close relationship with photosynthetic activities, there are still some uncertainties in using SIF to estimate GPP (Ryu, Berry & Baldocchi 2019). For example, the field-measured and remotely sensed SIF contain errors, associated with the various retrieving methods for SIF retrieval and the calibration of the spectrometer. There is still a lack of tools to validate SIF and GPP across different scales. Even with established SIF field sensors, the limited field of view (FOV) cannot reveal the true relationship of SIF and GPP at the canopy scale. Airborne SIF data can minimise the gap between the coarse spatial resolution and directly validate with the satellite SIF

(Frankenberg et al. 2018; Rascher et al. 2015). The relation between $LUE_p$ and $LUE_f$ is not clear for various temporal scales and vegetation functional types. Sunlit and sunshade leaves' contribution total SIF are under discovery. Due to the light transmission at the canopy layers, within the depth of the canopy, the lower leaves emit less SIF compared to the illuminated leaves, but the vertical SIF distribution is still not completely known. Satellite SIF presents the instantaneous SIF, but how to scale the instantaneous SIF to the daily SIF considering the variations in light conditions remains a challenge (Zhang et al. 2016).

### 1.1.2.4. Remote sensing of SIF

The first global SIF map was provided by the Japanese Greenhouse Gases Observing Satellite (GOSAT) satellite in 2011 (Frankenberg et al. 2011; Guanter et al. 2012). The spectrometer of GOSAT is TANSO-FTS and covers the 755-775 nm region, with spectral resolution of 0.025 nm (Frankenberg et al. 2011). It can extract SIF signal by using Fraunhofer line at the 757 and 770 nm. However, its spatial resolution is 10.5 km, and observations are not continuous. In 2012, Joiner et al. (2012) retrieved global SIF signal at 866 nm from SCIAMACHY (SCanning Imaging Absorption SpectroMeter for Atmospheric CHartographY) satellite data based on CaII Fraunhofer line. Köhler, Guanter & Joiner (2015) retrieved global spatially continuous SIF data at 740 nm from SCIAMACHY data (Köhler, Guanter & Joiner 2015b). After the launch of the Global Ozone Monitoring Experiment–2 (GOME-2) by the European Space Agency, SIF studies have become much more convenient. GOME-2 provides four channels, and the fourth channel can cover 590 – 790 nm and its spatial resolution is 40 km * 80 km. However, from July 2013, the GOME-2 sensor MetOp-A's spatial resolution increased to 40 km * 40 km. Also, Joiner et al. (2016) used SCIAMACHY and GOME-2 SIF data to retrieve the red SIF for mainlands and oceans.

Due to the coarse spatial resolution of previous mentioned SIF satellite products, studies of the SIF distribution in finer spatial resolutions are still lacking. OCO-2 (Orbiting Carbon Observatory-2) was launched in July 2014 and provided high spectral resolution in 757 – 775 nm. Its FWHM (full width at half maximum) is 0.042, while the spatial resolution is 1.3 km * 2.25 km. The disadvantage of OCO-2 is that its observations are spatially discontinuous, which brings difficulties for long-term analysis (Frankenberg et al. 2014). TROPOMI (TROPOspheric Monitoring Instrument) is the newest SIF satellite and provides SIF data from the end of 2017. The medium spatial resolution (7 km * 3.5

km) and almost daily observations will make TROPOMI become the most powerful SIF satellite in the future (Guanter et al. 2015; Köhler, Frankenberg, et al. 2018) (Figure 1.6, **Error! Reference source not found.**).

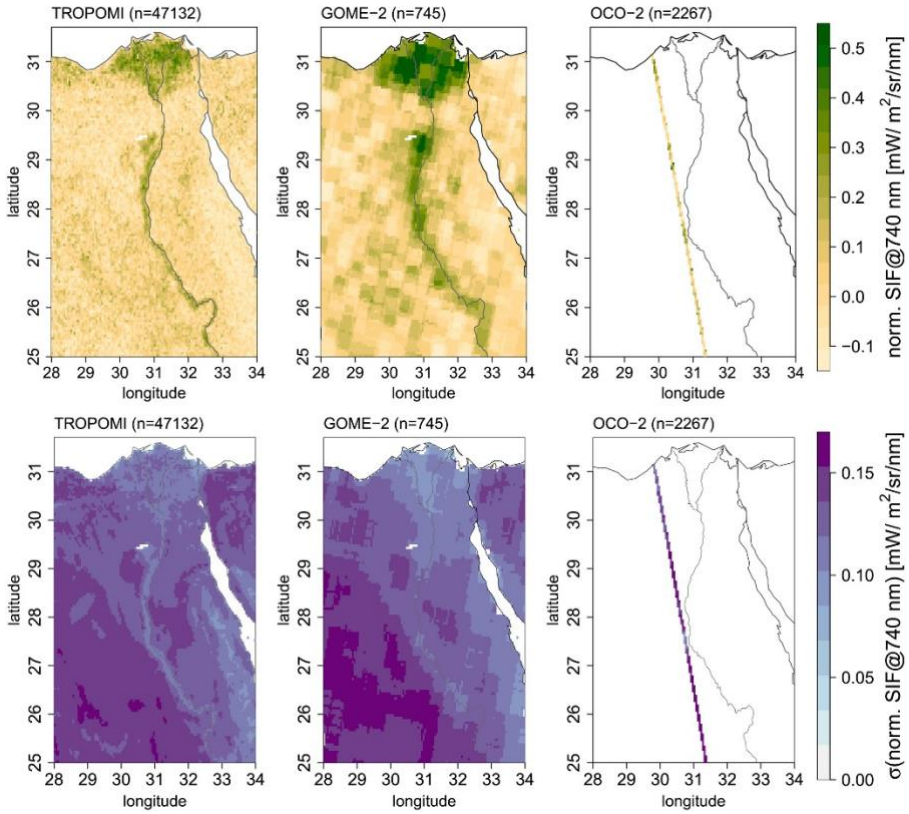


Figure 1.6. Comparison between TROPOMI, GOME-2, and OCO-2 SIF in the Nile region (Köhler, Frankenberg, et al. 2018)

Satellite SIF datasets are widely used to identify vegetation responses to environmental stress. Lee et al. (2013) used GOSAT SIF to identify SIF variations with the water supply in the Amazon. He and his collaborators found the both SIF and water supply decreased in the dry season, and that SIF presented a positive pattern with GPP. Sun et al. (2015) used GOME-2 SIF to monitor the significant drought in North America and found that SIF can be used to reflect the vegetation responses to extreme droughts. Yoshida et al. (2015) studied SIF variations in the Russian drought of 2010, and their results showed that SIF did not decline in croplands and forests, which was inconsistent with previous studies.

Remote sensing of SIF has also been used in phenology studies. Phenology is used to identify the seasonality of vegetation activity (Jeong et al. 2017). It is a significant indicator of vegetation responses to climate change (DRAGONI et al. 2011; Richardson

et al. 2010). Phenology is dependent on the greenness of the leaf, leaf chlorophyll content and environmental factors. Some studies have been pointing to an earlier onset of the growing stage than before, due to climate warming. For example, Piao et al. (2008) showed that the variation of phenology will prolong the growing stage and increase the rate of photosynthesis and respiration. The accurate extraction of the vegetation phenology is helpful for understanding and predicting the global carbon cycle (Bauerle et al. 2012).

Table 1.1. Summary of SIF satellite data available

| | SCIAMACHY | GOME-2 | GOSAT | OCO-2 | TROPOMI |
|---|---|---|---|---|---|
| Data availability | Aug 2002 – Mar 2012 | Aug 2007 - present | Oct 2009 - present | Sep 2014 - present | Nov 2017 - present |
| Overpass time | 10.00 LST | 9.30 LST | 13.30 LST | 13.30 LST | 13.30 LST |
| Nadir pixel size | 30 km * 60 km | 40 km * 40 km | 10.5 km | 1.3 km * 2.25 km | 7 km * 3.5 km |
| Swath width | 960 km | 1920 km | 705 km | 10.3 km | 2600 km |
| Revisit time | 6 days | 1.5 days | 3 days | 16 days | Almost daily |
| Spectral coverage | 604 – 805 nm | 590 – 790 nm | 755 – 773 nm | 757 – 775 nm | 640 – 784 nm |
| Spectral resolution | 0.48 nm | 0.5 nm | 0.025 nm | 0.042 nm | 0.38 nm |
| Signal-to-noise ratio | < 3000 | < 2000 | > 300 | < 1000 | < 5000 |

Traditionally, vegetation indices (VI) have been used in phenology for the few last decades, but they can only express a static greenness observation of the vegetation and cannot reflect the photosynthesis activity (Jeong et al. 2017; WHITE et al. 2009). Due to the high correlation between SIF and GPP, SIF has great potential for phenology studies. SIF contains the information of radiation and fluorescence quantum yield which can be used for detecting canopy stress. Joiner et al. (2014) used GOME-2 SIF to extract the phenology matrix for deciduous broadleaf forests, mixed forests and croplands. They found the growing stage was shorter than that obtained using the MODIS $f_{PAR}$ product.

Moreover, the SIF extracted phenology is much closer to the measurements from eddy covariance towers. Compared to VI, far-red SIF does not experience the saturation issue in high productivity areas (Guanter et al. 2014a; Yang et al. 2015b), hence, SIF can be an

efficient indicator to estimate APAR (Koffi et al. 2015). It implies that SIF can reflect the difference in photosynthesis rates when greenness is stable, for example; the vegetation responses to drought are related to the fluorescence yield for croplands, grasslands, and forests (Sun et al. 2015a; Yoshida et al. 2015). Compared to the variation in chlorophyll content, SIF presents higher correlation with water supply in the Amazon forest (Lee et al. 2013). Walther et al. (2016) used GOME-2 SIF to extract the phenology matrix for the northern evergreen forests, and results showed that the start of the season was one month earlier than in the Enhanced Vegetation Index (EVI) data (Walther et al. 2016). Jeong et al. (2017) used GOME-2 SIF and GOSAT SIF to extract the phenology for the northern forests, and found that the growing season was shorter than that obtained from the Normalized Difference Vegetation Index (NDVI). By analysing the relationship between SIF, NDVI, GPP and temperature, they showed SIF could better reflect the GPP variations.

#### 1.1.2.5. Field measurements of SIF

Many spectrometers with control system are used to measure and retrieve fluorescence in the field. Normally, SIF systems are installed to monitor SIF and evaluate the relationship between fluorescence and GPP. These systems include: FluoSpec, FluoSpec2 and SIF-Sys (Miao et al. 2018; Yang, Ryu, et al. 2018; Yang et al. 2015b). Nowadays, the spectrometers have developed higher spectral resolution. The most widely spectrometer is provided by the Ocean Optics Company (HR2000+, HR4000, QE Pro and USB4000) (Cogliati et al. 2015; Daumard et al. 2012; Garzonio et al. 2017; Yang et al. 2015a). Normally, devices are installed 10 meters above the canopy. The sensor, FloX, is designed to measure fluorescence under natural light condition and is coupled with the QE Pro spectrometer (Cogliati et al. 2015). A similar system is FluoSpex 2, which contains two spectrometers: QE Pro and HR2000+. Another system named FluoNet has been set up for monitoring grasslands, forests and croplands (Yang, Shi, et al. 2018). SIF detectors have also been mounted on UAVs (unmanned aerial vehicle) (Calderón et al. 2013; Zarco-Tejada, González-Dugo & Berni 2012), Piccolo Doppia is the most famous UAV-SIF system (MacArthur et al. 2014). It consists of a QE Pro spectrometer and two fibres which are used to measure the upward and downward radiance. UAV-SIF systems are helpful to understand the effects of multi angles on SIF retrievals.

Extractions of SIF signal include two methods: one is based on the radiance, and another one is based on the reflectance. The method based on the reflectance is retrieved as an

index (a ratio) for SIF, not a physical quantity. This method consists of three components: reflectance ratios, derivatives and infilling index. The ratio method is used widely because it is between two reflectances, using wavelengths (680 or 740 nm) which are affected by fluorescence and to remove the information from related reflectance. The most widely used ratios are $R_{690}/R_{600}$ and $R_{740}/R_{800}$ (Dobrowski et al. 2005).

The radiance method is based on Plascyk's Fraunhofer Line discrimination (FLD). The standard FLD needs the inside and outside wavelength in the Fraunhofer line and assumes these two regions are close to each other. SIF and radiance are almost the same in these two regions. Hence, SIF can be presented as,

$$SIF = \frac{I_{out}L_{in} - I_{in}L_{out}}{I_{out} - I_{in}} \quad (1\text{-}8)$$

In equation 1-8, $I_{in}$ and $I_{out}$ means solar irradiance inside and outside of Fraunhofer line, respectively.

Although the FLD method is a straightforward approach, the SIF and reflectance from inside and outside of the Fraunhofer line are not constant, hence, many retrieving methods based on FLD have been developed. For example, 3FLD and cFLD are based on multispectral data, while iFLD, eFLD, pFLD and SFM (Spectral Fitting Method) are based on hyperspectral data (Alonso et al. 2008; Meroni et al. 2010; Meroni & Colombo 2006). 3FLD is more accurate when compared to the FLD method, and much more stable compared to iFLD. Meroni et al. (2010) used simulated data to compare SIF estimates from the SFM with FLD methods. They found the performance of SFM is better than the traditional FLD method, hence, FLEX project choose SFM as the standard method for SIF retrieval (Rascher, Gioli & Miglietta 2008).

Currently, SIF signals can be extracted from ground-based measurements, airborne and space observations (Aasen et al. 2019). The ground-based measurements uses the $O_2$-A and $O_2$-B bands because the atmospheric scattering can be ignored between the sensor and the target, and the sensor is not disturbed by re-absorption issues. When retrieving SIF signals from space, the Fraunhofer line has usually been adopted, but as the width of the Fraunhofer line is narrow, hyperspectral data is needed for retrieving SIF.

### 1.1.2.6. Modelling of SIF

Models are an efficient tool to study SIF and can help researchers to understand SIF photon transference and distributions. At the leaf scale, there are several famous theories:

Beer's law theory, Kubelka-Munk theory, Stochastic theory and Monte Carlo simulations (Emmel 2000; Emmel & Hersch 1998; Ganapol et al. 1998; Pedrós et al. 2010).

With the development of SIF knowledge, the focus of modelling SIF has been transferred from the leaf to the canopy scale. The first SIF model at the canopy scale was the Olioso model, developed in 1992 (Olioso, Méthy & Lacaze 1992). The Olioso model assumed that light flux followed the Lambert-beer law. This model can only calculate the direct solar radiance and generate the radiance in the viewing direction. It can also simulate the background reflection of the incident photon and downward emitted radiation. The fluorescence consists of these three conditions.

The FLSAIL model combined the previous SAILH model and the canopy geometry (Rosema et al. 1991; Verhoef 1998). This model was developed based on the SAIL model, and added a module which can simulate the hot spot effect in a single scattering contribution. FLSAIL assumed that the canopy layer is homogeneous and adapts a leaf scale fluoresce model based on the Kubelka-Munk theory. The input parameters for FLSAIL includes viewing zenith angle, viewing azimuth angle, hot spot parameter, LAI, relative leaf thickness, fluorescence quantum efficiency, chlorophyll content and soil reflectance.

In 2002, the ESA (European space agency) started a FluoMOD research plan. This project planned to develop leaf scale and canopy scale fluorescence models based on the radiative transfer theory. At the leaf scale, Pedrós et al. (2010) developed the FluoMODleaf model based on the PROSPECT model and coupled leaf parameters including leaf structure with, chlorophyll content, carotenoid content, dry matter and water thickness. This model also considered the electron transfer rate and the ratio between solar energy absorption and contribution for photosystems I and II. Fluorescence, reflectance and transmittance between 400 and 700 nm could be simulated by the FluoMODleaf model. The canopy fluorescence model can consider how much radiation can be intercepted by the leaf and radiation distribution at vertical layers. Verhoef (1998) developed the FluoSAIL model based on the SAIL model. This model coupled with the MODTRAN model to simulate the photon transference in the atmosphere. FluoSAIL adapted the output of FluoMODleaf and can simulate the fluorescence spectrum between 400 and 1000 nm at 1 nm spectral resolution. Zarco-Tejada et al. (2006) developed the user interface software (FluoMOD) by combining FluoMODleaf and FluoSAIL. Currently, the FluoMOD fluorescence model

can only simulate the fluorescence of vegetation in a non-stressed state and has levels of uncertainty when simulating the $C_4$ vegetation under stress conditions.

SCOPE, as the newest and most widely used radiative transfer model and energy balance model, can simulate the reflectance and transmittance at the top of the canopy, fluorescence at any given viewing angles and vegetation photosynthesis conditions (Van der Tol et al. 2009). This model improves the current understanding of canopy photosynthesis and supports the simulation of vegetation's fluorescence under stress conditions.

SCOPE, FluoSAIL and PROSPECT models are one-dimensional and assume vegetation is homogeneous in vertical and horizontal dimensions. However, vegetation presents obvious heterogeneity of structure and biochemical properties (Ryu, Berry & Baldocchi 2019). Usually, a forest system consists of several distinguishable layers, including canopy, bush and grass layers. Hence, one-dimensional models cannot meet the requirements for proper vegetation properties simulation. This has led to the development of three-dimensional fluorescence models.

The DART (Discrete anisotropic radiative transfer) model integrated with the fluorescence module developed by CESBIO (Gastellu-Etchegorry et al. 2017) can simulate radiative transfer in a three-dimensional scene. In this model, all objects of vegetation and buildings are represented as a matrix of parallelepiped cells, each with its own optical properties (reflectance and transmittance). Moreover, the DART model allows for fluorescence emission to be simulated in different directions. FluorFLIGHT and FluorWPS are new 3D models that can simulate fluorescence at the top of the canopy (Hernández-Clemente et al. 2017; Zhao et al. 2016). DART, FluorWPS and FluorFLIGHT are all based on the Monte Carlo method and have their own ray-tracing frames. They use the FLUSPECT model to generate the Excited Fluorescence Matrices (EF-matrix) for PSI and PSII and simulate the fluorescence emission. FluorWPS has been used to simulate SIF signal for row crops, and FluorFLIGHT was used to study the physiological conditions of forests and found that SIF signal was influenced by canopy structure (Hernández-Clemente et al. 2017; Zhao et al. 2016), however, these models have not been validated with long-term, seasonal SIF measurements. Also, this model is not open source, and users cannot modify the model parameters according to their requirements. This increases the difficulties for implementation and understanding of the model.

The FLiES (Forest light environmental simulator) model is a powerful and open sourced three- dimensional radiative transfer model (Kobayashi & Iwabuchi 2008). It is based on the Monte Carlo method and a ray-tracing frame. The model generates a large number of photons at the beginning of the simulation and uniformly distributes them above the simulation area. The model generates the direction of each photon and uses a random method to generate the scattering direction when photons collide with objects in the simulation area. By repeatedly simulating large numbers of photons, the model produces more realistic results. In this study, I will develop a SIF module for the FLiES model and validate it with field-measured SIF. Additionally, I will apply the FLiES model to resolve issues that field measurements cannot address.

## 1.2. Objectives and research questions

The overall goal of this thesis was to build a three-dimensional fluorescence radiative transfer model and use it to interpret the photosynthetic activities of vegetation. The thesis objectives were addressed using remotely sensed data, the machine learning method and statistical tools. More specifically, I retrieved the key parameters for modelling from Sentinel-2 and Landsat surface reflectance data by using Gaussian progress regression methods. Field-measured SIF data coupled with remotely-sensed SIF data, including observations from GOME-2 and OCO-2 satellites, were used to validate the simulations and objectives. Furthermore, I retrieved vegetation structural parameters from LiDAR data. The objectives and research questions of this thesis are described below, by chapter;

**Chapter 1:** This is the introduction of this thesis. Firstly, I described the significance of the global carbon cycle to human beings and the environment, and the relationship between GPP and carbon cycle. Then I provided fundamental concepts about SIF and its relationship with photosynthesis. I also presented a comprehensive literature review on the remote sensing of SIF, field measurements of SIF and existing SIF models. Additionally, I pointed out the drawbacks of the current SIF models. Lastly, I listed the objectives and research questions of each chapter of this thesis.

**Chapter 2:** One-dimensional models assume homogeneous vegetation structure in the horizontal dimension, hence, they cannot fully depict the vertical distribution of radiation and fluorescence radiance. In order to fill this gap, I integrated the excited fluorescence matrices (EF-matrices) and a three-dimensional radiative transfer model (FLiES) based on the Monte Carlo method and the photon tracing frame. Vegetation structure and

biochemical parameters, including chlorophyll and water content, were retrieved from LiDAR data and Landsat surface reflectance by the Gaussian Processes Regression (GPR) method, respectively. I aimed to (1) retrieve vegetation structural parameters from LiDAR data; (2) retrieve the vegetation biochemical parameters from satellite surface reflectance using a machine learning method, and identify their seasonal changes; (3) develop a SIF module for the FLiES model; (4) validate a new SIF model with field-measured SIF in a field site in the United States (Harvard Forest) and compare it to a one-dimensional and a three-dimensional model; (5) use the newly develop SIF model to separate the SIF signal as emitted SIF and scattered SIF, and analyse the relationship between these two signals and GPP. This work is useful for understanding the relationship between SIF and photosynthetic activities, and offers a robust approach for long-term SIF simulations.

**Chapter 3:** Although devices deployed on the top of the canopy and SIF satellite data (GOME-2 and OCO-2) provide continuous SIF observations, they cannot reveal the dynamic change of understory SIF and how it contributes to the local ecosystem carbon dynamics. Radiative transfer models have been developed to study SIF emissions, however, the one-dimensional models assume the vegetation is homogeneous, and they lack the vertical spatial distribution of SIF. A three-dimensional model (FLiES) with the a SIF module can study SIF emissions from the overstory and understory layers, and improve our understanding of the vertical SIF dynamics within the vegetation. In this chapter, I aimed to (1) identify the patterns of SIF emission in overstory and understory layers among open shrublands, tropical savannas and evergreen broadleaf forests; (2) estimate the GPP of different vegetation types, partition the contribution from overstory and understory, and determine how it varies seasonally; (3) examine the factors affecting the overstory and understory SIF emissions. This research will be useful for understanding how SIF varies across the different vegetation layers and canopy cover gradients across several biomes.

**Chapter 4:** Under different light conditions (limiting to saturating), SIF and LUE exhibit positive or negative patterns for sunlit and sun-shaded leaves and also, variations of sun position and viewing angle bring additional uncertainties for the relationship of GPP and SIF, SIF yield and APAR, and SIF yield and LUE. In this chapter, I aimed to investigate the bidirectional reflectance distribution function (BRDF) effects on the SIF:GPP and SIF yield:LUE relationships, and discuss factors that impact SIF emissions from the sunlit

and sunshade crown area. The objectives were to (1) identify SIF variations with the view zenith angle and view azimuth angle for mixed forests, deciduous broadleaf forests and evergreen needleleaf forests at the site level; (2) examine the relationship between SIF and GPP for different viewing geometries, and normalise SIF at hotspot and dark spot directions to represent sunlit and sunshade crown area, respectively; (3) identify the relative importance of environmental factors (vapour pressure deficit, radiation, soil water content, etc.) contributing to nadir, hot spot and dark spot groups. This research will be useful for understanding sunlit and sunshade SIF variations and their sensitivity to environmental factors.

**Chapter 5:** SIF is sensitive to environmental stressors, such as heat and water deficit, however, SIF and GPP present a strong correlation in dense canopy areas, but a weak correlation in areas of sparse vegetation. However, the factors that affect SIF emission and scattering within different canopy structural conditions are still unknown. In this chapter, I aimed to examine how understory affects observed SIF coupled with leaf properties and canopy structures. I implemented a novel SIF module for a three-dimensional radiative model (FLiES) to generate a database covering 3150 conditions of varying of input parameters. Moreover, I tested the effects on the understory under two scenarios. Specific objectives were to (1) identify factors affecting the understory-observed SIF and generate a database for examining different scenarios impact on the understory; (2) study the canopy structure, leaf properties and understory reflectance influence on SIF retrievals under certain scenarios; (3) apply the relationship between SIF parameters and retrievals to analyse implicit factors affecting SIF observations in sparse and dense vegetation areas. This research will be useful for understanding how the understory layer contributes to SIF variations.

**Chapter 6:** This is the conclusion of this thesis. I summarised all findings, highlighted significant results and drew conclusions from each research chapter (Chapters 2 - 5). I also described the limitations of this thesis and the newly developed SIF model. Additionally, I suggested directions for future research in this field.

# Chapter 2. Enabling the three-dimensional FLiES model to simulate seasonal scale sun-induced chlorophyll fluorescence

## Abstract

Sun-induced chlorophyll fluorescence (SIF) is an effective tool for monitoring terrestrial vegetation photosynthesis activities and detecting canopy stress. The close relationship between SIF and gross primary production (GPP) allows its use for measuring seasonal photosynthetic efficiency in response to environmental stress, including extreme heat and drought, and for studying the relationship among SIF, canopy structure and functioning. Although SIF can be measured from satellites (OCO-2, GOME-2), complex and multi-layer vegetation canopy structures and optical interactions with non-vegetation landscape components hamper stress detection. Three-dimensional canopy models can potentially scale-up leaf-emitted SIF signals to the canopy level in heterogeneous environments, and thereby improve productivity retrievals from satellite SIF emissions.

In this study, we used photon tracing and the Monte Carlo computational algorithms to integrate the excited fluorescence matrices (EF-matrices) with a three-dimensional radiative transfer model (Forest Light Environmental Simulator, FLiES). Vegetation structure parameters were retrieved from LiDAR data and biochemical parameters, including chlorophyll content and water content, were retrieved from monthly Landsat surface reflectances by the Gaussian Processes Regression (GPR) method. We validated the model with seasonal field measures of SIF at Harvard Forest, USA. The coefficient of determination ($R_2$) was 0.8 (p-value < 0.001) and root mean square error (RMSE) was 0.11 mW/m2/sr/nm. The models' performance for simulating SIF was compared with the SCOPE model (one-dimensional) and the DART model (three-dimensional), and demonstrated the stable performance of the FLiES-SIF model. Lastly, we found the model effective in extracting emitted SIF in the far-red region, resulting in the emitted SIF significantly correlated with light use efficiency (LUE), $R_2$ = 0.70 and 0.76 for sunny days and cloudy days, respectively. The FLiES-SIF model was found to be an accurate, robust and simplified approach for SIF simulation to improve our understanding of the coupling between SIF and photosynthesis activity.

## 2.1. Introduction

As a visible indicator, sun-induced chlorophyll fluorescence (SIF) is a new approach to study vegetation photosynthesis remotely (Berry 2018). SIF has two peaks, a red SIF signal at 680 nm and a far-red signal at 740 nm. The far-red SIF contains information of photosystem I and II (PSI, PSII) and is used widely to study photosynthesis activity due

to lower re-absorption rates (Poscar 2014). In recent studies, SIF has been used as an effective proxy to study vegetation responses to heatwaves and other stress (Song et al. 2018b; Wieneke et al. 2018a; Wohlfahrt et al. 2018a; Wu, Xiao, et al. 2018). In addition, more and more continuing field measurements of SIF (Hu et al. 2018; Miao et al. 2018; Yang et al. 2017; Yang, Ryu, et al. 2018; Yang et al. 2015b) would improve the understanding of the relationship between SIF and photosynthesis across different temporal and spatial scales.

Because of SIF's strong correlation with photosynthesis activity, SIF can be used to estimate gross primary productivity (GPP). The combined use of SIF field measures with flux measurements has become more prevalent in SIF studies. Hence, some field devices (FluoSpec, FluoSpec2, SIF-Sys) have been set up to study the relationship of SIF and GPP, absorbed photosynthesis active radiation (APAR), and light use efficiency (LUE) among crops and evergreen broadleaf forest (Miao et al. 2018; Wieneke et al. 2018a; Yang, Ryu, et al. 2018; Yang et al. 2015b). Some studies have found the satellite observed SIF to be linearly related to eddy covariance GPP, and that SIF can better capture GPP seasonal changes (Frankenberg et al. 2011; Guanter et al. 2014b; Smith et al. 2018). SIF has been derived from many satellite platforms, such as GOSAT (Greenhouse Gases Observing Satellite) (Frankenberg et al. 2011; Guanter et al. 2014b), GOME-2 (Global Ozone Monitoring Instrument 2) (Joiner et al. 2013; Köhler, Guanter & Joiner 2015a) and OCO-2 (Orbiting Carbon Observatory 2) (Sun et al. 2017). But the coarse spatial resolution of GOME-2 (40 km * 40 km) and disperse temporal observations of OCO-2 are major disadvantages. The newly launched TROPOMI (TROPOspheric Monitoring Instrument) (Köhler, Frankenberg, et al. 2018) might overcome these issues with 7 km * 3.5 km pixels and daily revisit.

The SIF signal can be simply divided into leaf emitted SIF and scattered SIF (equation 2-1, $SIF_{scatter}$ is the scattered SIF, $SIF_{emitted}$ is the emitted SIF, which is observed by sensor without any collisions). The scattered SIF signal is affected by canopy structure (Damm et al. 2015a; Verrelst et al. 2016), where the scattered fluorescence signal loses energy during the scattering effect. The emitted SIF (we can treat it as "pure SIF") presents a closer relation with photonsynthesis activity. Due to the low re-absorption of leaf in the near-infrared region, far-red SIF would be more suitable to study the link between emitted and scattered SIF with photosynthesis. Sensors cannot separate the emitted SIF from scattered SIF, however models can fill this gap.

$$SIF = SIF_{scatter} + SIF_{emitted} \quad (2\text{-}1)$$

FluorMODleaf (Pedrós et al. 2010) and FluorSAIL (Miller et al. 2005) 1-dimensional models were developed to study the fluorescence at leaf and canopy levels, respectively. FluorSAIL is based on the SAIL model and simulates fluorescence by using inputs from FluorMODleaf. Relying on the FluorSAIL model, SCOPE (Soil Canopy Observation Photochemistry and Energy fluxes, 1-dimensional model) was developed to study the leaf fluorescence emission at the top of canopy (TOC) for homogeneous canopies (Van der Tol et al. 2009). However, these models are unable to be applied over complex vegetation canopies, especially for simulating vegetation with horizontal and vertical heterogeneity (Porcar-Castell et al. 2014).

Advanced three-dimensional radiative transfer models for SIF simulation have been developed, including FluorWPS (Fluorescence model with Weighted Photon Spread method) (Zhao et al. 2016), DART (Discrete Anisotropic Radiative Transfer model) (Gastellu-Etchegorry et al. 2017) and FluorFLIGHT (Hernández-Clemente et al. 2017), all of which rely on the Monte Carlo method and based on the leaf model FLUSPECT (Van der Tol et al. 2009; Verhoef 2011; Vilfan et al. 2016) to generate Excited Fluorescence Matrices (EF-matrix) for PSI and PSII, separately. FluorWPS has been used to simulate the SIF signal for row crops, and FluorFLIGHT was used to study the physiological conditions of forest from which the SIF signal was found to be influenced by canopy structure (Zhao et al. 2016).

However, these models have not been validated for SIF seasonal changes over long term periods, constrained by difficulties in providing seasonally-varying input parameters. The input biochemical parameters (leaf structure, chlorophyll content, leaf dry matter, leaf water, etc.) are critical to SIF variations, as leaf structure, chlorophyll and carotenoid content (N, Cab and Cca) influence EF-matrices and reflectance and transmittance properties in the PAR and near infrared spectral regions (Verrelst et al. 2016). Measuring these input parameters is difficult over seasonal periods, hampering long term SIF simulations.

Machine learning applications offer the potential of seasonal parameter retrievals, with some studies successfully applying Gaussian Processes Regression (GPR) methods to retrieve total chlorophyll content, leaf area index (LAI) and fraction of vegetation cover (FVC) from Sentinel-2 satellite spectral bands with high precision results (Camps-Valls

et al. 2016; Verrelst et al. 2012). Machine learning methods offer new possibilities to apply 3D radiative transfer models to simulate SIF seasonality through improved retrievals of biochemical parameters and geometric shapes of vegetation structure across different spatial and temporal resolutions. The machine learning method also avoids the complex RTM (Radiation Transfer Model) model inversion and time-consuming construction of look-up tables (Kempeneers et al. 2008; Shiklomanov et al. 2016; Zhang et al. 2014).

FLiES model (Forest Light Environmental Simulator) is a three-dimonsional radiative transfer model (Kobayashi & Iwabuchi 2008). Its robust ray-tracing frame makes possible expanding based on various purposes (Kobayashi et al. 2012). The goal of this study is to develop a SIF module for the three-dimensional FLiES model and use machine learning to retrieve biochemical parameters from satellite surface reflectances. The seasonal SIF simulations are validated with field measured SIF and the performance of the new SIF module is compared with other 3-D and 1-D models. The relationships between emitted and scattered SIF from the model with GPP are also analysed. This work is useful for understanding the relationships between SIF and photosynthesis activities, and offer an easy approach for simulating SIF in the long term.

## 2.2. Study area and Data

### 2.2.1. Study area

Canopy SIF was measured in Harvard Forest, Petersham, Massachusetts, USA (42°32'06″N, 72°10'28″W). The plant function type is deciduous broadleaf forest and dominant tree species are red oak and red maple. The annual mean temperature of Harvard Forest is around 7.5 °C, and the annual precipitation is about 1200 mm. Snow covers the ground for several months during winter. We set a 30 $m_2$ area for model simulations covered SIF measurements, and we assume tree species here are homogenous.

### 2.2.2. LiDAR data

We retrieved vegetation structure, shape and height, from the Light Detection and Ranging (LiDAR) data. LiDAR data is a remote sensing method that airborne laser is pointed at a targeted object on the ground, the beam of light is reflected by the surface it encounters. Hence, LiDAR consists of cloud points of vegetation on the ground. LiDAR data are provided by G-LiHT (https://gliht.gsfc.nasa.gov), they surveyed Prospect Hill in

June 2012. We assumed that vegetation in this area was mature and height and extreme crown changing could be ignored.

A Canopy Height Model (CHM) (McGaughey 2009) is implemented to separate vegetation layer and ground layer. The vegetation layer contains the height of each cloud point. Then we use crown detect method to locate crown of each vegetation and extract each crown's height, radius and positions. In summary, we get properties of each tree in study area.

### 2.2.3. Landsat reflectance

In order to analyse the seasonal change of biochemical parameters, Landsat-8 OLI surface reflectance data were gathered from 2013 to 2014. The Landsat 8 OLI launched on the 11 February 2013 and has a 16 day temporal resolution and 30 $m_2$ spatial resolution. The first seven bands (band 1 ~ band 7) of Landsat-8 OLI's were used to retrieve biochemical parameters. Quality control was applied to the data and removed low-quality observations. Data extract and process were applied on Google earth engine (https://earthengine.google.com/). A total of 22 Landsat images covering two growing seasons were processed to surface reflectance (ten scenes for 2013 and twelve scenes for 2014).

### 2.2.4. Eddy covariance GPP

Daily mean eddy covariance GPP ($GPP_{EC}$) data was calculated for checking the relationship between $GPP_{EC}$ and different model simulations. The R package, REddyProc (Wutzler et al. 2018), was implemented to estimate daily mean GPP with hourly eddy covariance and meteorological data. This tool used the gap-filling and flux partitioning algorithms to partition net flux (NEE) into GPP and field ecosystem respiration (Reichstein et al. 2005). The hourly eddy covariance and meteorological data were collected from EMS (Environmental Measurements Tower) tower (1.4 km from SIF measurements), and we averaged the daily GPP from 6:00 AM to 6:00 PM and remove outliers.

### 2.2.5. Measured Canopy SIF

Field measurements of SIF at Harvard Forest were used for validating model simulations in this study. The canopy SIF was measured from 2013 to 2014 (Jun 2013 – Oct 2013,

May 2014 – Oct 2014). The FluoSpec system was developed to estimate SIF at 760 nm ($SIF_{Field}$) with 5 minutes interval in the field 5 m above the top of the canopy. We averaged SIF between 6:00 AM and 6:00 PM and removed outliers. Clear sky conditions were defined as diffuse radiation / (diffuse radiation + direct radiation) < 0.5. Diffuse radiation and direct radiation were measured at EMS tower. More details, please check Yang's study (Yang et al. 2015b).

## 2.3. Methodology

This section briefly describes the framework of SIF simulation and a machine learning method used to retrieve biochemical parameters from remotely sensed data.

### 2.3.1. FLiES SIF module

FLiES (version 2.48) model is a three-dimensional radiation transfer model (Kobayashi & Iwabuchi 2008; Kobayashi, Suzuki & Kobayashi 2007). It is based on the Monte Carlo method and set a large number of photons uniformly distribute above the simulated area. The model generates the direction of each photon. Scattering occurs when photon collapsed with objects in the simulated scene, and model will calculate scattering direction and energy consumption during scattering. We assume that the leaf surface followed Lambertian concept. The random number generates scattering direction, including reflectance and transmittance. Normally, the ratio of reflectance and transmission's time is 1:1. By repeated simulate large numbers of photons, the result is close to the reality.

We developed the new SIF module for the FLiES model. Based on the original photon ray-tracing frame, we separated the photon as non-fluorescence and fluorescence photon. For the non-fluorescence photon, its simulation followed the original ray-tracing framework. However, for the fluorescence photon, the newly developed module would calculate each photon's scatter direction, and emitted fluorescence which activated by the incoming non-fluorescence and fluorescence photon. Before simulation, we applied pre-tracing progress for calculating the fluorescence correction factor and how much PAR reached leaf (Rosema et al. 1998; Zhao et al. 2016). Because the fluorescence correction factor changed by the incoming photosynthetic active radiation (PAR).

The backward and forward emitted fluorescence are calculated as follows,

$$Qf_{back}(\lambda_f) = \int_{400}^{750} \{[Q_{in}(\lambda_e) + Qf_{in}(\lambda_e)] \cdot M_{PSI}(\lambda_e, \lambda_f) + [Q_{in}(\lambda_e) + Qf_{in}(\lambda_e)] \cdot \phi_f \cdot M_{PSII}(\lambda_e, \lambda_f)\} d\lambda_e \quad (2\text{-}2)$$

$$Qf_{for}(\lambda_f) = \int_{400}^{750} \{[Q_{in}(\lambda_e) + Qf_{in}(\lambda_e)] \cdot M_{PSI}(\lambda_e, \lambda_f) + [Q_{in}(\lambda_e) + Qf_{in}(\lambda_e)] \cdot \phi_f \cdot M_{PSII}(\lambda_e, \lambda_f)\} d\lambda_e \quad (2\text{-}3)$$

In these two equations, $Q_{in}$ and $Qf_{in}$ are incoming non-fluorescence and fluorescence flux, separately. $M$ is the EF-Matrix, $\phi_f$ is the correction factor, which is dependent on the incident PAR, $Qf_{back}$ and $Qf_{for}$ is the backward and forward emitted fluorescence, separately. Because the fluorescence yield of PSI generally remains constant under illumination, so fluorescence correction factor only multiplied with PSII fluorescence yield. Hence, the emitted fluorescence can be calculated as,

$$Qf_{emit}(\lambda_f) = f_{esc} \times \begin{cases} Qf_{back}(\lambda_f) \times |n_d \cdot n_l|, & (n_d \cdot n_l)(n' \cdot n_l) < 0 \\ Qf_{for}(\lambda_f) \times |n_d \cdot n_l|, & (n_d \cdot n_l)(n' \cdot n_l) > 0 \end{cases} \quad (2\text{-}4)$$

The $f_{esc}$ is used to check whether the fluorescence can be detected by sensor. If fluorescence can reach the sensor, $f_{esc}$ = 1, and 0 otherwise. $n_d$, $n_l$ and $n'$is the vector for scattered direction, leaf surface and incident direction.

For scattered fluorescence flux, we simply use leaf reflectance and transmittance to be multiplied with $Qf_{in}$.

$$Qf_{scatter}(\lambda_f) = f_{esc} \times \begin{cases} Qf_{in}(\lambda_f) \times R \times |n_d \cdot n_l|, & (n_d \cdot n_l)(n' \cdot n_l) < 0 \\ Qf_{in}(\lambda_f) \times T \times |n_d \cdot n_l|, & (n_d \cdot n_l)(n' \cdot n_l) > 0 \end{cases} \quad (2\text{-}5)$$

In this equation, $R$ and $T$ is leaf reflectance and transmittance, respectively. Then we set a virtual sensor at the top of canopy. Our model surveyed how much fluorescence flux this sensor could detect.

$$F(\lambda_f) = \frac{\sum[Qf_{emit}(\lambda_f) + Qf_{scatter}(\lambda_f)]}{\pi A_{top} \cos\theta_0} \quad (2\text{-}6)$$

In this equation, $F(\lambda_f)$ is the scattered or emitted fluorescence flux can detected by the virtual sensor, $A_{top}$ is the simulation area, and $\theta_0$ is the sensor zenith angle. Then we simulated the fluorescence from 640 nm to 850 nm with spectral resolution of 1 nm.

### 2.3.2. Machine learning

In order to prepare the leaf reflectance, transmittance and EF-matrices for model input, we implemented PROSPECT (Feret et al. 2008) and FLUSPECT models coupled with the biochemical parameters (leaf structure (N), total chlorophyll content (Cab), carotenoid content (Cca), leaf water thickness (Cw), and leaf dry matter (Cd)). These five biochemical parameters are retrieved from the Landsat surface reflectance. We applied the Gaussian Process Regression (GPR) model to establish a relationship between the Landsat surface reflectance and biochemical parameters. Radial-Basis Function (RBF) was selected as the GPR's kernel as below,

$$k(x_i, x_j) = \exp\left(-\sum_{b=1}^{B} \frac{\|x_i - x_j\|^2}{2\sigma^2}\right) \quad (2\text{-}7)$$

where $\sigma$ is the length scale, which controls the spread of the relations for the spectral band, B is the number of bands, $x_i$ is the spectrum reflectance in each band.

Table 2.1. The $R_2$ and RMSE of the training group and validation group, which predicted by GPR model

| | Training group | | Validation group | |
|---|---|---|---|---|
| | $R_2$ | RMSE | $R_2$ | RMSE |
| N | 0.94 | 0.067 | 0.92 | 0.084 |
| Cab | 0.91 | 6.7 | 0.90 | 6.76 |
| Cca | 0.87 | 1.8 | 0.90 | 1.35 |
| Cw | 0.93 | 0.0012 | 0.97 | 0.0014 |
| Cd | 0.97 | 0.00067 | 0.94 | 0.0011 |

We selected Angers (Angers 2003) (Jacquemound et al. 2003) and LOPEX (LOPEX 1993) (Hosgood et al. 1995) leaf database for GPR generating the prediction model. These two databases contain a variety of plant species' leaf spectrum and bio-parameters (Zhang et al. 2014). We divided 80% of Angers leaf database as training group and 20% as a validation group and applied ten folds cross-validation to get the prediction model with the lowest Root Mean Square Error (RMSE). The **Error! Reference source not found.** shows the training results and validation results. All prediction results' significants are below 0.001.

Based on the established relationship between reflectance and biochemical parameters, I used the band 1-7 of Landsat reflectance data as the input bands for the prediction model, so the model can generate the biochemical parameters.

### 2.3.3. Model simulations

Table 2.2. Settings for FLiES, SCOPE and DART model

| Variable | FLiES | DART | SCOPE |
|---|---|---|---|
| Simulation area | 30 m2 | 30 m2 | - |
| Solar zenith angle, view zenith angle | 30°, 0° | 30°, 0° | 30°, 0° |
| PAR | Field measured | Field measured | Field measured |
| LAI | Field measured | Field measured | Field measured |
| Biochemical parameters | GPR model | GPR model | GPR model |
| EF-matrix | FLUSPECT model | FLUSPECT model | FLUSPECT model |
| Fluorescence quantum efficiency for PSI and PSII (fqeI, fqeII) | 0.002, 0.01 | 0.002, 0.01 | 0.002, 0.01 |
| Leaf angle distribution | Uniform distribution | Uniform distribution | Uniform distribution |
| Crowns shape | ellipsoid | ellipsoid | - |
| Metrological data | - | - | Field measured |
| Aerodynamic data | - | - | Field measured |

We applied three models to simulate SIF at 760 nm: FLiES model with new developed SIF module (FLiES$_{SIF}$), a three-dimensional model DART (DART$_{SIF}$) and a one-dimensional model SCOPE (SCOPE$_{SIF}$). Table 2.2 shows the simulation scheme for three models. Before simulation, we applied the GPR model to retrieve biochemical parameters from the Landsat surface reflectance. Then the interpolation method was used to generate daily biochemical parameters. FLUSPECT model coupled with biochemical parameters generated forward and backward EF-Matrices for PSI and PSII. PROSPECT model was

implemented to generate leaf spectrum (reflectance and transmittance). EF-matrix and leaf spectrum were used for models simulations (Figure 2.1). In the end, we validate model simulations with field measured SIF.

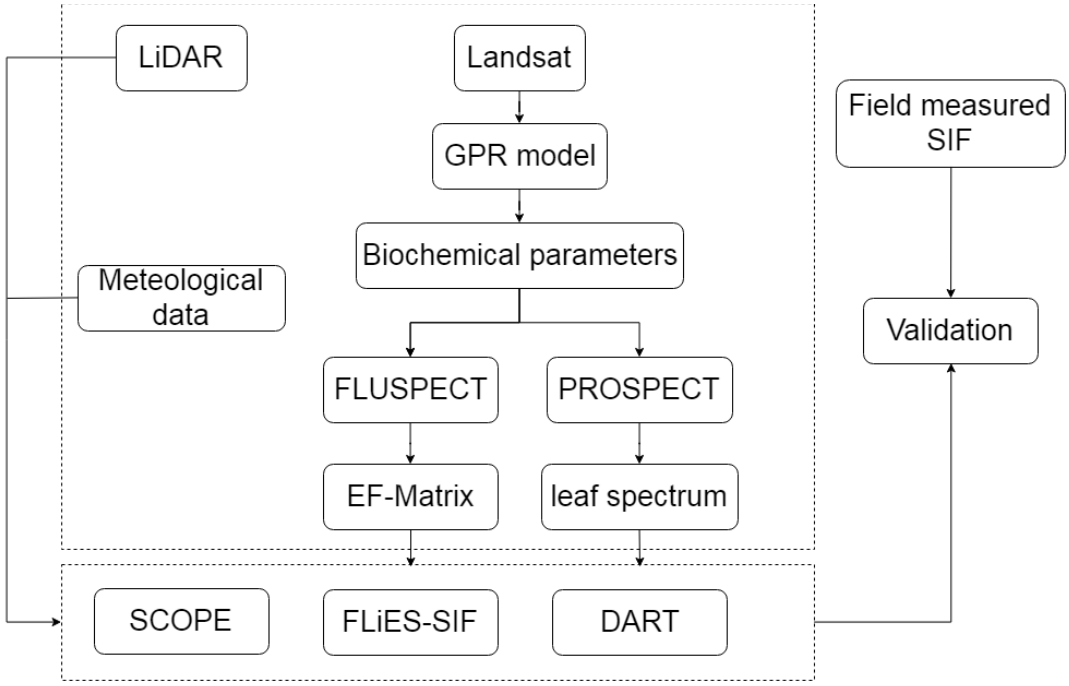


Figure 2.1. Flowchart of simulations

### 2.3.3.1. FLiES-SIF model

There are two main steps for FLiES model setting. First, the simulation landscape is defined as a space of 30 * 30 $m^2$. It consists of four layers, atmosphere layer, vegetation layer, floor layer and soil layer. In the vegetation layer, crowns and trunks are defined as geometric shapes. We use the cylinder to represent the vegetation's trunk and ellipsoid for the crowns. The height of trunk and radius of crowns are retrieved from LiDAR data.

Second, we used FLiES SIF module to simulate SIF at 760 nm, and compare model simulation results with SCOPE model, DART model and field measured canopy SIF (Figure 2.1). Regarding the previous study (Wu, Kobayashi, et al. 2018), we set $10^6$ photons for simulation, and it can let the simulation results close to reality.

### 2.3.3.2. DART model

The DART model is a comprehensive physically based, three-dimensional radiative transfer model (Gastellu-Etchegorry et al. 1996). We implement it to simulate SIF at 760 nm and validate FLiES model performance. The DART model can simulate radiance distribution and radiative budgets in different scenes, such as forest, crops, and urban.

DART model (version 5.7.1) offers a simulation of SIF in the 3D scene using the FLUSPECT model, which calculates the EF-matrix the same as used in the FLiES and SCOPE models.

Vegetation structure was retrieved from the LiDAR data as described in section 2.2. In the DART model we set the crown shape sphere the same as the vegetation model of FLiES, and the ratio of relative height and crown height equal to 1. Leaf angle distribution is set uniform distributions. The parameters of FLUSPECT model is predicted by using the GPR model. Iteration times are set to five, in order to get the valid results. Irradiance value is collected from the EMS tower as same as set in FLiES and SCOPE model. Remaining parameters are kept as the default value.

#### 2.3.3.3. SCOPE model

SCOPE is a simulation model for radiative transfer, photosynthesis and energy fluxes in vegetation and soil (version 1.7). It is a one-dimensional model and treats the simulation area as homogeneous. Inputs of SCOPE model included meteorological data (incoming shortwave radiation and longwave radiation, air temperature, vapour pressure, wind speed and CO2 concentration), leaf biochemical data and canopy-level data (LAI and vegetation height and leaf inclination). Meteorological data and LAI are available from Harvard forest dataset. Vegetation height is retrieved from the LiDAR data and leaf inclination was assumed a uniform distribution. Chlorophyll content (Cab) is retrieved from Landsat data (Section 3.2). The maximum carboxylation capacity (Vcmax) is set to 57.7 as the plant function type (deciduous broadleaf forest) of the study area (Zhang et al. 2016). Other input parameters, including leaf thermal reflectance and transmittance, are set to default values. Based on above settings, we used SCOPE to simulate SIF at 760 nm.

### 2.3.4. Statistical Analysis

Root mean square error (RMSE) is used to assess the performance of the new developed SIF module. The index is defined as follows,

$$\mathrm{RMSE} = \sqrt{\frac{\sum_{i=1}^{N}\left(x_{\mathrm{mea,i}} - x_{\mathrm{sim,i}}\right)^2}{N}} \tag{2-8}$$

Where $x_{\mathrm{mea,i}}$ and $x_{\mathrm{sim,i}}$ are the SIF for the measured and simulated, respectively, and N is the number of measured SIF days. Then, we use the coefficient of determination to check the relationship between simulated SIF and measured SIF at temporal scale. Data

processing, statistical analysis and visualisation are conducted in R scientific computation environment (R core team version 3.4) and associated packages obtained from the comprehensive R archive network (http://cran.r-project.orj).

## 2.4. Results

### 2.4.1. Retrieved biochemical parameters in two years

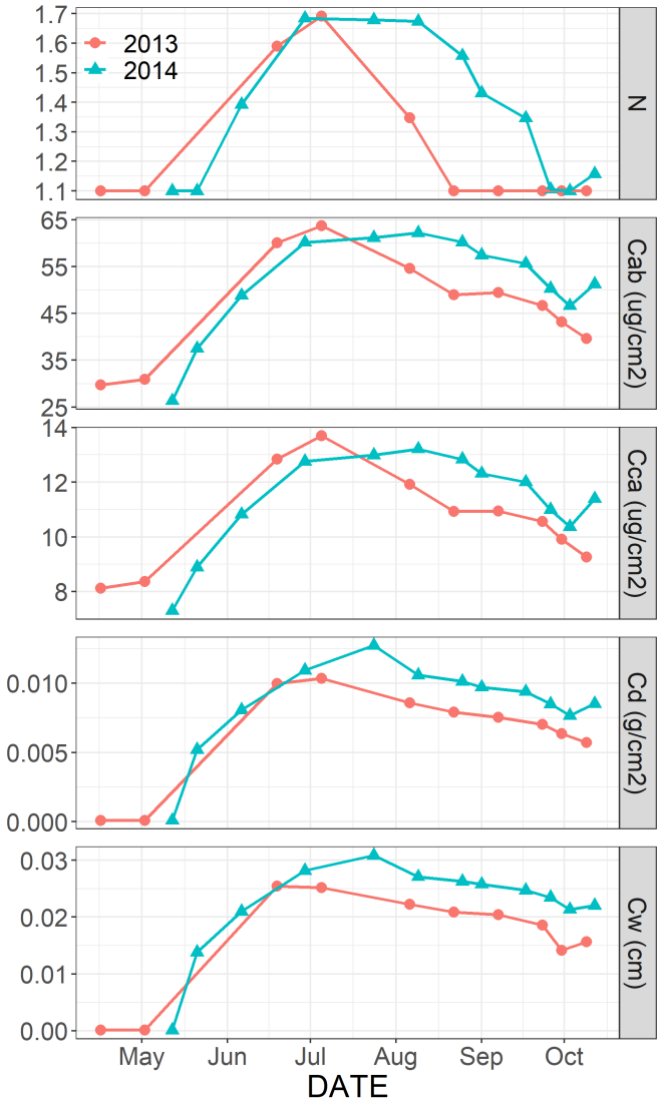


Figure 2.2. Seasonal and annual changes in retrieved biochemical parameters for years 2013 and 2014. N is the leaf structure, Cab is the total chlorophyll content, Cca is the carotenoid content, Cd is the dry matter of leaf and Cw is the leaf water content.

Figure 2.2 shows the five retrieved biochemical parameters for the 2013 and 2014 growing seasons by using the GPR method (see section 3.2). These biochemical parameters showed significant seasonal trends in both 2013 and 2014 (Figure 2.2). Their

values were highest around July and decreased in mid-August, which was similar with their vegetation phenology (Klosterman et al. 2014). However, a major difference between these two years was the shorter peak season period of these biochemical parameters in 2013 compared to 2014.

The yearly average and range (2013 and 2014) of N, Cab, and Cca was 1.3±0.24, 49.3±10.99 ug/cm2 and 11.02±1.79 ug/cm2, respectively. Because dynamic changes of SIF are sensitive to the canopy chlorophyll content, we further checked the correlation between retrieved Cab and the chlorophyll content index. MODIS (Moderate Resolution Imaging Spectroradiometer) surface reflectance data (MOD09A1, 500 m spatial resolution and eight days temporal resolution) was downloaded and used to calculate the green chlorophyll index ($CI_{green} = R_{nir\ band} / R_{green\ band} - 1$), which is highly correlated with chlorophyll content (Gitelson et al. 2005). We used a linear regression model to check the correlation between retrieved Cab and $CI_{green}$ (Figure 2.3). As the coefficient of determination was 0.9 and p-value < 0.01, we confirmed that the GPR model-predicted Cab could be used as a key parameter for model simulations. In the next section, we generated daily biochemical parameter and EF-matrices through interpolation and applied these for model simulation.

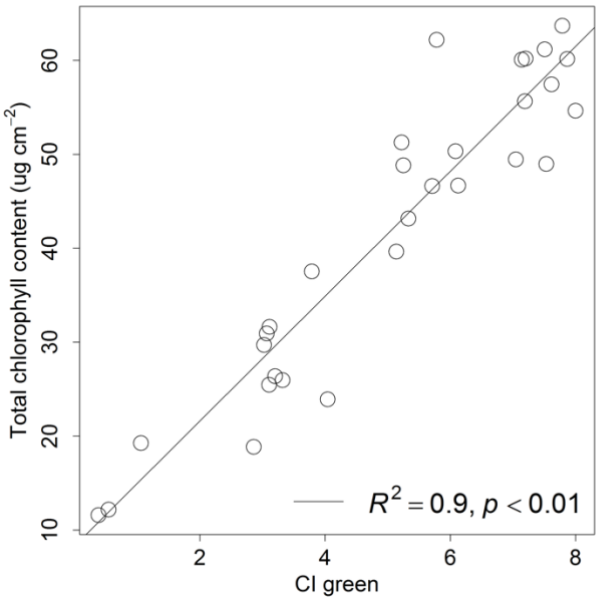


Figure 2.3. Correlation between the green chlorophyll index, $CI_{green}$, and total chlorophyll content.

### 2.4.2. Comparison of simulated SIF with field measured canopy SIF under different sunlit & cloudy light conditions

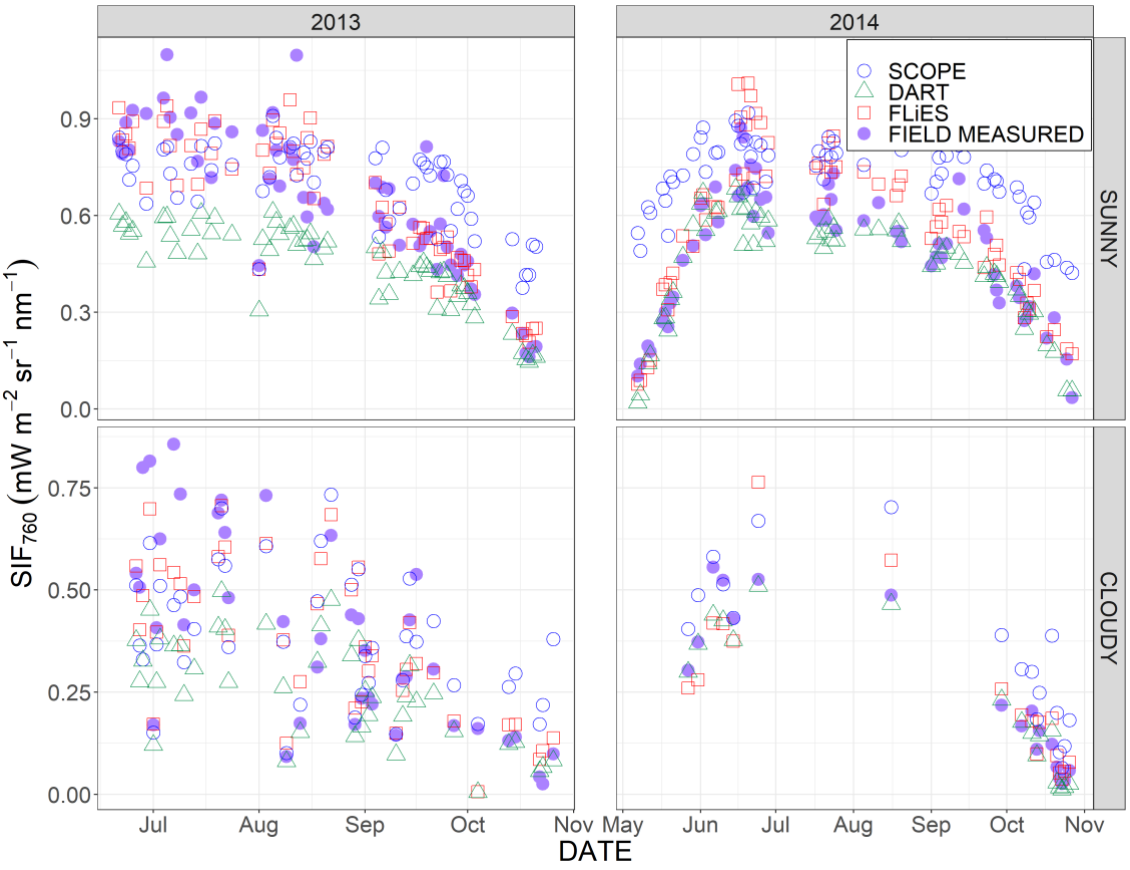


Figure 2.4. The seasonal change of field measured canopy SIF, with FLiES$_{SIF}$, DART$_{SIF}$ and SCOPE$_{SIF}$ at 760 nm from 2013 to 2014.

Daily field measured SIF was compared with FLiES$_{SIF}$, DART$_{SIF}$ and SCOPE$_{SIF}$ SIF retrievals at 760 nm from 2013 to 2014 under different light conditions (Figure 2.4). Cloudy-day field measurements were mainly taken in 2013. All simulated SIF agreed well with the measured canopy SIF from 2013 to 2014 and they showed an obvious seasonal trend. Model simulated SIF decreased from July 2013 until the end of that year and the start of the season was from May 2014. In the middle of June 2014, all simulated SIF reached the peak at the same time as SIF$_{Field}$ and commenced to drop again around September 2014. In sunny days of 2013, DART$_{SIF}$ was lower than SIF$_{Field}$, while FLiES$_{SIF}$ and SCOPE$_{SIF}$ showed similar patterns with the SIF$_{Field}$. However, DART$_{SIF}$ and FLiES$_{SIF}$ agreed well with the SIF$_{Field}$ in both sunny and cloudy days of 2014, and SCOPE$_{SIF}$ was a little higher than the field SIF measurements during the sunny days in 2014. The yearly average of FLiES$_{SIF}$ was 0.51±0.25 mW/m2/sr/nm, DART$_{SIF}$ was 0.37±0.17

mW/m2/sr/nm, SCOPESIF was 0.59±0.21 and SIFField was 0.5±0.24 mW/m2/sr/nm as shown in Figure 2.5 The range of FLiESSIF and SCOPESIF was similar to the SIFField in both sunny days and cloudy days.

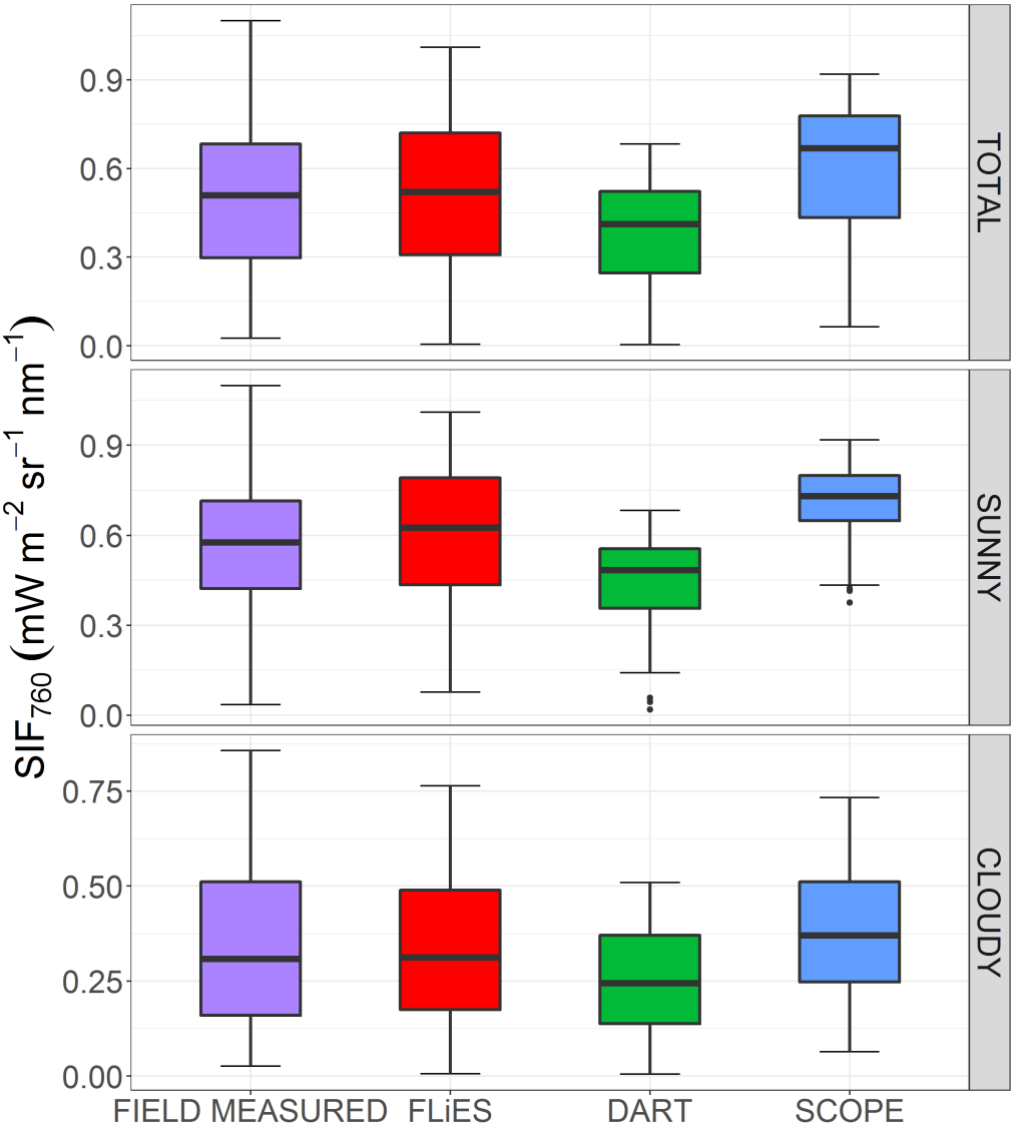


Figure 2.5. Box plot for SIF annual mean and range of SIFField, FLiESSIF, DARTSIF and SCOPESIF.

The correlation between model-simulated SIF and field measured SIF was checked using linear regression (Figure 2.6). The coefficient of determination of FLiESSIF ($R_2$ = 0.8, $p < 0.001$) was higher than other model simulated ($R_2$ = 0.76, 0.56 for DART and SCOPE model, respectively), which presented strong correlation with field measured SIF. The RMSE of FLiESSIF (RMSE = 0.12 mW/m2/sr/nm) was lower than DARTSIF and SCOPESIF (RMSE = 0.17 and 0.2 mW/m2/sr/nm, respectively).

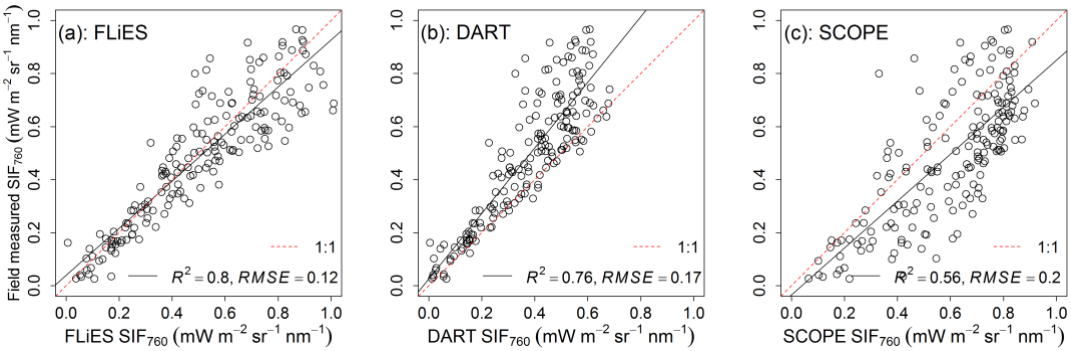


Figure 2.6. The correlation between $SIF_{Field}$ and $FLiES_{SIF}$, $DART_{SIF}$, $SCOPE_{SIF}$. (a) Correlation between $FLiES_{SIF}$ and $SIF_{Field}$. (b) Correlation between $DART_{SIF}$ and $SIF_{Field}$. (c) Correlation between $SCOPE_{SIF}$ and $SIF_{Field}$. The red dash line is the 1:1 symmetric line, all p-value < 0.001.

Due to SIF sensitivity with PAR, we further checked the SIF simulation for sunny and cloudy days. Normally, SIF will increase with increasing irradiance, however SIF will also change slightly when light becomes saturating. Hence, simulating SIF for different light condition is critical to the understanding of the SIF mechanism. The results as Table 2.3 showed all models were highly correlated with the $SIF_{Field}$ for both sunny and cloudy days. Interestingly, the correlation of simulated and measured SIF for clear sky was weaker than for cloudy days. The RMSE for cloudy days from each model yielded the same weaker correlation. Even for the SCOPE model, the $R_2$ and RMSE for the cloudy days have better performance than total simulated and sunny day SIF. This implies modelling SIF should consider the light saturation.

Table 2.3. Correlation of determination of FLiES model, DART model, and SCOPE model simulated SIF with field measured SIF for sunny days and cloudy days, all p-value are less than 0.001.

| | FLiES $SIF_{760}$ | | DART $SIF_{760}$ | | SCOPE $SIF_{760}$ | |
|---|---|---|---|---|---|---|
| | $R_2$ | RMSE | $R_2$ | RMSE | $R_2$ | RMSE |
| Total | 0.80 | 0.11 | 0.76 | 0.17 | 0.56 | 0.20 |
| Sunny days | 0.74 | 0.12 | 0.68 | 0.17 | 0.47 | 0.21 |
| Cloudy days | 0.80 | 0.10 | 0.76 | 0.16 | 0.62 | 0.14 |

### 2.4.3. The correlation between $GPP_{EC}$ and SIF in sunny or cloudy days

Figure 2.7 shows the correlations between daily $GPP_{EC}$ with model simulated SIF and measured SIF at 760 nm for different light conditions from 2013 to 2014. SIF simulated by three-dimensional models were highly correlated with the $GPP_{EC}$, $R_2$ of $FLiES_{SIF}$ = 0.73 and $DART_{SIF}$ = 0.69 (all p-value < 0.001), respectively. Compared with the correlation of $SIF_{Field}$ and $GPP_{EC}$ ($R_2$ = 0.67), the results were similar. All measured or simulated SIF in cloudy days showed a slightly stronger correlation with the $GPP_{EC}$ than in sunny days. In sunny days, $FLiES_{SIF}$ presented the highest $R_2$ with $GPP_{EC}$ ($R_2$ = 0.78); in cloudy days, $DART_{SIF}$ showed the highest $R_2$ with $GPP_{EC}$ ($R_2$ = 0.85). Interestingly, the SIF from FLiES and DART models estimated higher GPP values for cloudy days than for sunny days (Figure 2.7 (a), (b)).

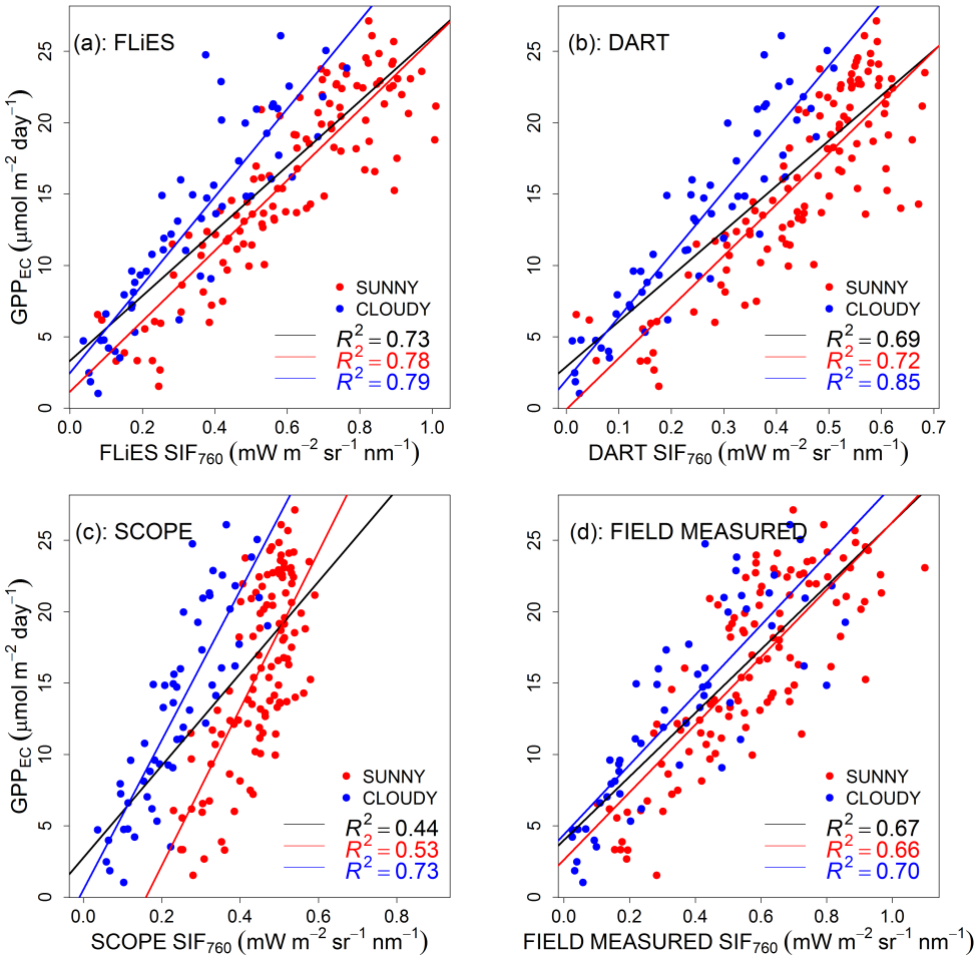


Figure 2.7. The correlation between daily $GPP_{EC}$ and model simulated daily SIF under different light conditions (a) – (d). Black lines, red lines and blue lines are regression line for total SIF, SIF in sunny days and cloudy days, respectively. Red points mean

measurement in sunny days, blue points mean measurement in cloudy days. All p values are less than 0.001.

## 2.5. Discussion

### 2.5.1. Model sensitivity

Simulated SIF was primarily affected by vegetation structure and light conditions. Figure 2.8 shows the correlation matrix between FLiESSIF, biochemical parameters and vegetation structure. Among different factors, FLiESSIF is mostly correlated with APAR ($R_2$ = 0.919), suggesting that SIF is mainly driven by APAR, which is consistent with previous findings (Yang et al. 2015b). FLiESSIF is also highly correlated with biochemical parameters, especially chlorophyll content ($R_2$ = 0.658). Within certain limits, SIF increased with higher chlorophyll contents until SIF saturated at higher chlorophyll contents (Porcar-Castell et al. 2014; Yang et al. 2015b), thus inhibiting stronger SIF correlations with chlorophyll content.

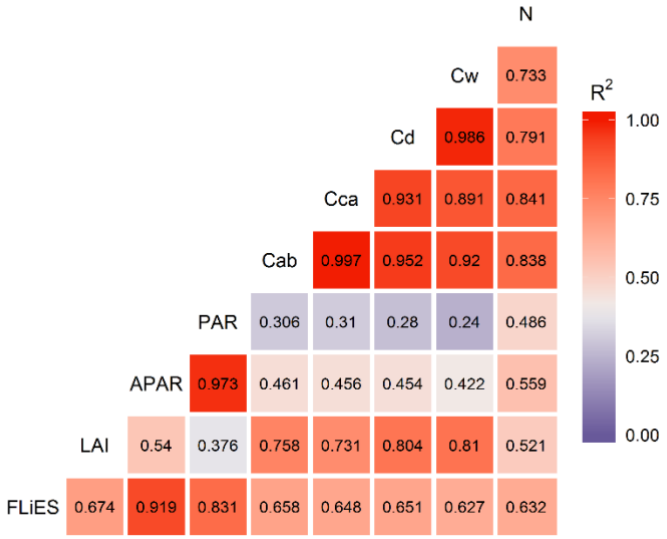


Figure 2.8. Correlation matrix between FLiESSIF and other factors, all p-values are less than 0.001.

LAI influences on SIF simulation were weaker ($R_2$ = 0.67) than meteorological and biochemical factors. Normally, with increasing PAR, the field or satellite sensor should detect the SIF signal more easily, but this situation is more complicated across the different growth phases (PAR~LAI, $R_2$ = 0.37, Figure 2.8). For example, during the 2014 growing season PAR reached its maximum value in May, but the green leaf phenology

of vegetation at Harvard forest just started with chlorophyll content and LAI changing rapidly, while the SIF signal was still very weak (SIF < 0.4 mW/m2/sr/nm, PAR = 2000 µmol/m2/sec, LAI = 3) (Figure 2.9). Therefore, SIF is more correlated with leaf structure (LAI) than radiation (PAR) during the growing season. At the peak of the growing season (July – August 2014), LAI was stable while PAR started to decrease and SIF gradually decreased (Figure 2.9). Hence, at this stage, PAR replaced LAI as the main controlling factor of SIF. In summary, at the seasonal scale, different driving factors affected SIF over different growth phases for this deciduous broadleaf forest.

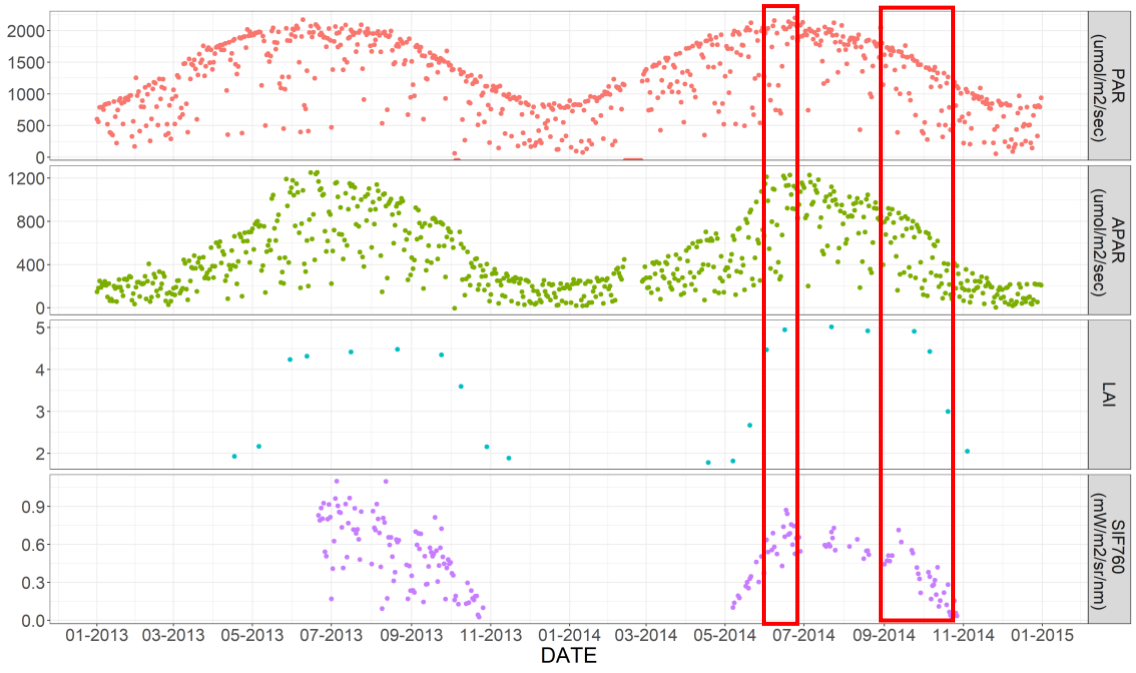


Figure 2.9. Time series of PAR, APAR, LAI and field measured SIF from 2013 to 2014. PAR, APAR, LAI and SIF are all from field measurements.

## 2.5.2. The relationship between GPP and scattered vs emitted SIF

The difference of fluorescence observed from leaf and canopy is that SIF consists of emitted and scattered SIF at the canopy scale, while the SIF signal only contains emitted SIF at the leaf scale. This is particularly true for far-red SIF at 760 nm, due to much lower re-absorption compared with the red SIF, where the scattering effect is more easily observed. As $SIF_{760}$ contains information from both PSI and PSII (Baker 2008), it is critical to understand which part of the far-red SIF signal is more correlated with photosynthesis activity under different light conditions.

SIF yield and LUE were positively correlated (Figure 2.10 (a)), especially in sunny days. Schlau-Cohen & Berry (2015) indicated that SIF yield increased under clear sky and photosynthesis capacity also increased. Similarly, we can see a significant correlation between scattered and emitted SIF under clear sky (Figure 2.10 (b), (c). $R_2$ = 0.34 and 0.25, respectively). In cloudy days, SIF yield, scattered and emitted SIF presented non-significant patterns with LUE (p-value > 0.05). (Miao et al. 2018) indicated that SIF yield was positively correlated with LUE in cloudy days at seasonal scale, but limited observations of days, growing phase and different vegetation types may impact on its correlation (Pearcy 1990). In our study, it can be seen that SIF yield showed higher values in cloudy days than in sunny days and SIF yield increased with increasing diffuse radiation (Gu et al. 2003). SIF yield contains less information of LUE and APAR because the fluorescence yield represents a small portion, about 1%, of the total quantum yield, and the complex relationship between SIF yield and LUE needs further research (Schlau-Cohen & Berry 2015).

For far-red SIF, the SIF yield showed a weak relationship with APAR ($R_2$ = 0.12), however, both scattered and emitted SIF showed significant correlations with APAR ($R_2$ = 0.64 and 0.72 for scattered SIF and emitted SIF, respectively) (Figure 2.10 (e), (f)). A strong APAR can trigger leaves to emit more fluorescence to some extent and increase fluorescence scattering. Scattered SIF in the far-red region is positively affected by canopy structure (Migliavacca et al. 2017; Yang & Van Der Tol 2018). The relationship of emitted SIF in sunny days was higher than on cloudy days ($R_2$ = 0.72 and 0.64, respectively). In summary, the higher APAR leads to higher SIF yield for deciduous broadleaf forest. The total SIF yield showed a positive relationship with APAR (Figure 2.10 (d)), which was also found in other vegetation types: soybean and grass (Miao et al. 2018; Verma et al. 2017).

Total SIF better captured GPP dynamics than scattered and emitted SIF (Figure 2.10 (g), (h), (i)). Relationships between scattered and emitted SIF with GPP did not show any obvious differences, as they were both strongly correlated with GPP under both sunny and cloudy days. We note that SIF more quickly responded to GPP for cloudy days than for sunny days (Figure 2.10 (g)) due to the SIF correlation with photosynthesis under higher diffuse radiation (Meroni et al. 2009). This implies that remotely sensed observed SIF may not provide a complete measure of the true relationship of SIF with GPP due the poor data quality under cloudy skies.

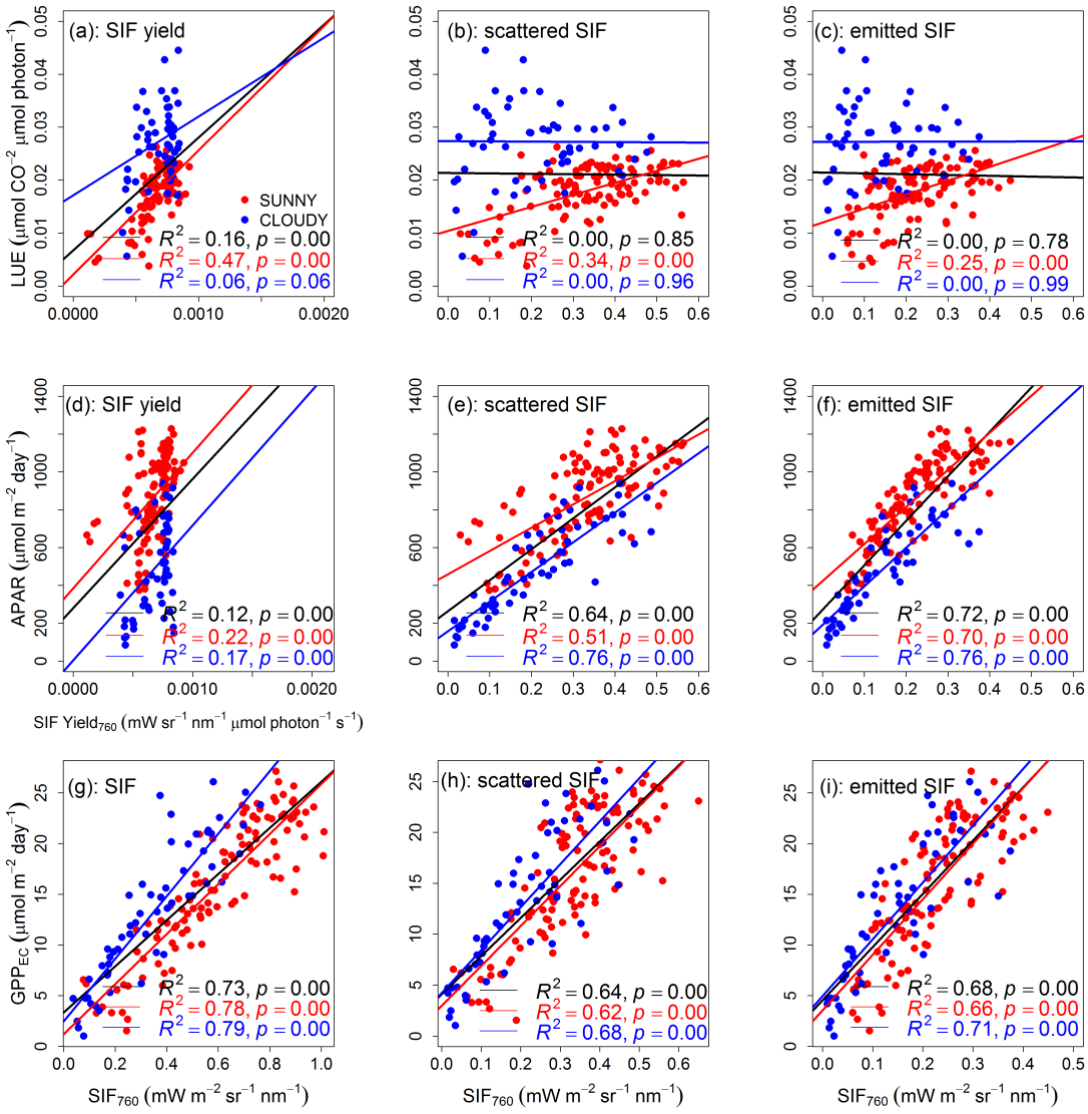


Figure 2.10. At the seasonal scale, the relationship between and each part of FLiES simulated SIF, LUE and APAR. Correlation of LUE and (a) daily SIF yield, (b) scattered SIF, (c) emitted SIF. Correlation of APAR and (d) daily SIF yield, (e) scattered SIF, (f) emitted SIF. Correlation of $GPP_{EC}$ and (g) field measured SIF, (h) scattered SIF, (i) emitted SIF. Red points mean measurement in sunny days, blue points mean measurements in cloudy days. The black line is the total regression line, red and blue line means the sunny and cloudy regression line, respectively.

### 2.5.3. Uncertainties of seasonal SIF simulations

Models can give us more information about SIF dynamic changes at seasonal and diurnal scales. One dimensional models focus on the flux changes and how multiple ecological factors influence SIF simulations, but ignore the complex and heterogeneous vegetation structures. Simulations from 3-D models can overcome these issues and potentially better

inform vegetation photosynthetic states and health through more realistic vegetation canopy modelling. The FLiES model as an open source and the three-dimensional radiative transfer model with a ray-tracing framework can be easily extended. The performance of FLiES-SIF model is stable and simulation results are with low RMSE compared with field measured data.

Comparisons of 1D model and 3D model running times and complexity of parameter settings would increase the difficulty of model usability. For the FLiES model, it only concerns radiative transfer and cannot support simulations of flux exchange and radiation balance. In other words, the progress of photosynthesis is not only related to the radiation and biochemical parameters, but also to temperature, leaf level photochemical processes, soil water content and meteorological impacts (Baker 2008). Extreme changes of these factors would result in vegetation stress with impacts on the photosynthesis capacity. Hence, modelling SIF for vegetation stress detection with 3-dimensional structure should consider the entire local environment in the future.

Moreover, we note that seasonal changes of SIF from the understory also contributes to the ecosystem photosynthesis (Kato et al. 2016), especially grass growth may be earlier than vegetation in the overstory layer and more sensitive to temperature and precipitation. Because of the lack of field measurements, we set the reflectance and transmittance from the understory layer to default values during the simulation, which may introduce uncertainties. On the other hand, although PAR light level dependence model coupled with a light correction factor ($\phi_f$) is applied in the model (Rosema et al. 1998), we still should consider complex light and plant health conditions impact on fqeI and fqeII (Schlau-Cohen & Berry 2015). In the future, retrieving fluorescence quantum efficiency will need to be applied in the simulations.

In summary, the FLiES model performance was equivalent or better than with the other models by using our retrieving method, but we cannot state that the DART model and SCOPE model does not work well in long-term SIF simulations. In order to test our new SIF module, we limited the input parameters of the DART and SCOPE models in order to keep the same input parameters with FLiES model. This may generate a bias and be the main reason for the simulation differences of these three models found in this study.

## 2.6. Conclusions

In this study, we developed a new SIF module for the FLiES model to enable 3-dimensional SIF simulations of complex canopy structures at seasonal scales. We performed a first time validation of the model using field seasonal measurements of SIF over a two-year period and we further compared our results with other, 2- and 3-dimensional models. Based upon validation with actual field measurements our newly developed SIF module and new parameter retrieval approach showed accurate and stable results in comparison with other models under both sunny and cloudy days. By retrieving biochemical parameters from Landsat data and vegetation structure from Airborne LiDAR data, this simulation framework provides an easy and accurate approach for simulating seasonal and long term SIF patterns, and for evaluating dynamic biochemical and radiation effects on SIF. Furthermore, we examined the relationship between "pure" SIF (emitted SIF) and scattered SIF with photosynthesis under different incoming radiation conditions, and found that the pure SIF could provide the information of photosynthetic function for different patterns of clear- and cloudy sky conditions. In the future, this model needs to be further evaluated and compared with SIF observations for different vegetation types, patterns of landscape heterogeneity, and multi-layer overstory/ understory vegetation structures. Further tests are also needed to assess model simulations of vegetation under extreme and stressed environments.

# Chapter 3. Partitioning sun-induced chlorophyll fluorescence into overstory and understory layers by using a three-dimensional model

## Abstract

Sun-induced chlorophyll fluorescence (SIF) has been used as an indicator of vegetation photosynthesis. It is useful for measuring seasonal photosynthetic efficiency in response to environmental stress, such as extreme heat and drought. Although some SIF devices have been deployed at the top of the canopy, as well as satellites (GOME-2 and OCO-2) which can monitor SIF continually, they cannot reveal the dynamic changes of understory SIF and how these contribute to local scale ecosystem carbon dynamics. A radiative transfer model was developed to study SIF emissions, however, this one-dimensional model assumes vegetation is homogeneous, and is unable to provide the vertically spatial distribution of SIF. The three-dimensional FLiES model with a newly developed SIF module, is now able to study the SIF emission in both overstory and understory layers and can improve our understanding of the understory SIF dynamics. In this study, a machine learning method was implemented to retrieve biochemical parameters from Sentinal-2 surface reflectance and generate the excited fluorescence matrices (EF-Matrix) and leaf spectrum. LiDAR data was further used to extract vegetation structure and position. We then used the FLiES-SIF model to partition SIF emissions into overstory and understory layers over three flux tower sites: Ti Tree East (AU-TTE), Litchfield (AU-LIT) and Cumberland Plains (AU-CUM) in Australia, representing shrubland, tropical savanna and evergreen forest, respectively. The results suggested that SIF from the understory layer contributed more than 51% of the total SIF in the wet season for the tropical savanna. However, the understory contribution was limited in the evergreen forest to only 10% of total SIF. We further examined the influence of canopy structure and incoming radiation on the SIF emission. The results showed that the understory SIF was highly correlated with PAR in sparse tree areas ($R_2$ = 0.64 and $R_2$ = 0.88 for AU-TTE and AU-LIT, separately). Over the higher-density canopy area of AU-CUM, the canopy cover showed a weak correlation with SIF emission ($R_2$ = 0.25). The relationships reported here will contribute to our understanding of how different layer's SIF vary from sparse to dense canopy covered areas.

## 3.1. Introduction

Sun-induced chlorophyll fluorescence is light re-emitted by chlorophyll molecules during the photosynthesis process. SIF has two peaks, one is at 685 nm, and contains the information of photosystem II (PSII). The other peak is at 740 nm (far-red SIF), which

contains information of both photosystems I and II (PSII). The far-red SIF is widely used to study the photosynthesis efficiency, heatwaves and drought (Li, Xiao & He 2018b; Sun et al. 2015b; Wang et al. 2016; Wieneke et al. 2018a), because of the low absorption of the leaf at far-red region (Porcar-Castell et al. 2014).

Recently, SIF has become a critical factor for determining the photosynthetic activity of vegetation. The strong relationship between SIF and gross primary productivity (GPP) has been confirmed by satellites (Joiner et al. 2013; Köhler, Guanter & Joiner 2015b) and field measurements (Miao et al. 2018; Nichol et al. 2019; Wieneke et al. 2018a; Yang et al. 2015b). OCO-2 data has been used to analyse the relationship between satellite SIF and eddy covariance GPP over 64 flux sites globally, and suggests that there is a nearly universal relationship between satellite SIF and GPP across a wide variety of biomes (Li et al. 2018). In addition, flux tower sites coupled with advanced devices (FluoSpec2, SIF-Sys), which can be deployed in the field to measure SIF, found SIF was more correlated with APAR than GPP, and it demonstrated SIF carried APAR information. Even in different light conditions, SIF shows a different pattern with GPP across different vegetation types (Yang et al. 2015b). Thus we can predict GPP for overstory and understory by using the strong linear relationship between SIF and GPP.

Normally, observations of SIF are concentrated on the top of canopy (TOC), and the seasonality of understory SIF remains uncertain. The lack of knowledge of seasonality change of understory SIF may underestimate the contribution of understory species to total ecosystem carbon dynamics (Kato et al. 2016). Hence, in order to better represent ecosystem function and predict ecosystem response to disturbances and future climate change, it would be advantageous to partition the energy flux into overstory and understory layers, and further investigate the response of the two vegetation layers to environment factors (Misson et al. 2007).

Savannas as the classical tree-grass type, bring much focus about the energy flux from different layers (Walker & Gillison 1982). Furthermore, savannas play an essential role in the global carbon cycle. They accounted for 30% of GPP of all terrestrial ecosystem (Kanniah et al. 2009). This is especially evident in Australia, where savanna areas occupy one-quarter of the Australian continent (Hutley, O'grady & Eamus 2000). Savannas have a particular tree-grass structure. In the overstory layer, the canopy cover is sparse and discontinuous, however, the understory layer consists of shrub and grass and it usually can be defined as a continuous and heterogenous layer (Whitley et al. 2011).

Savanna productivity is primarily influenced by solar radiation, precipitation and fire (Beringer et al. 2003; Moore et al. 2016). Australian savanna areas receive a large amount of solar radiation. Whitley's study showed the effectness of light interception on savanna GPP is a much more important influence than water supply (Whitley et al. 2011). However, to what extent the radiation contributes to the understory layer is still the remaining issue for savanna areas (Moore et al. 2016). Precipitation is also an essential factor that affects savanna vegetation. The C4 grasses in the understory layers grow rapidly in the wet season (Moore et al. 2016). Fire, when it occurs in savanna would reduce the growth of trees and affects carbon storage (Beringer et al. 2015; Beringer et al. 2007).

Based on the previous study, field measurements, satellite observations and models are the main research tools to study the partitioning energy into overstory and understory layers. Moore et al. (2016) were the first to use two flux towers to separate GPP of tree and grass for a tropical savanna in Australia, and they found the understory contribution had strong seasonality and contributed more GPP in the wet season. Recently, they used the DIFFUSE model and remote sensing data to separate GPP of trees and grass for long-term periods (Moore et al. 2018). Similarly, Whitley et al. (2011) used the SPA model to partition the energy flux into the overstory and understory layers, and they found the understory C4 grass contributed nearly 38% to total GPP.

Field measured SIF has also been used to partition SIF emissions into different vertical layers. The upward measurements of the overstory SIF and understory SIF were examined in a cool temperate forest in Japan (Kato et al. 2018; Kato et al. 2016). The results showed a substantial contribution of the understory in upward SIF, which may indicate less photoinhibition relative to the overstory. However, the partitioning of SIF in overstory and understory layers for different biomes has remained mostly unexplored.

In order to get a better understanding of SIF emissions under different environmental conditions, researchers have developed the one-dimensional model and three-dimensional model to simulate SIF. The SCOPE (Soil Canopy Observation Photochemistry and Energy fluxes) model, as the most widely used and famous one-dimensional model is used to simulate leaf fluorescence emission at TOC and energy flux for the homogeneous canopies (Van der Tol et al. 2009). However, this one-dimensional model cannot identify the SIF signal from the overstory or understory. It is also unable to

simulating SIF emission from vegetation with horizontal and vertical heterogeneity (Porcar-Castell et al. 2014).

Advanced three-dimensional models can overcome the drawbacks of the one-dimensional model. The DART model, FluorWPS and FluorFLIGHT are three-dimensional radiative transfer models and are based on the Monte Carlo method and ray-tracing theory (Gastellu-Etchegorry et al. 2017; Hernández-Clemente et al. 2017; Zhao et al. 2016). They both relied on the FLUSPECT model generating excited fluorescence matrices (EF-Matrix) for PSI and PSII. The DART model has been used to study the diurnal change of SIF for crops while the FluorWPS model studied the SIF emission for row crops. FluorFLIGHT coupled with classical 3D model FLIGHT has studied the health conditions for forests and found that SIF signal is influenced by canopy structure (Hernández-Clemente et al. 2017).

The FLiES (Forest Light Environmental Simulator) model, as an open source, three-dimensional and ray-tracing model can be extended and has been successfully applied in forest and savanna areas (Kobayashi & Iwabuchi 2008). In the previous chapter, we developed a SIF module for the FLiES model and a new method of retrieving key parameters by the machine learning method. We validated SIF simulation with observations in a temperate forest. The results showed that the performance of the new SIF module is excellent and with lower root mean square error (RMSE), and found a strong correlation with observed SIF in the far-red region.

In this study, we aimed to use the finest resolution satellite surface reflectance to retrieve the critical biochemical data and used a three-dimensional model to partition the overstory and understory SIF. Our objectives were to (i) identify the pattern of SIF emissions in the overstory and understory layers among open shrubland, tropical savanna and evergreen broadleaf forest; (ii) estimate the GPP of different vegetation types, and partition them into overstory and understory, and discuss how they vary seasonally; (iii) examine the factors that would affect the overstory and understory SIF emissions. This research will be useful for understanding how different layer's SIF vary and contribute to different canopy covers across several biomes.

## 3.2. Study area and Data

### 3.2.1. Study area

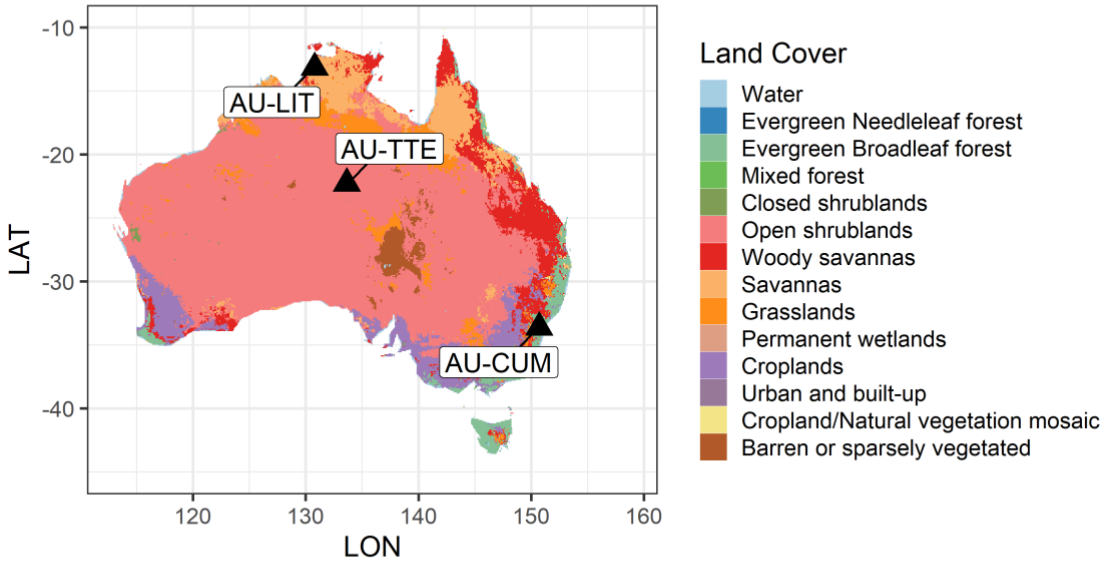


Figure 3.1 The land cover of three flux tower sites in Australia. The land cover data used MCD12C1.

We chose three study sites that are around flux tower sites (Figure 3.1). One site, Ti-Tree east (AU-TTE), is located in the centre of Australia (22°17′S, 133°38′E) at an elevation of 553 m above sea level. AU-TTE is dominated by grassy mulga woodland and Corymbia savanna (Eamus et al. 2013). The average height of the canopies is 4.85 meters. The temperature and mean annual precipitation is around 35 degree Celsius and 443 mm, respectively.

Litchfield (AU-LIT) is in the Litchfield National Park in the Northern Territory, Australia (13°10′S, 130°47′E). Its vegetation type is tropical savanna. The elevation of AU-LIT is 220 m above sea level, and annual precipitation is 1737 mm. The understory is C4 grass.

The third site is the Cumberland Plain (AU-CUM), which is located west of Sydney (33°36′S, 150°43′E). The elevation of this site is 20 m above sea level. The canopy is dominated by Eucalyptus moluccana and Eucalyptus fibrosa with an average height 20

meters at the canopy. The mean annual temperature and precipitation is 24 degree Celsius and 800 mm, respectively. The vegetation type is an evergreen broadleaf forest.

The AU-TTE and AU-CUM sites were both activated in 2012 and AU-LIT was established in 2015. They provided measured ground heat flux, radiation, wind speed, barometric pressure, air temperature and open path $CO_2$ and $H_2O$ exchanges.

### 3.2.2. LiDAR data

LiDAR data is used to retrieve vegetation structure and position on the spatial scale. LiDAR data is the surface reflection, a remote sensing method where an airborne laser is pointed at a targeted object on the ground, rapid pusles of light are fired and the beams of light are measured by the time they take to bounce back to the sensor (Jaboyedoff et al. 2012). Hence, LiDAR consists of cloud points of vegetation on the ground. Aus Tern provides lidar data, and Litchfield was surveyed in 2013, Ti Tree East in 2014, and Cumberland Plain in 2015. We assumed that vegetation in these areas was mature and the extreme change of height and crown could be ignored.

We used the Canopy Height Model (CHM) (Pitkänen et al. 2004) to separate vegetation layer and ground layer. The vegetation layer contains the height of each cloud point. Then we used the crown detect method to locate the crown of each vegetation and extract each crown's height, radius and positions.

### 3.2.3. GOME-2 SIF

In this study, the GOME-2 data v27 level 3 chlorophyll fluorescence from MetOp-A (spatial resolution is 40 km) at 740 nm was used for validating the model simulations. The level 3 data have had filtering applied including cloud fractions of up to 30% and solar zenith angles of less than 70 degrees. Data was extracted at the coordinates of each flux site.

### 3.2.4. Sentinel-2 reflectance

The AU-TTE and AU-LIT sites are a mixture of tree and grass. Normally, the Landsat pixel (30 meters spatial resolution) and even more coarse data (MODIS) may hide seasonal tree and grass changes. Sentinel-2, as the finest spatial resolution sensor, is suitable and available to analyse tree-grass and minimise the influence from mixed tree-grass pixels.

The Sentinel-2 satellite, launched in 2013, provides 13 spectral bands from visible and near-infrared to the shortwave infrared. The temporal resolution is usually around 15 days under cloud-free conditions (Drusch et al. 2012).

We used Sentinel L1B reflectance data (ten bands, Band 1 to Band 9) to retrieve vegetation biochemical parameters, bands spatial resolutions were 10, 20 and 60 meters, respectively. Because the plant function type of pixels around the flux tower site are homogeneous, we assumed that the different spatial resolution of Sentinel-2 bands less impacted on the retrieving of biochemical parameters. As the reflectance of L1B was measured at the top of the atmosphere, we implemented the sen2cor tool to convert L1B to L2A level data and processing atmosphere correction. In order to keep the best quality of measurements, we constrained the cloud thickness equals to zero.

### 3.2.5. MODIS EVI data

Enhanced vegetation index (EVI) is widely used as proxies of canopy "greenness", an effective factor indicating vegetation green leaf area, green foliage cover and leaf chlorophyll content (Huete et al. 2002). EVI data was collected from MOD13Q1 006 from 2016 to 2017. The spatial resolution is 250 m, and the temporal resolution is 16 days. At each flux tower site, we extracted the pixels to match the footprint of the flux site. Quality control was implemented to remove the pixels contaminated by clouds or aerosols using quality flags.

The equation defining EVI is:

$$EVI = G * \frac{NIR - RED}{NIR + C_1 * RED - C_2 * BLUE + L} \quad (3\text{-}1)$$

Where, NIR, RED and BLUE represents near infrared band, red band and blue band, separately. Coefficients are including $G$ = 2.5, $C_1$ = 6, $C_2$ = 7.5 and $L$ = 1.

### 3.2.6. Eddy covariance data

The Eddy covariance data of each flux site are provided by the OZFLUX network (http://www.ozflux.org.au). The data processing included quality control assessment, removal outlier observations, correction for low turbulence periods and gap filling. We collected the daily GPP data in level 6, it calculated by Lloyd–Taylor respiration model (Lloyd & Taylor 1994).

$$R_{eco} = R_{ref} \exp\left(E_0 \left(\frac{1}{T_{ref} - T_0} - \frac{1}{T - T_0}\right)\right) \quad (3\text{-}2)$$

$$GPP = NEE - R_{eco} \quad (3\text{-}3)$$

In equation 3-2, $T_{ref}$ = 10°C is the reference temperature, $T_0$ = -46.04°C is the model parameter chosen by Lloyd and Taylor to fit their soil respiration data, $R_{ref}$ is the base respiration rate at the reference temperature, $E_0$ is the activation energy and $R_{eco}$ is the ecosystem respiration, NEE is the net ecosystem exchange of carbon. Furthermore, downward incoming photosynthesis activated radiation (PAR) of each site was collect for model simulation.

## 3.3. Methodology

This section briefly describes the frame of SIF simulation and a machine learning method, which used to retrieve parameters from remotely sensed data.

### 3.3.1. FLiES SIF model

#### 3.3.1.1. Vegetation structure

The simulation scene was defined as a space of 30 * 30 $m^2$. It consisted of four layers: atmosphere layer, vegetation layer, floor layer and soil layer. In the vegetation layer, crowns and trunks were defined as geometric shapes. We used a cylinder to represent the vegetation's trunk and an ellipsoid for the crowns. The height of the trunk and radius of crowns were retrieved from LiDAR data. In the floor layer, we assume the distribution of grass is uniform. We defined that the vegetation height above one meter belonged to the overstory layer, below one meter was in the understory layer.

#### 3.3.1.2. Model frame

FLiES model (version 2.48) is a three-dimensional radiation transfer model (Kobayashi & Iwabuchi 2008). It based on the Monte Carlo method and implemented a large of photons which distribute uniformly above the scene. Then the random method is used to generate each photon's direction. When scattering occurred, the model will count how much energy is lost and absorbed by the leaf.

We developed a new SIF module for the FLiES model as a previous chapter described. Based on the original photon ray-tracing frame, we separated the photon as non-fluorescence and fluorescence photon. For the non-fluorescence photon, its simulation

followed the original ray-tracing framework. However, for the fluorescence photon, the newly developed module would calculate each photon's scatter direction, and emitted fluorescence which was activated by the incoming non-fluorescence and fluorescence photon. Before the simulation, we applied pre-tracing progression for calculating the fluorescence correction factor and how much PAR reached leaf (Rosema et al. 1998; Zhao et al. 2016), because the fluorescence correction factor changes by the incoming photosynthetic active radiation (PAR).

### 3.3.2. Machine learning

In order to retrieve biochemical parameters, including total chlorophyll content, Carotenoid content, water content, dry matter content and leaf structure (Cab, Cca, Cw, Cd, N), machine learning is implemented to build a connection between biochemical parameters and reflectance. The finest resolution of Sentinel-2 MSI was used in building the relationship. We extracted ten bands B1 to B9 (443 – 945 nm), resolution ranging from 10 m to 60 m. We applied the Gaussian Process Regression (GPR) model to establish a relationship between the Sentinel-2 surface reflectance and biochemical parameters. Radial-Basis Function (RBF) was selected as the GPR's kernel as below,

$$k(x_i, x_j) = \exp\left(-\sum_{b=1}^{B} \frac{\|x_i - x_j\|^2}{2\sigma^2}\right) \quad (3\text{-}4)$$

where $\sigma$ is the length scale, which controls the spread of the relations for the spectral band, B is the number of bands, $x_i$ is the reflectance of each spectrum.

Table 3.1. GPR trained and validated results

| | Training group | | Validation group | |
|---|---|---|---|---|
| | $R_2$ | RMSE | $R_2$ | RMSE |
| N | 0.95 | 0.089 | 0.98 | 0.028 |
| Cab | 0.92 | 3.5 | 0.97 | 2.764 |
| Cca | 0.92 | 2.3 | 0.91 | 1.7 |
| Cw | 0.93 | 0.003 | 0.91 | 0.003 |
| Cd | 0.91 | 0.0018 | 0.95 | 0.0012 |

We selected Angers (Angers 2003) (Jacquemound et al. 2003) and LOPEX (LOPEX 1993) (Hosgood et al. 1995) leaf database for GPR to generate the prediction model. These two

databases contain a variety of plant species' leaf spectrum and bio-parameters (Zhang et al. 2014). We divided 80% of the leaf database as training group and 20% as a validation group and applied a ten fold cross-validation to get the prediction model with the lowest RMSE. **Error! Reference source not found.** showed the training results and validation results. All prediction results significants are below 0.001.

### 3.3.3. Structure of model simulations

Before simulation, we overlayed a 3 * 3 net, which contained nine pixels and each pixel was 30 * 30 $m^2$, over each flux tower site, with the flux tower site at the centre of the net. Also, we chose a pixel around the net with no canopy cover and defined it as a grass pixel. The retrieved results were used in the model as the understory layer.

Table 3.2. Settings for FLiES-SIF model

| Variable | FLiES model settings |
|---|---|
| Simulation area | 30 $m^2$ |
| Solar zenith angle | Calculate as the local time 9:30 am |
| PAR | Field measured |
| LAI | MODIS |
| Biochemical parameters | GPR model |
| EF-matrix | FLUSPECT model |
| Fluorescence quantum efficiency for PSI and PSII (fqeI, fqeII) | 0.002, 0.01 |
| Leaf angle distribution | Uniform distribution |
| Crowns shape | ellipsoid |

Our simulation consists of two steps (Figure 3.2); one is preparing input parameters; the other step is deploying the model. Regarding the preparation of input parameters, firstly we retrieved shapes of the targeted vegetation from LiDAR data in each sample pixel. Secondly, we extracted each sample pixel's Sentinel-2 reflectance and used the GPR model to predict five bio-parameters. Then, we used five bio-parameters to generate leaf spectrum, including reflectance and transmittance, using a Prospect-5 model and EF-matrices from a Fluspect model. Last but not least, we used the FLiES SIF model to simulate SIF in AU-TTE, AU-CUM and AU-LIT, and compared model simulation results

with remote sensing data and eddy covariance data. The input parameters for the FLiES model are listed in Table 3.2.

Linear regression was used to generate a prediction function of total SIF and GPP. Because of the high correlation between GPP and SIF, we used the prediction function to predict overstory GPP and understory GPP from overstory SIF and understory SIF, respectively.

Regarding deployment of the model, we set 1000000 photons for each simulation, as it provides simulation results close to reality. Also, we set the sensor at the nadir view to be the same as the GOME-2 observations, in order to compare the results between model and satellite. We used MODIS LAI (MOD15A2H) data as the scale factor for adjusting canopy area (Wu, Kobayashi, et al. 2018). Settings of atmosphere layer for FLiES model were used default values (Kobayashi & Iwabuchi 2008).

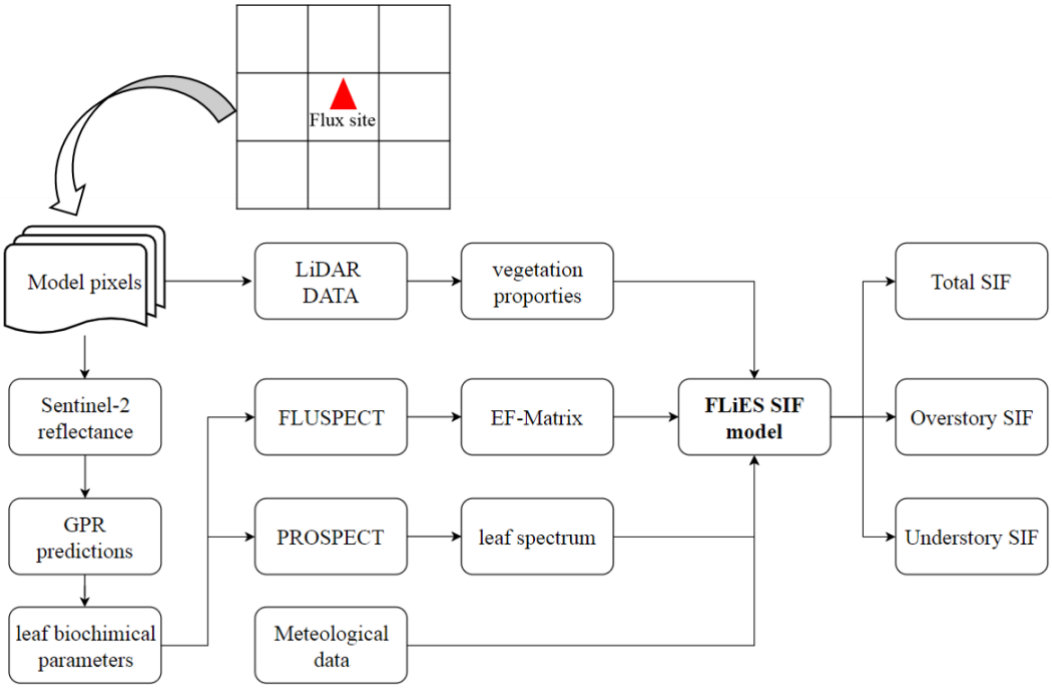


Figure 3.2. Flowchart of simulations.

## 3.4. Results

We simulated SIF ($SIF_{FLiES}$) from 2016 to 2017 by the FLiES model coupled with the newly developed SIF module and compared results with $GPP_{EC}$, MODIS EVI and GOME-2 SIF ($SIF_{GOME-2}$). We also checked the correlation between $GPP_{EC}$ and $SIF_{FLiES}$ for different layers. Finally, we predicted GPP by SIF.

### 3.4.1. Compare model simulated SIF, MODIS EVI, eddy covariance GPP and GOME2 SIF

Figure 3.3 (a) – (c) shows model simulated SIF, MODIS EVI, eddy covariance GPP and GOME2 SIF for AU-TTE, AU-LIT and AU-CUM from 2016 to 2017. AU-TTE, $SIF_{FLiES}$ showed a similar pattern of seasonality with EVI and $GPP_{EC}$ (Figure 3.3 (a)). From December 2016, $SIF_{FLiES}$ started increasing at the same rate as EVI and $GPP_{EC}$. They both reached the peak in February 2017 ($SIF_{FLiES}$ = 0.35 mW/m2/sr/nm, $GPP_{EC}$ = 5 g C/m2/day and EVI = 0.19), then they dropped until the end of 2017. $SIF_{FLiES}$ and $GPP_{EC}$ kept stable from July 2017 to December 2017. We could see the $SIF_{GOME-2}$ fluctuated between 2016 to 2017 (ranging from 0.09 to 0.6 mW/m2/sr/nm), implying that the coarse spatial resolution would effect the representation of the true SIF situation. Interestingly, in the dry season (besides Jan 2017 to Mar 2017), the understory $SIF_{FLiES}$ was similar to overstory $SIF_{FLiES}$. Hence, it indicated that vegetation in both overstory and understory contribute similarly to the local ecosystem in the dry season.

AU-LIT, $SIF_{FLiES}$, EVI, $GPP_{EC}$ and $SIF_{GOME-2}$ presented similar seasonal patterns from 2016 to 2017 (Figure 3.3 (b)). All factors increased gradually from October 2016 to January 2017. They both kept stable over the next two months and then started to decrease almost at the same time. In October 2017, $GPP_{EC}$ dropped to the lowest point ($GPP_{EC}$ = 1.25 g C/m2/day) and started to increase and were followed by $SIF_{FLiES}$, EVI and $SIF_{GOME-2}$. Compared to AU-TTE, the $SIF_{GOME-2}$ trend is much smoother in AU-LIT because the vegetation is homogeneous in AU-LIT and the pixels of GOME-2 contain mostly the same vegetation types. The overstory $SIF_{FLiES}$ and understory $SIF_{FLiES}$ showed a different pattern in both dry and wet seasons. The trend of the overstory $SIF_{FLiES}$ was flat and the value ranged from 0.1 to 0.2 mW/m2/sr/nm. The understory $SIF_{FLiES}$ ranged from 0.01 to 0.28 mW/m2/sr/nm. In the wet season, the overstory $SIF_{FLiES}$ and understory $SIF_{FLiES}$ were close to each other, but in the dry season, the understory $SIF_{FLiES}$ retained much lower values than the overstory $SIF_{FLiES}$.

AU-CUM, $GPP_{EC}$ displayed weak seasonality (Figure 3.3 (b)) because of its vegetation type is an evergreen broadleaf forest. EVI fluctuated from 2016 to 2017, however, the range was limited to 0.312 and 0.39. Even EVI showed an inverse trend, which compares to $SIF_{GOME-2}$ between January 2017 and December 2017. The understory $SIF_{FLiES}$ was lower than the overstory $SIF_{FLiES}$ and the trend was stable. It did not present an obvious

seasonal pattern. Hence, in this site, overstory $SIF_{FLiES}$ were mainly contributing to the GPP. Total $SIF_{FLiES}$ ranged from 0.12 to 0.82 mW/m2/sr/nm between 2016 to 2017, $SIF_{GOME-2}$ ranged from 0.1 to 0.81 mW/m2/sr/nm.

Compared to AU-CUM, the model simulated SIF showed clear seasonality in AU-TTE and AU-LIT. At the season of the peak, $SIF_{FLiES}$ in AU-CUM (SIF = 0.85 mW/m2/sr/nm) was higher than $SIF_{FLiES}$ in AU-TTE and AU-LIT. AU-TTE and AU-LIT, EVI showed a similar pattern to SIF; however, the pattern of EVI fluctuated and there was difference in the $GPP_{EC}$ in AU-CUM (Figure 3.3 (c)). This implies that SIF might replace EVI as an indicator of phenology in evergreen forest. However, EVI and SIF were both sensitive to the seasonal change in GPP in the savanna area.

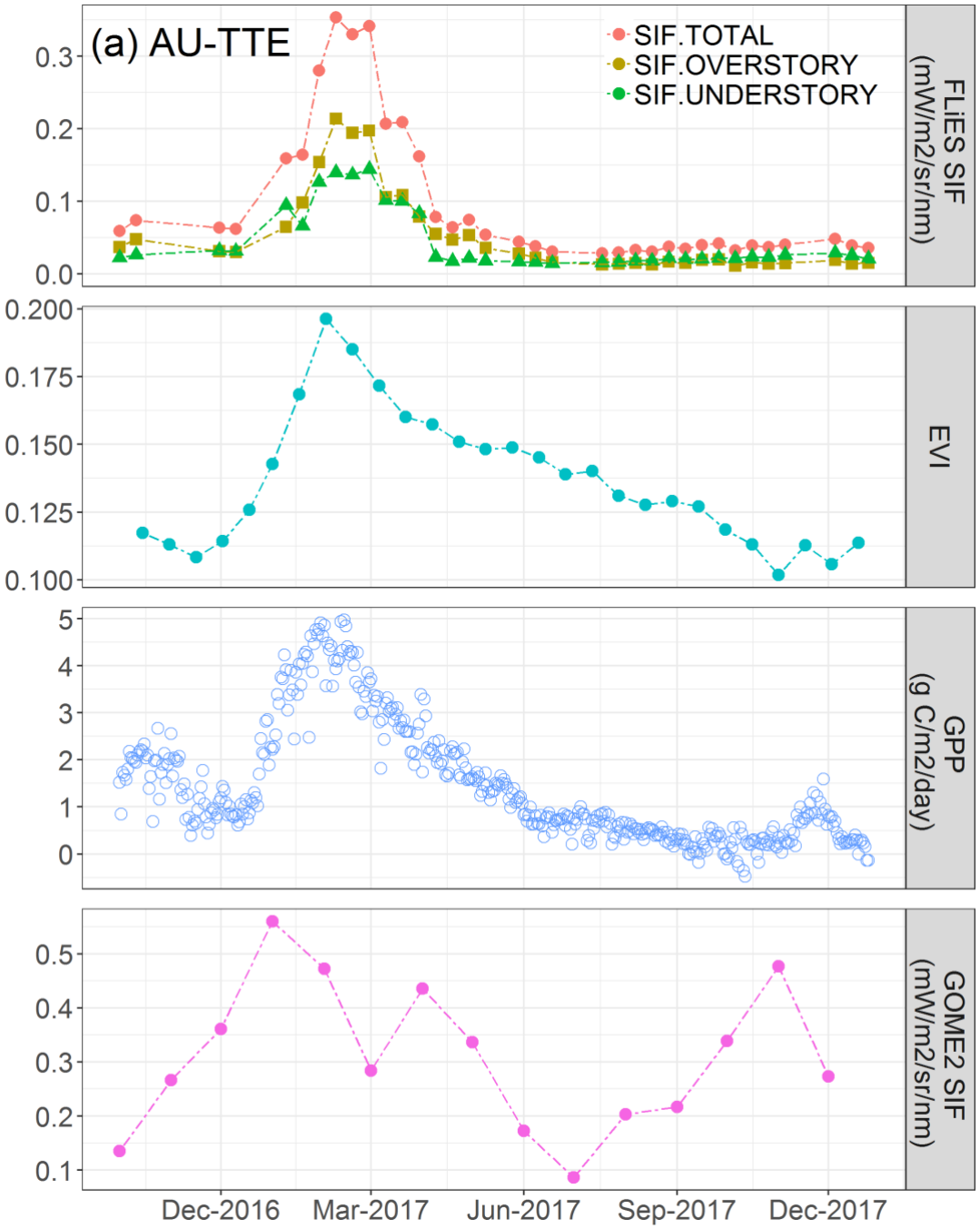
(a) AU-TTE
SIF.TOTAL
SIF.OVERSTORY
SIF.UNDERSTORY
FLiES SIF (mW/m2/sr/nm)
EVI
GPP (g C/m2/day)
GOME2 SIF (mW/m2/sr/nm)
0.0
0.1
0.2
0.3
0.100
0.125
0.150
0.175
0.200
0
1
2
3
4
5
0.1
0.2
0.3
0.4
0.5
Dec-2016
Mar-2017
Jun-2017
Sep-2017
Dec-2017

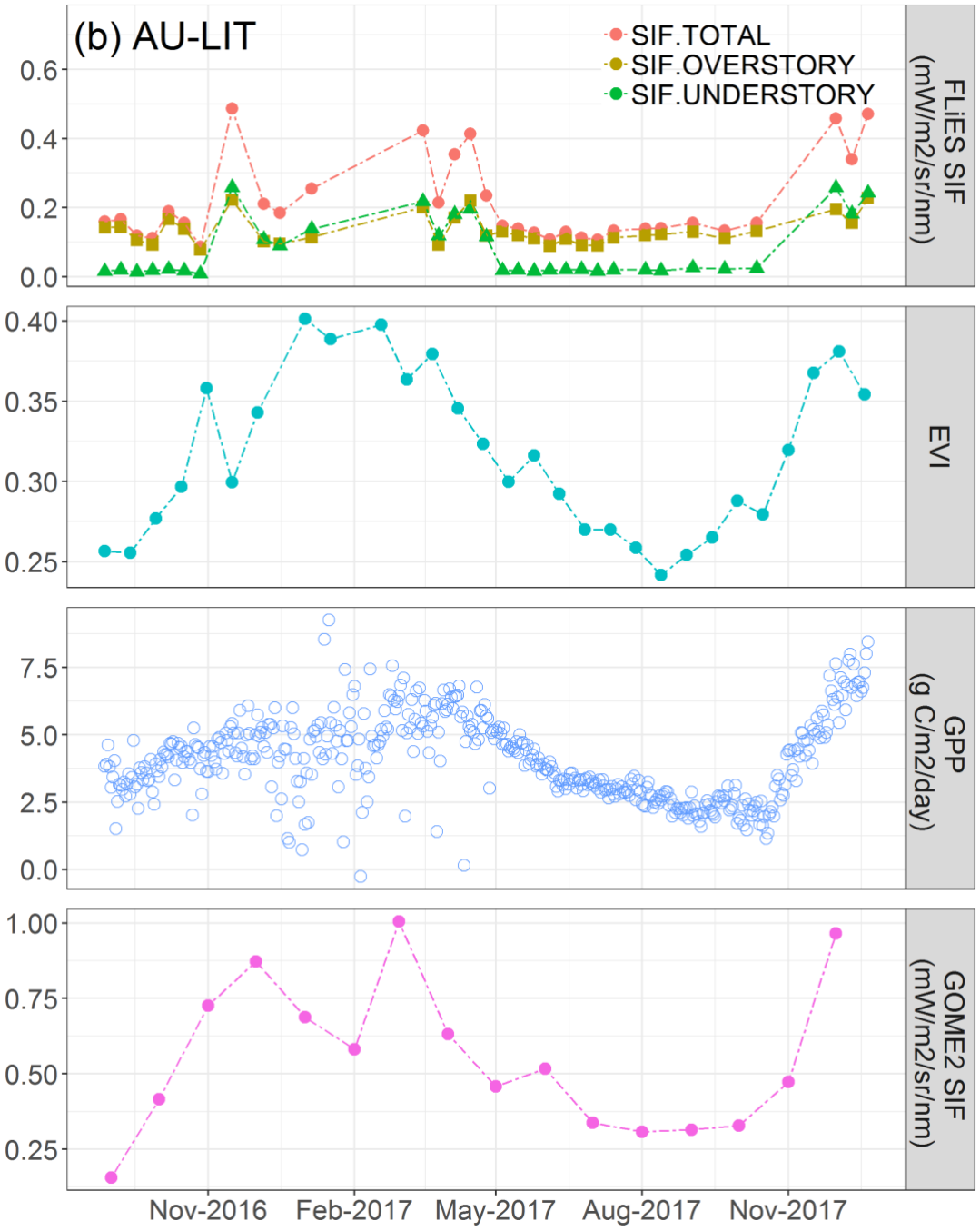
(b) AU-LIT
SIF.TOTAL
SIF.OVERSTORY
SIF.UNDERSTORY
FLiES SIF (mW/m2/sr/nm)
EVI
GPP (g C/m2/day)
GOME2 SIF (mW/m2/sr/nm)
0.6
0.4
0.2
0.0
0.40
0.35
0.30
0.25
7.5
5.0
2.5
0.0
1.00
0.75
0.50
0.25
Nov-2016
Feb-2017
May-2017
Aug-2017
Nov-2017

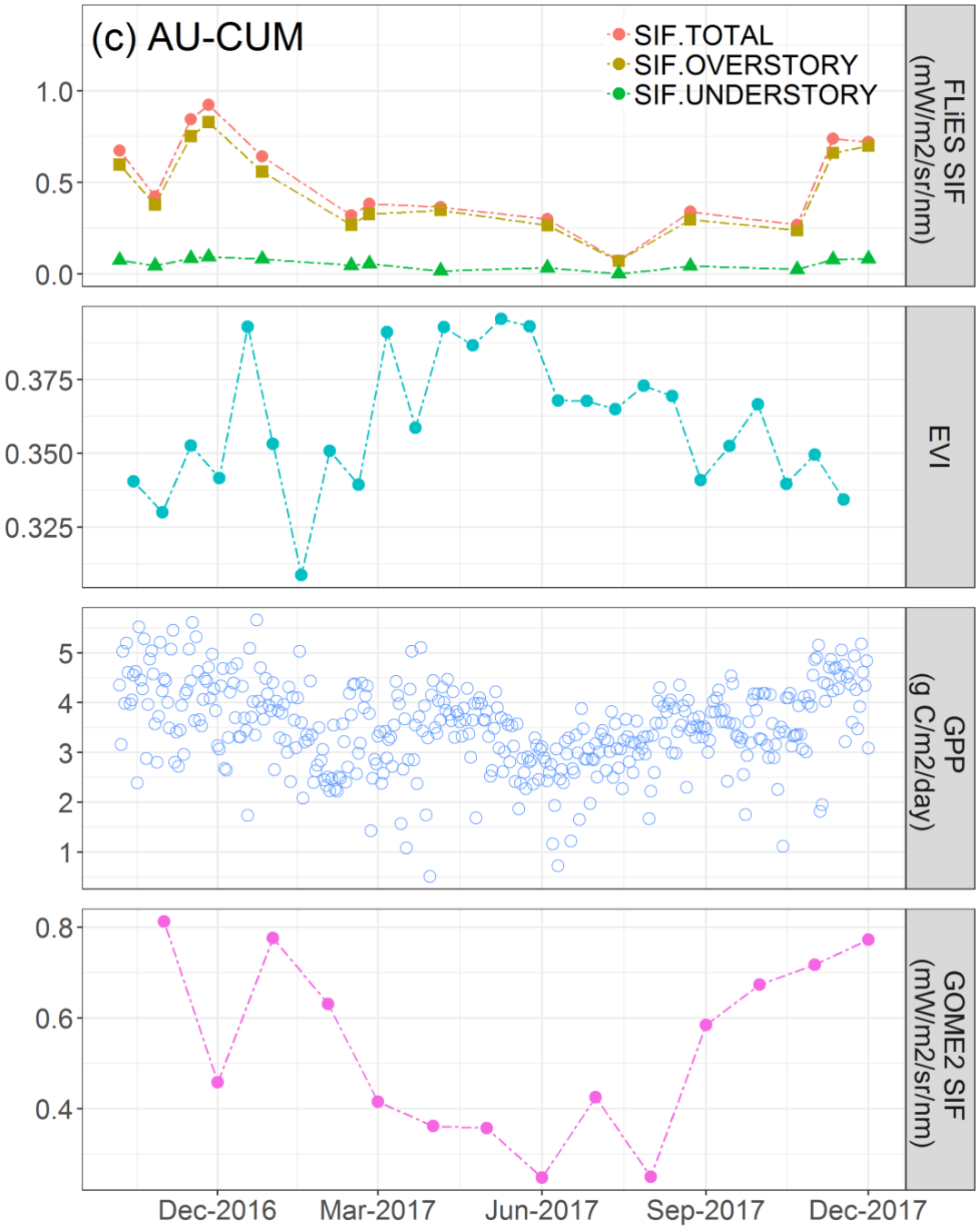


Figure 3.3. Time series of FLiES model simulated SIF, MODIS EVI, eddy covariance GPP and GOME2 SIF from 2016 to 2017 for (a) AU-TTE, (b) AU-LIT and (c) AU-CUM.

### 3.4.2. The relationship between $GPP_{EC}$ and overstory $SIF_{FLiES}$, understory $SIF_{FLiES}$

Figure 3.4 presents the correlation between $GPP_{EC}$ and model simulated total $SIF_{FLiES}$, overstory $SIF_{FLiES}$, understory $SIF_{FLiES}$ for AU-TTE, AU-LIT and AU-CUM. Overstory and understory $SIF_{FLiES}$ are highly correlated with $GPP_{EC}$ in AU-TTE (Figure 3.4 (a), $R_2$

= 0.78 and 0.75, respectively). This indicates that both these two layers are the primary source, contributing to GPP.

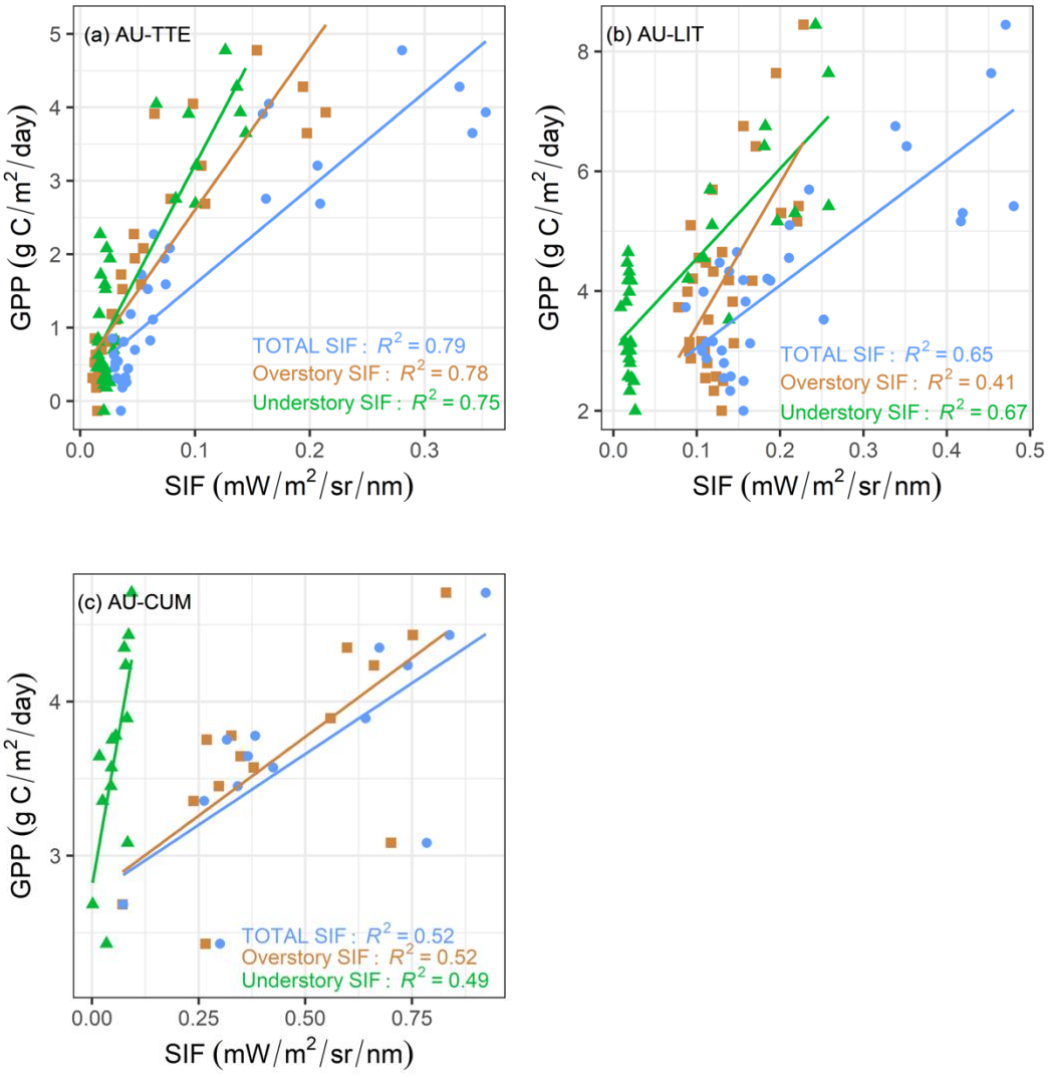


Figure 3.4. Correlation between GPP and total SIF$_{FLiES}$, overstory SIF$_{FLiES}$, understory SIF$_{FLiES}$ for (a) AU-TTE, (b) AU-LIT and (c) AU-CUM. The blue, brown and green points represent the total SIF, overstory SIF and understory SIF, respectively. The line is the linear regression line. All p-values are less than 0.0001.

In AU-LIT, understory SIF$_{FLiES}$ was more highly correlated with GPP$_{EC}$ than was overstory SIF$_{FLiES}$ (Figure 3.4 (b), $R_2$ = 0.67 and 0.41, respectively). Although understory SIF$_{FLiES}$ showed a non-significant pattern with GPP$_{EC}$ in the dry season, it still mainly contributed to GPP. The less variation of overstory SIF$_{FLiES}$ led to the weak correlation with GPP$_{EC}$.

In AU-CUM, overstory $SIF_{FLiES}$ and understory $SIF_{FLiES}$ showed a similar coefficient of determination (Figure 3.4 (c), $R_2$ = 0.52 and 0.49, respectively). Even though the understory $SIF_{FLiES}$ was rather lower than overstory $SIF_{FLiES}$; it was still positively correlated with $GPP_{EC}$.

Among these three sites, total $SIF_{FLiES}$, overstory $SIF_{FLiES}$ and understory $SIF_{FLiES}$ of AU-TTE were more correlated with $GPP_{EC}$ than in the other sites. AU-LIT's overstory $SIF_{FLiES}$ was correlated the weakest with $GPP_{EC}$, and AU-CUM's understory $SIF_{FLiES}$ was correlated the weakest with $GPP_{EC}$.

### 3.4.3. Predicted overstory GPP and understory GPP

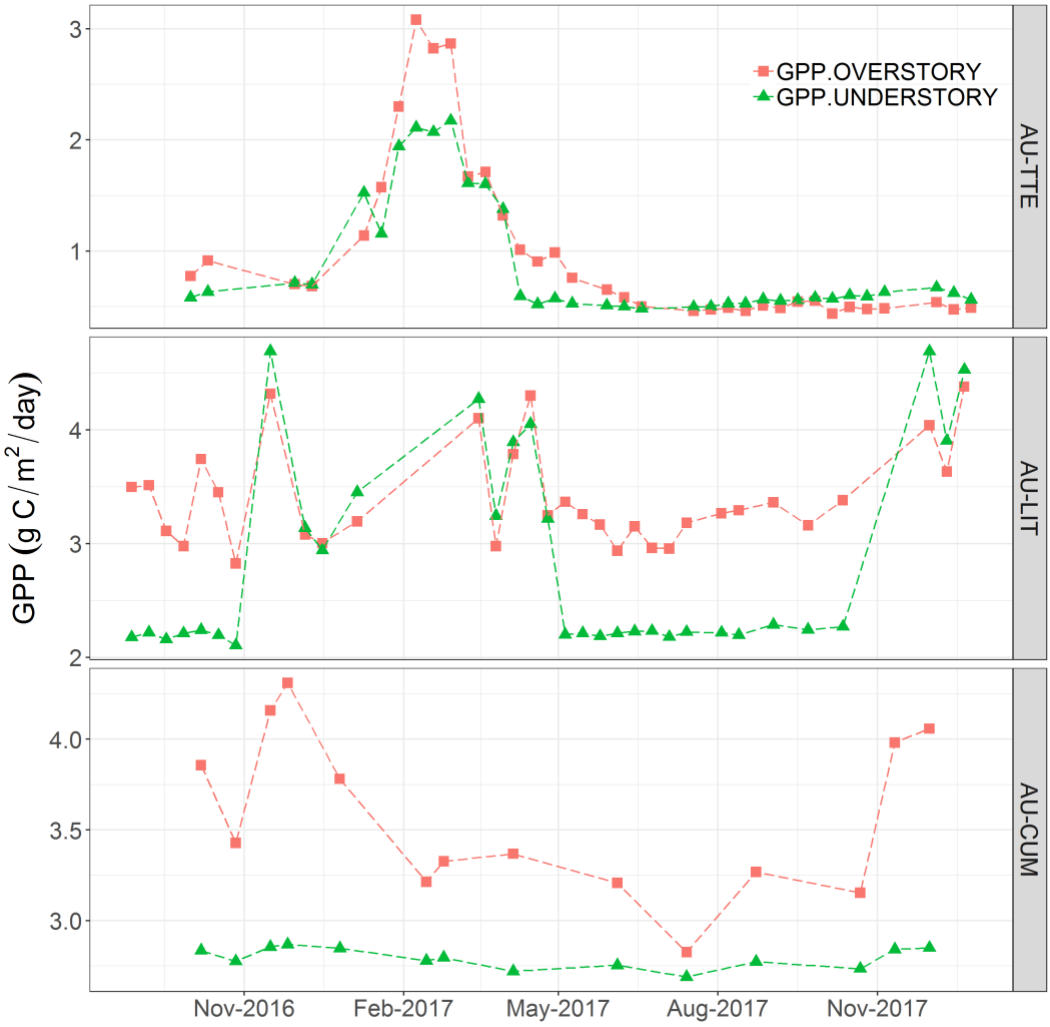


Figure 3.5. Prediction of GPP for AU-TTE, AU-LIT and AU-CUM from 2016 to 2017.

Based on the linear relationship between $GPP_{EC}$ and total $SIF_{FLiES}$, we predicted overstory GPP and understory GPP based on overstory $SIF_{FLiES}$ and understory $SIF_{FLiES}$ for AU-

TTE, AU-LIT and AU-CUM (Figure 3.5). Between January 2017 and March 2017, the overstory GPP was higher than understory GPP in AU-TTE. Apart from this period, the understory GPP was similar to the overstory GPP. For AU-LIT, overstory GPP fluctuated from 3 to 4.1 g C/m2/day over the duration of this study. However, the understory GPP was almost the same as overstory GPP in the wet season (December 2016 to February 2017). Hence, overstory GPP was the main contributor in the dry season. The understory vegetation contributed approximately 45% to total GPP and accounted for 51% of total GPP in 2017. It is consistent with Whitley's study (Whitley et al. 2011). In AU-CUM, the understory GPP was stable at around 2.75 g C/m2/day during the study period. Total GPP mainly consisted of overstory GPP. Furthermore, the RMSE of total GPP and $GPP_{EC}$ was checked for each site. The RMSE is 0.65 g C/m2/day for AU-TTE, 0.91 g C/m2/day for AU-LIT, 0.41 g C/m2/day for AU-CUM.

## 3.5. Discussion

### 3.5.1. Vegetation structure and PAR effect SIF on overstory and understory layer for different vegetation types.

We examined the meteorology and canopy structure factors that would have an effect on SIF emissions in the different layers. Firstly, we found that SIF was strongly correlated with PAR in both overstory and understory layers ($R^2$ = 0.89 and 0.51, respectively. P-value < 0.0001) in acacia woodlands (AU-TTE). Because the tree distribution is sparse and canopy cover is rather low (mean canopy cover is 14%) in this area, sunlight can reach the understory layer with minimal obstruction from objects in the overstory layers. This is the main reason that PAR in the understory layer is larger than in the overstory layer (Figure 3.6 (a)). The correlation between PAR and SIF emission in AU-LIT was different from AU-TTE. SIF from the understory layer is positively correlated with GPP ($R^2$ = 0.88, p-value < 0.0001), however, overstory SIF showed no significant pattern with GPP ($R^2$ = 0.04, p-value = 0.0008) (Figure 3.6 (b)). Overstory SIF was less variable over our study period (Figure 3.6 (b)), and overstory LAI was stable and constant (Whitley et al. 2011). It indicated that PAR seasonal changes affected overstory SIF less than understory SIF in the tropical savanna. Compared to AU-TTE and AU-LIT, understory SIF in AU-CUM showed a weak relationship with PAR ($R^2$ = 0.37, p-value < 0.0001). Because the canopy cover is high (mean canopy cover is 52%) a less direct beam, which

is the main trigger for SIF emission, can reach the understory layer. This is consistent with measurements made by (Kato et al. 2016).

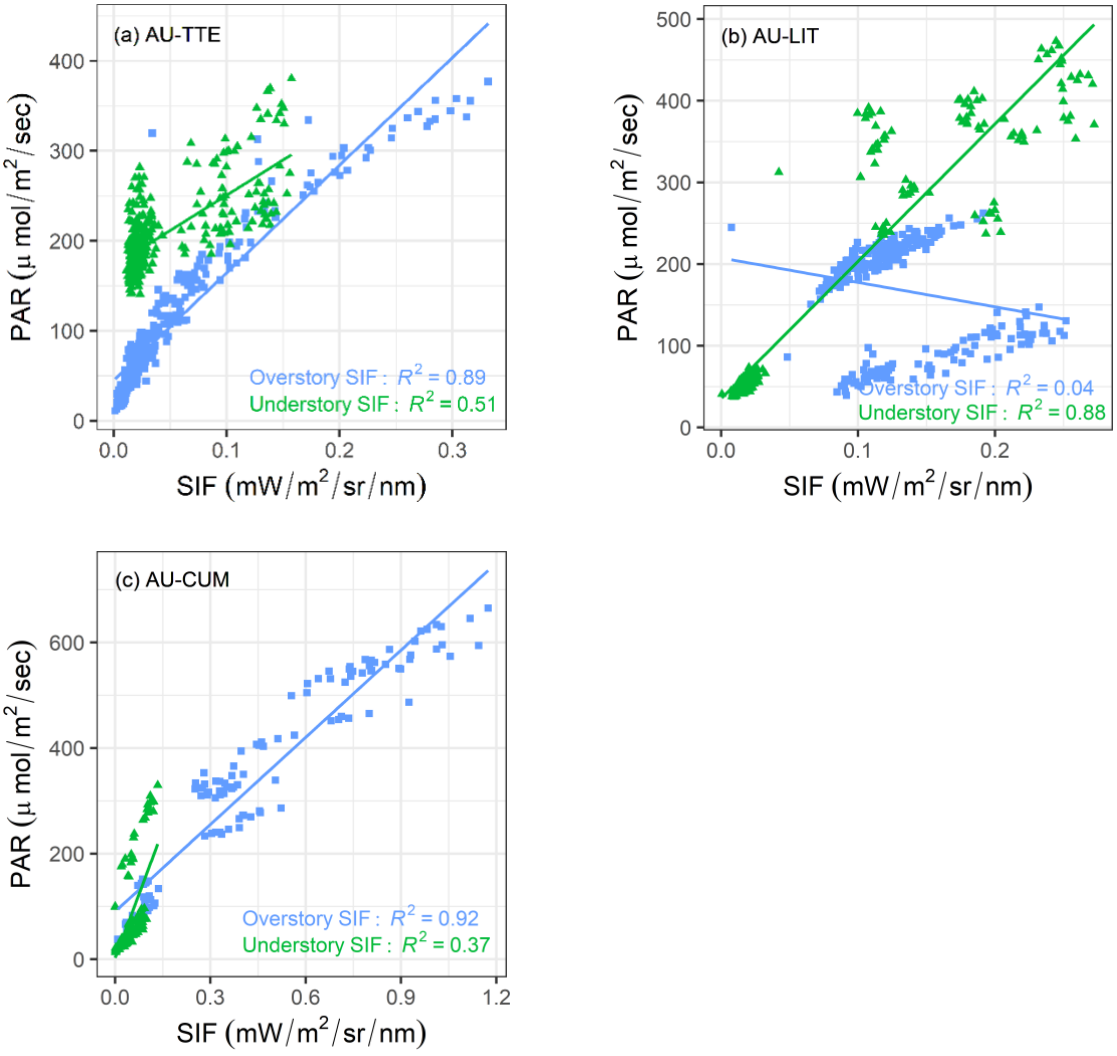


Figure 3.6. Correlation between SIF and PAR in overstory and understory layers for (a) AU-TTE, (b) AU-LIT and (c) AU-CUM

Secondly, we checked the relationship between SIF and canopy cover for these three sites (Figure 3.7). The correlation for AU-TTE and AU-LIT showed the high coefficient of determination of SIF and canopy cover ($R_2$ = 0.67 and 0.48, respectively, p-value < 0.0001). This implies the contribution from understory SIF could not be ignored because of the lower canopy cover. The relationship between SIF and canopy cover is lower in AU-CUM ($R_2$ = 0.26, p-value < 0.0001). The reason is that the dense canopy cover reduces the light reaching the understory layer and the canopy cover changes less in an

evergreen forest. In summary, SIF can be detected more in the smaller overstory canopy cover area.

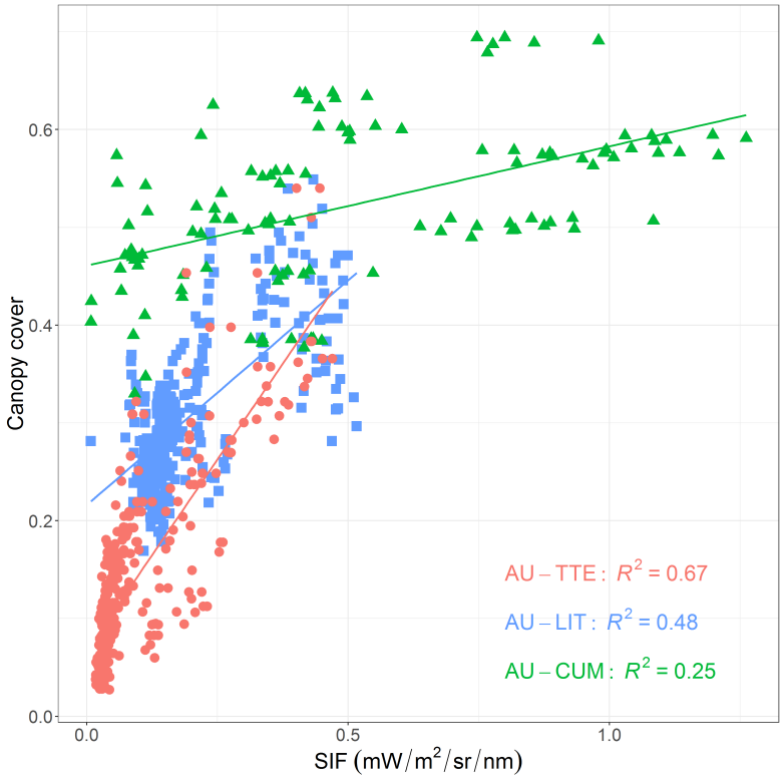


Figure 3.7. Correlation between SIF and canopy cover for AU-TTE, AU-LIT and AU-CUM. The line means a linear regression line. All p-value is less than 0.0001.

Table 3.3. The PAR, SIF and Canopy cover for overstory and understory in AU-TTE, AU-LIT and AU-CUM.

| | | PAR | | SIF | | Canopy cover |
|---|---|---|---|---|---|---|
| | | μmol/m2/sec | % | mW/m2/sr/nm | % | % |
| AU-TTE | overstory | 108.06±85.26 | 34.31% | 0.052±0.057 | 54.9% | - |
| | understory | 206.88±45.54 | 65.69% | 0.044±0.041 | 45.1% | - |
| | total | 314.95±107.85 | - | 0.096±0.097 | - | 14.27±9.82% |
| AU-LIT | overstory | 167.66±62.91 | 51.22% | 0.133±0.418 | 63.18% | - |
| | understory | 159.63±147.39 | 48.78% | 0.077±0.085 | 36.82% | - |
| | total | 327.29±97.18 | - | 0.210±0.120 | - | 30.71±8.34% |
| AU-CUM | overstory | 337.94±187.54 | 78.95% | 0.449±0.229 | 89.2% | - |
| | understory | 90.05±82.22 | 21.05% | 0.054±0.028 | 10.8% | - |
| | total | 427.99±160.57 | - | 0.504±0.256 | - | 51.55±8.85% |

Based on our results, Figure 3.8 shows a generalised pattern of relationship between SIF and PAR, canopy cover for overstory and understory layers. For the overstory layer, the pattern between PAR and SIF is similar to that of the canopy cover. They both increase under the dense canopy cover area. This suggests the higher canopy cover leads to more leaf emitted SIF and the canopy can receive more PAR. For understory layers, the situation is different from overstory layers. With the increase of canopy cover, less PAR reaches the understory and it leads to the lower SIF emission from grass or shrubs. In addition, the understory PAR accounted for two-thirds of total incoming radiation in AU-TTE, but the understory SIF stood for nearly half of total SIF (Table 3.3). The reason may relate to the fluorescence efficiency of the overstory layer being higher than the understory.

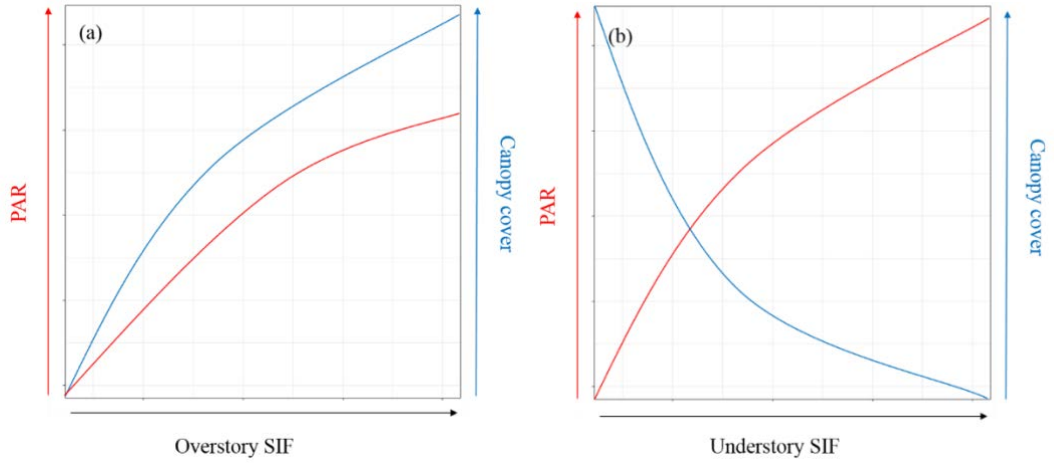


Figure 3.8. Generalised pattern from our results: (a) the relationship between overstory SIF and PAR, canopy cover; (b) the relationship between understory SIF and PAR, canopy cover. The arrows indicate values from low to high.

### 3.5.2. Uncertainties of SIF simulation in overstory and understory layers

We used a 3D model to simulate SIF emission from overstory and understory for shrubland, savanna forest and evergreen forest. However, there are uncertainties in partitioning the SIF into two layers.

The radiative transfer model concerns the radiation distribution, but it cannot simulate ecological flux exchange. SIF may be related to many factors, including temperature, soil water content and environmental stress (Baker 2008). Hence, simulating SIF in overstory and understory layers should concern only the local ecological environment. In savanna,

precipitation and radiation influences a plant's productivity (Kanniah 2010), hence, the cloud cover and diffuse radiation may affect the understory SIF emission. We note that retrieving biochemical parameters relied on the satellite observations, so that we cannot simulate SIF in cloudy days directly. With continuing precipitation, the grass would grow rapidly and its structure would change as well, hence, if we want to know more about the understory layer change, field observations should also be employed.

Another issue is that the fluorescence quantum efficiency for photosystem I and II (fqeI, fqeII) was set as the default value (fqeI = 0.002, fqeII = 0.01) for AU-TTE, AU-LIT and AU-CUM. The fqe varies among different vegetation species (Porcar-Castell et al. 2014), because each type of plant has its own unique ability to use light efficiently. Even though PAR adjustment was implemented in the FLiES model, retrieving fqeI and fqeII is still needed for precise modelling.

In the understory layer, vegetation included both shrub and grass. Photons have complex interactions with overstory layer. Because our method relied on satellite observations, we treated the vegetation as homogenous over one pixel of observation. For example, the understory layer contains many species, including Psydrax latifolia and Thyridole psis michelliana (Eamus et al. 2013), in AU-TTE, hence researchers should distinguish different vegetation species in future study.

## 3.6. Conclusion

In this study, the FLiES model coupled with a newly developed SIF module was used to partition the SIF signal into overstory and understory layers at an interannual time scale. LiDAR data was used to build a three-dimensional model of complex vegetation structure for open shrubland, tropical savanna and evergreen forest. We retrieved biochemical data from Sentinel-2 surface reflectance data using the GPR method. Results presented different seasonal patterns of SIF distribution in AU-TTE, AU-LIT and AU-CUM. The simulated SIF model showed a similar seasonal pattern with $GPP_{EC}$ and GOME-2 SIF. In open shrubland (AU-TTE), overstory and understory SIF showed a strong relationship with PAR and GPP. For tropical savanna (AU-LIT), overstory SIF showed less variation, but understory SIF accounted for 50% of the total SIF in the wet season. In the evergreen forest, the contribution of understory SIF was less than overstory SIF, and it showed a weak relationship with canopy cover. Hence, the incoming radiation is not the primary reason leading to less SIF emission. In shrubland and tropical savanna, SIF was more

sensitive to canopy cover. In the future, we would discuss further to what extent understory SIF is affected by other ecological factors.

# Chapter 4. OCO-2 sun-induced chlorophyll fluorescence normalised by a three dimensional radiative transfer model is better correlated with vegetation productivity

## Abstract

Sun-induced chlorophyll fluorescence (SIF) is one of the most effective indicators that can be used to show vegetation photosynthetic activities. Variable scale measurements from leaf level to space have been implemented to find strong correlations between SIF and gross primary production (GPP). SIF yield and LUE (light use efficiency) can exist in positive or negative relationships under different light conditions (limiting or saturating) and dependent on sunlit and sun shaded leaves. In addition, variations of sun position and viewing angle bring uncertainties to the relationships of GPP and SIF, SIF yield and APAR (Absorbed Photosynthetically Active Radiation), and SIF yield and LUE. With the help of the OCO-2 (Orbiting Carbon Observatory-2) satellite sensor, which provides special geometric measurement modes (nadir, glint and target mode), we collected and analysed SIF emissions at nadir, hot spot and dark spot directions over three flux tower sites (US-PFa, US-WCr and US-NR1). We found that SIF in the hot spot direction was better correlated with GPP ($R_2$ = 0.95, 0.95 and 0.88 for US-PFa, US-WCr and US-NR1, respectively) than at other geometrical directions. Furthermore, we implemented a three-dimensional radiative transfer model (FLiES) coupled with solar position, viewing angle and LiDAR-based vegetation structure retrievals to simulate the relative photosynthetic active radiation for three viewing conditions. Our results were used to normalise the far-red OCO-2 SIF and this resulted in SIF yields better correlated with APAR and LUE in the hot spot and dark spot directions, compared with the original SIF observations. The coefficient of determination of SIF yield and LUE was improved from 0.39 to 0.48 at all three sites normalized by the model. Lastly, statistical analysis suggested that PAR (Photosynthetically Active Radiation) was the most critical factor (34.06%) explaining the SIF observations from the hot spot observations, while air temperature was the most relative importance factor (42.51%) for SIF variations in dark spot geometries. Our findings will help lead to a better understanding of view angle influences on sunlit and sun shade SIF retrievals.

## 4.1. Introduction

Sun-induced chlorophyll fluorescence (SIF) is a weak signal, but it can indicate a plant's photosynthetic efficiency (Baker 2008). It mainly exists from 650 to 850 nm and has two peaks at 680 and 740 nm, respectively. The fluorescence at 685 nm, normally regarded as red SIF, only contains photosystem II (PSII) information, while the 740 nm

fluorescence, regarded as far-red SIF, contains both photosystems I and II (PSII) information (Porcar-Castell et al. 2014). Because of the low absorption of far-red SIF (Yang & Van Der Tol 2018), it is common to use as a proxy to study the relationship between SIF and abilities of vegetation's photosynthesis. The SIF signal is similar to the reflectance, it is also influenced by the viewing angles (bidirectional reflectance distribution function effects, BRDF) (Liu et al. 2016). Different view positions and sun positions might lead to variable results of SIF.

Over the past ten years, many satellites were launched for monitoring SIF at different spatial and temporal resolutions. GOME-2 (Global Ozone Monitoring Experiment-2) started its observation from 2007 and provided a new approach to detect how vegetation's photosynthetic activities respond to climate change (Guanter et al. 2012; Joiner et al. 2013). The level 3 data of GOME-2 offers monthly SIF data, but the coarse spatial resolution (40 * 40 km) and the degradation of sensors brings uncertainties and difficulties for the long-term time series analysis (Zhang, Joiner, Gentine, et al. 2018). Compared to GOME-2, OCO-2 (Orbiting Carbon Observatory-2) provides fine spatial resolution (1.3 km * 2.25 km), however, the disperse soundings, discontinuous spatial coverage and a 16 day revisit dataset, creates the need to interpolate for large scale studies (Frankenberg et al. 2014; Sun et al. 2017). Some studies used a machine learning method to create OCO-2 SIF products, GOSIF, CSIF and $\overline{SIF}_{OCO2\_005}$ at 0.05° spatial resolution (Li & Xiao 2019; Yu et al. 2019; Zhang, Joiner, Alemohammad, et al. 2018). In addition, TROPOMI (TROPOspheric Monitoring Instrument) is the newest launched satellite (data available from March 2018). It provides medium spatial resolution (7 km * 3.5 km) and a high frequency revisit (almost daily) dataset (Guanter et al. 2015; Köhler, Frankenberg, et al. 2018). In time, TROPOMI will be the most popular SIF satellite for analysis of vegetation photosynthetic activities.

As contrast to the other satellites, OCO-2 has three different measurement modes: Nadir, Glint and Target mode (Frankenberg et al. 2014). The Nadir mode is the sensor which collects the data at the nadir view directions. Glint mode observations are made when the solar zenith angle at the apparent glint spot is less than 75 degrees. OCO-2 has been validated in many places, globally. When the satellite passes by these places, OCO-2 activates a target mode and collect thousands of observations. At this time, the solar zenith angle and solar azimuth angle are assumed to be fixed, hence, OCO-2 contributes to analysis of how variations of viewing angle effects the SIF value.

Guanter found that GOME-2 SIF was significantly correlated with eddy covariance GPP (gross primary production) for cropland (Guanter et al. 2014a). GOME-2 SIF also was used to detect the plants responding to heat events and drought (Song et al. 2018a; Sun et al. 2015b). Li analysed the relationship between GPP and OCO-2 SIF for 64 flux sites globally and found there was an existing universal relationship of GPP and SIF for a wide variety of vegetation (Li et al. 2018). Additionally, SIF devices (FluoSpec, FluoSpec2 and SIF-sys) have been set up to monitor diurnal and seasonal SIF variations (Miao et al. 2018; Wieneke et al. 2018b; Yang, Ryu, et al. 2018). Researchers have found that the relationship of SIF:GPP in finer temporal resolution (half-hourly) was much weaker than at the seasonal scale, and SIF was primarily driven by APAR (absorbed photosynthetically active radiation) (Yang, Ryu, et al. 2018; Zhang et al. 2016). In addition, a significantly positive correlation between GPP and SIF under a clear sky and cloudy sky was found at the seasonal scale for deciduous broadleaf forests (Yang et al. 2015b).

In order to remove the APAR effects on SIF and GPP, and discover the exact relationship between SIF and GPP, researchers have partitioned SIF yield and LUE (light use efficiency) to GPP (Damm et al. 2015a).

$$SIF_{yield} = \frac{SIF}{APAR} \tag{4-1}$$

$$LUE = \frac{GPP}{APAR} \tag{4-2}$$

Equations 4-1 and 4-2 explains that SIF and GPP both contain the APAR. SIF yield can be treated as the emitted SIF per photon absorbed (light use efficiency for fluorescence). LUE can be treated as how much light is used for photosynthesis. The previous study confirmed that the SIF is more correlated with APAR than photosynthesis (Yang, Ryu, et al. 2018), and some researchers have found that the pattern of LUE and SIF was negative across the diurnal and seasonal scale for soybean (Miao et al. 2018), which was contrary to Yang and Verma's study in a deciduous temporal forest and C4 grass (Verma et al. 2017; Yang et al. 2015b). It might due to different vegetation types and different growing seasons. Miao suggested that the relationship of SIF yield and LUE varied with the light conditions. While vegetation is under saturating light, the SIF yield is positive with LUE, and negative when the light is limited (Van der Tol et al. 2014). However, this pattern on sunlit (light easily saturating) and sun shade leaves (light limiting) have not been

confirmed at the site scale. Sunlit and sun shade leaves might exhibit different patterns of SIF:GPP and SIF yield: LUE. When a hyperspectral camera was involved in SIF study, it showed the sunlit SIF is two-fold that of sun shade SIF (Pinto et al. 2016). It implied that the light conditions of sunlit leaf and sun shade leaf might be different.

The SIF signal is similar to reflectance, as it is affected by the direction of the view. Some researchers have already used models to demonstrate when SIF reached a peak at the hot spot direction (Van der Tol et al. 2014; Zhao et al. 2016). The field measurement furthermore confirmed SIF at $O_2$-A band has clear BRDF affection (Liu et al. 2016). Satellite observations also confirmed this issue: normalised GOME-2 SIF at hot spot direction was strongly correlated with sunlit GPP (He et al. 2017). However, the coarse spatial resolution of GOME-2 data makes it challenging to validate at the site scale. In addition, Zhang indicated that OCO-2 data is prone to being affected by viewing angles.

In this study, we aimed to check the BRDF effects on the relationships of SIF:GPP and SIF yield:LUE, and discuss essential factors that would have an impact on SIF from the sunlit and sun shade crown areas. Our objectives were to (i) identify SIF value variance with view zenith angle and view azimuth angle for mixed forest, deciduous broadleaf forest and evergreen needle forest at the site level; (ii) examine the relationship between SIF and GPP for various view observations, and investigate the utility of a normalised SIF at the hotspot and dark spot directions to represent sunlit and sun shade crown area, respectively; (iii) investigate the relative importance of environmental factor contributions for the nadir, hot spot and dark spot observations. This research will be useful for understanding how sunlit and sun shade SIF values vary and their sensitivity to environmental factors.

## 4.2. Study area and Data

### 4.2.1. Study area

We selected three sites for this study, Park falls, Willow Creek and Niwot ridge forests. Flux towers are implemented to enable measuring in these sites. Park falls (US-PFa) is located in the north of the USA (45°56' N, 90°16' W). The elevation of US-PFa is 470 m above sea level. The mean annual temperature and precipitation are 4.33 °C and 823 mm, respectively. This site is surrounded by forest and wetlands. The forest is mixed temperate forest and includes northern hard-woods, red pine and forested wetlands (Li et al. 2018).

The second flux site, Willow Creek (US-WCr, 45°48' N, 90°04' W), is near the US-PFa (21 km to the southeast). The elevation is 520 m above sea level. The mean annual temperature and precipitation are 4.02 °C and 787 mm, respectively. The land cover of this site is a deciduous broadleaf forest. The vegetation of US-WCr includes sugar maple, basswood and green ash (Cook et al. 2004).

Niwot ridge forest (US-NR1) is located in the Rocky Mountains of Colorado, USA (40°01' N, 105°32' W). The elevation is 3050 m above sea level. The mean annual temperature and precipitation are 1.5 °C and 800 mm, respectively. The primary land cover is evergreen needle forest. The forest includes subalpine fir, lodgepole pine and Englemann spruce (Burns et al. 2016).

### 4.2.2. OCO-2 SIF

The Orbiting Carbon Observatory 2 (OCO-2) is used to study carbon dioxide distribution in the atmosphere from July 2014, and it also retrieves fluorescence from the $O_2$-A band (Frankenberg et al. 2015). We obtained the SIF data from OCO-2 SIF product (OCO2_L2_Lite_SIF_V8r, 8100r). OCO-2 SIF's temporal resolution is 16 days, and its spatial resolution is 1.3 km * 2.25 km. Each measurement, covers eight footprints, and the local passing time is 13:36.

Although OCO-2 provided two bands of SIF (757 and 771 nm), we chose 757 nm for this study due to its better correlation with GPP (Li, Xiao & He 2018a). We collected instantaneous SIF retrievals at 757 nm for the area of 10 km * 10 km around each flux tower site from September 2014 to November 2018. We removed OCO-2 SIF retrievals in glint mode because it has been reported that it is of low quality and underestimates SIF (Sun et al. 2017). Nadir and target mode of SIF soundings were used in this study. OCO-2 data is filtered by IGBP (International Geosphere-Biosphere Programme) index similarly as the vegetation type of each flux site. We did not aggregate instantaneous SIF into daily SIF because we aim to check immediately the SIF response to photosynthesis.

### 4.2.3. MODIS data

We used MODIS (Moderate Resolution Imaging Spectroradiometer) fPAR (fraction of Photosynthesis Active Radiation) for normalising APAR effects on SIF. fPAR is a factor that can present how much PAR was absorbed by vegetation for photosynthesis ($APAR = PAR \times fPAR$) (Myneni, Knyazikhin & Park 2016). MODIS fPAR is provided by

MOD15A2H (version 6) at the spatial resolution of 500 m from 2014 to 2018. We filtered raw data by the quality control method, which is recommended in their official documentation and extract the fPAR based on each flux site coordinates. Because the temporal resolution of MOD15A2H mismatches with OCO-2, we selected the closest date of fPAR to OCO-2 observations when calculating APAR.

### 4.2.4. LiDAR data

Light Detection And Ranging (LiDAR) data can calculate the distance between the sensor and measured objects by measuring the time a pulse of transmitted energy takes to return to the LiDAR sensor (Dubayah & Drake 2000). The LiDAR data of US-PFa and US-WCr are provided by GLiht (https://gliht.gsfc.nasa.gov/), and they were both surveyed in June 2012. The LiDAR data of US-NR1 is provided by NEON (https://data.neonscience.org), and it was surveyed in September 2017.

We implemented a Canopy Height Model (CHM) (Simard et al. 2011) to separate the canopy layer and ground layer and apply the crown detection method to identify each crown's position, height and area. This information would be used in building a three dimensional canopy structure for the model simulation.

### 4.2.5. Eddy covariance data

Half hourly eddy covariance data of US-PFa, US-WCr and US-NR1 are provided by Ameriflux (https://ameriflux.lbl.gov/). PAR (Photosynthesis Active Radiation), VPD (Vapour Pressure Deficit), NEE (NET Ecosystem Exchange), SWC (Soil Water Content) and Ta (air temperature) were extracted from the dataset based on the OCO-2 passing time (approximate 13:30).

Eddy covariance GPP ($GPP_{EC}$) data was calculated for checking the relationship between $GPP_{EC}$ and SIF retrievals. The R package, REddyProc (Wutzler et al. 2018), was implemented to estimate GPP with half hourly eddy covariance and meteorological data. This tool used the gap-filling and flux partitioning algorithms to partition net flux into GPP and field ecosystem respiration (Reichstein et al. 2005). $GPP_{EC}$ is similarly extracted by OCO-2 overpass time.

## 4.3. Methodology

This section briefly describes definitions of OCO-2 viewing directions and the framework of simulation for relative radiation.

### 4.3.1. Definitions of OCO-2 observation directions

We defined OCO-2 observations into three directions: nadir, hot spot and dark spot. The nadir direction contains the observations under the nadir measurement mode and the definition as:

$$VZA = 0° \tag{4-3}$$

VZA means the view zenith angle. The hot spot is defined as an observation and solar directions are a coincidence (as equation 4-4 shows). In order to retrieve enough observations for statistics, we used a larger threshold for hot spot direction,

$$\begin{cases} |SZA - VZA| < 15° \\ |SAA - VAA| < 30° \end{cases} \tag{4-4}$$

where SZA means solar zenith angle, SAA means solar azimuth angle and VAA means view azimuth angle. The dark spot is defined as VAA is in the forwarding scattering direction as:

$$\begin{cases} |SZA - VZA| < 10° \\ \big||SAA - VAA| - 180°\big| < 5° \end{cases} \tag{4-5}$$

### 4.3.2. FLiES model

FLiES (version 2.48) (Kobayashi & Iwabuchi 2008), a three dimensional radiation transfer model, was implemented to simulate the relative absorbed radiation from different solar positions and viewing angles. It based on the Monte Carlo method and ray-tracing frame. A large number of photons were uniformly distributing above the simulation scene, then the random method was used to generate each photon's direction. With a large number of repetition times, simulation results are close to reality.

In order to build a three-dimensional vegetation structure, vegetation properties, including height, position and crown area, were extracted from the LiDAR data. We simply defined the simulation as two layers: the canopy layer and understory layer.

### 4.3.3. Normalised APAR and SIF yield

We calculated the APAR for different observation directions as:

$$\begin{cases} APAR_{Nadir} = PAR \times f_{PAR} \\ APAR_{Hot\ spot} = PAR \times f_{PAR} \times relaPAR_{Hot\ spot} \\ APAR_{Dark\ spot} = PAR \times f_{PAR} \times relaPAR_{Dark\ spot} \end{cases} \quad (4\text{-}6)$$

where $APAR_{Nadir}$ , $APAR_{Hot\ spot}$ and $APAR_{Dark\ spot}$ are the APAR for nadir, hot spot and dark spot direction. We assumed $f_{PAR}$was uniformly distributed in the canopy layer. PAR was collected from each flux site and $f_{PAR}$ was collected from the MODIS dataset. $relaPAR_{Hot\ spot}$ and $relaPAR_{Dark\ spot}$ was simulated by the FLiES model. The simulation method was that I counted the PAR value in canopy layer at the giving field of view, and then I calculated the ratio between PAR at the giving direction and total PAR. Hence, the SIF yield for different observations directions can be defined as followings,

$$\begin{cases} SIF\ yield_{Nadir} = SIF_{Nadir}/APAR_{Nadir} \\ SIF\ yield_{Hot\ spot} = SIF_{Hot\ spot}/APAR_{Hot\ spot} \\ SIF\ yield_{Dark\ spot} = SIF_{Dark\ spot}/APAR_{Dark\ spot} \end{cases} \quad (4\text{-}7)$$

### 4.3.4. Structure of model simulations

Figure 4.1 showed the flow chart of our methodology. Firstly, we separated OCO-2 soundings as the nadir, hot spot and dark spot direction as our definitions (section 4.3.1). For each direction, we extracted every sounding from SZA, SAA, VZA and VAA. Their angles were coupled with the canopy structure, which processed by LiDAR data, were for FLiES model settings.

For the FLiES model setting, we set $10^8$ photons (as the model document suggests), the reflectance and transmittance for leaf, stem are set as default and leaf inclination is uniformly distributed. In our simulation area, the distribution of trees is dense and less photon reflection from the underground layer can reach the virtual sensor, and we only considered the canopy layer radiation distribution, so we set the reflectance and transmittance of the underground as default as well. To calculate the relative PAR for different directions, we used the same incident PAR and leaf density for every direction. Because the shape of the crown in these three sites is different, we set the crown shape as a cone for US-NR1 (evergreen needle forest) and ellipsoids for US-PFa and US-WCr, respectively. We can then get the relative PAR from each simulation, and retrieve SIF yield for nadir, hot spot and dark spot direction based on equation 4-7.

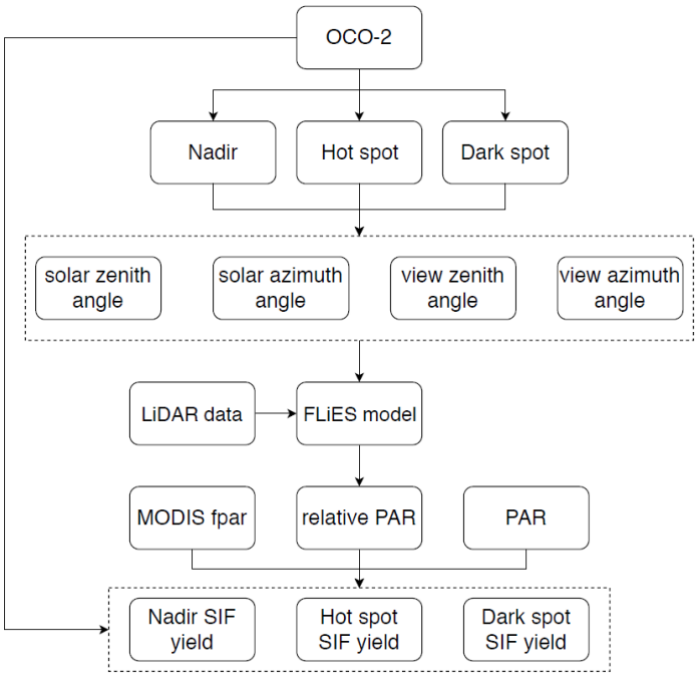


Figure 4.1. Flow chart of simulation methods.

### 4.3.5. Relative importance method

In order to evaluate environmental factors affecting each viewing direction, the partial correlation method (Chevan & Sutherland 1991) was applied in this study. We used R package relaimpo (Grömping 2006) to calculate the ranks of the environmental factors for viewing different SIFs in terms of their unique contribution to SIF retrievals. This method would be of benefit to understand each environmental factors contribution to different angles' SIF variations.

## 4.4. Results

### 4.4.1. OCO-2 SIF observations in multi-angles

Figure 4.2 shows the polar coordinate results for OCO-2 observations in a single day at the target measurement mode. In order to see the variation of SIF values clearly, the OCO-2 observation angle was resampled to one degree. The hot spot effect is obviously shown in Figure 4.2 (a)-(b). The SIF was higher when the sensor direction was coincidental to the sun angle than in other directions (SZA = 30°, SAA = 223° for Figure 4.2 (a), VZA = 32°, VAA = 225° for Figure 4.2 (b)). At the dark spot direction, SIF observations were lower than at other angles (Figure 4.2 (c), VZA = 43°, VAA = 21.5°), but were not the lowest. It suggested that SIF from the sun shade canopy area is lower than the sunlit area

and a, prior study found the SIF values measured from sunlit leaf was two-fold that of SIF from sun shade leaf (Pinto et al. 2016). But for SIF observations in 2017-04-21 (Figure 4.2 (d)), the SIF values (mean SIF = 0.22 mW/m2/sr/nm) were similar at different angles. The reason may be that the leaves were not growing as April was earlier than the growing season (Li, Xiao & He 2018a). Comparisons of the SIF values at a different time of the year (Figure 4.2 (a), (c)), SIF as a whole was higher in June 2018 than September at US-WCr, suggesting the SIF has seasonality (Guan et al. 2015).

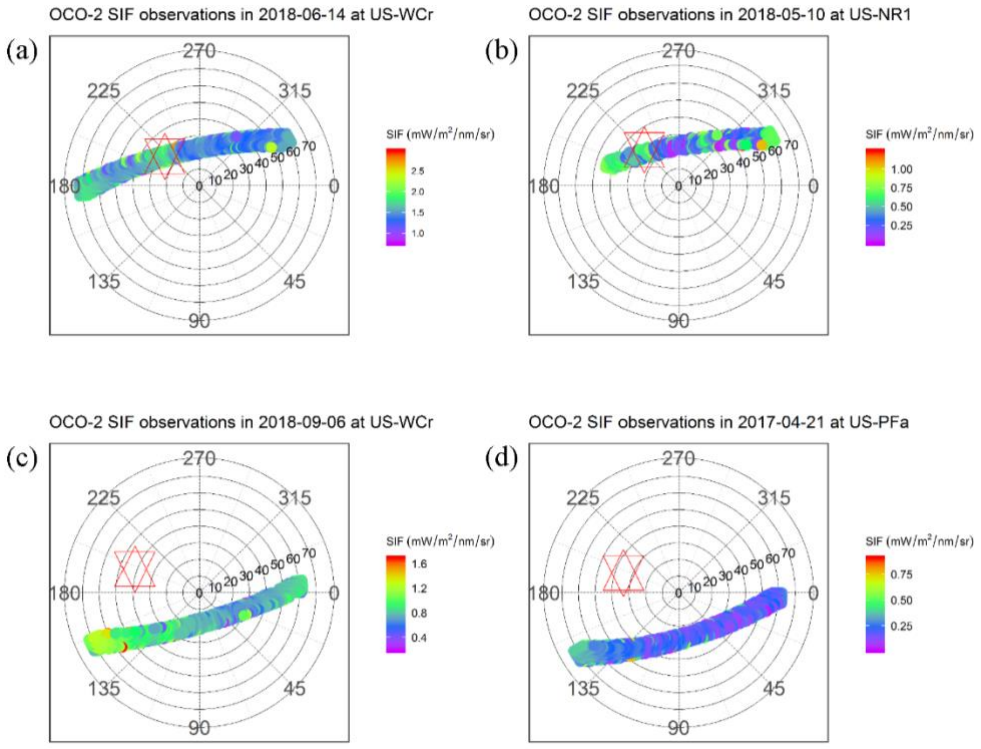


Figure 4.2. (a) – (d). Instantaneous OCO-2 SIF observations at 757 nm in different days. (a) and (b) shows the hot spot effect, (c) and (d) shows the dark spot effect. The red five-point star identifies the sun position at OCO-2 passing time. The numbers inside the circle are zenith angle. The numbers on the outermost circle represent the azimuth angle.

### 4.4.2. The relationship between GPP and OCO-2 SIF over nadir, hot spot and dark spot observations

Figure 4.3 presents the relationship between $GPP_{EC}$ and OCO-2 SIF at 757 nm in the nadir, hot spot and dark spot directions for US-PFa, US-WCr and US-NR1. All these sites exhibited the same pattern: SIF was highly correlated with $GPP_{EC}$ in the hot spot group ($R^2$ = 0.95, 0.95 and 0.88 for US-PFa, US-WCr and US-NR1, respectively). However,

the p-value of US-NR1 was more than 0.05 due to the limited SIF observations in the hot spot group. The stronger correlation implies that the SIF, observed from the sunlit crown area, can better explain the $GPP_{EC}$ changes than in other viewing directions.

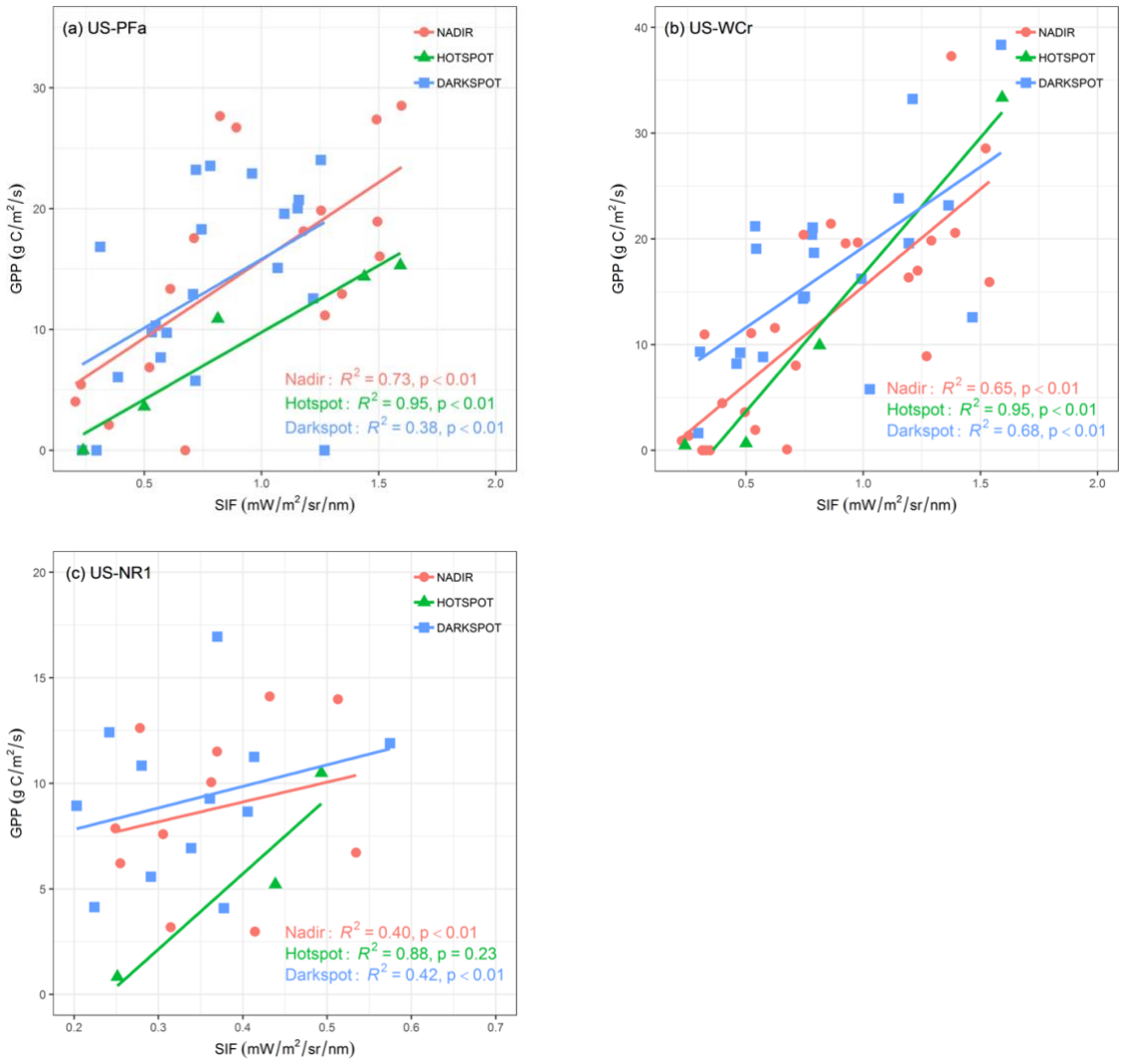


Figure 4.3. The relationship between eddy covariance GPP and OCO-2 SIF in nadir, hot spot and dark spot views for (a) US-PFa, (b) US-WCr and (c) US-NR1. Coloured lines mean the linear regression line.

In US-PFa, the coefficient of determination between SIF and $GPP_{EC}$ was 0.73 in the nadir group (Figure 4.3 (a)), which was higher than observed in the dark spot group ($R_2$ = 0.38, p-value < 0.01), but their slopes were close to each other. SIF observations in the dark spot group were mainly from the sun shade crown area. It suggested that sun shade SIF had a weak relationship with $GPP_{EC}$ in US-PFa. However, for SIF soundings in US-WCr and US-NR1 (Figure 4.3 (b), (c)), the correlation between SIF and $GPP_{EC}$ was almost same for the nadir and dark spot directions, the $R_2$ of SIF and $GPP_{EC}$ in the dark spot

direction was slightly higher than in the nadir direction (All p-value < 0.01). SIF value and $GPP_{EC}$ in US-NR1 were lower than in other sites.

### 4.4.3. The correlation between normalised APAR and SIF for nadir, hot spot, and dark spot directions

APAR mainly drives SIF, so we checked the relationship between OCO-2 SIF and normalised APAR at US-PFa, US-WCr and US-NR1 for the nadir, hot spot and dark spot directions (Figure 4.4 (a) – (c)). In the nadir direction, an obvious pattern existed for SIF and APAR. $R_2$ were 0.68, 0.64 and 0.25 for US-PFa, US-WCr and US-NR1 (all p-value < 0.01), respectively. We noted that APAR is the original APAR based on the nadir direction definition as equation 4-6 shows. In the hot spot direction, SIF was more strongly correlated with normalised APAR ($R_2$ = 0.79, 0.91 and 0.88 for US-PFa, US-WCr and US-NR1, respectively) than in other directions. The $R_2$ increased distinctly when compared with the nadir direction ($R_2$ mean increased 0.34). It suggests that the SIF from the sunlit crown area is primarily driven by APAR, which is consistent with previous studies (Yang, Ryu, et al. 2018; Yang et al. 2015b). However, the p-value of the hot spot SIF and APAR in US-NR1 is larger than 0.05, and its pattern was not significant due to limited OCO-2 observations (Figure 4.4 (c)). Compared to the hot spot direction, the explanation of APAR by SIF from the dark spot direction was weak in all three sites and was even weaker than the nadir direction. The coefficients of determination were 0.52, 0.6 and 0.11 for US-PFa, US-WCr and US-NR1, respectively. It suggested that the SIF variation from the sun shade crown area was not driven by APAR and we should consider other environmental factors that would impact SIF in the sun shade crown area (Pinto et al. 2016). It is noticed that the slope for different view directions is not consistent among the three study sites. An explanation might be that SIF has its own response speed to APAR in different varied light area conditions. In other words, SIF in the hot spot direction was more sensitive to the APAR variations than SIF observed in the nadir and dark spot directions.

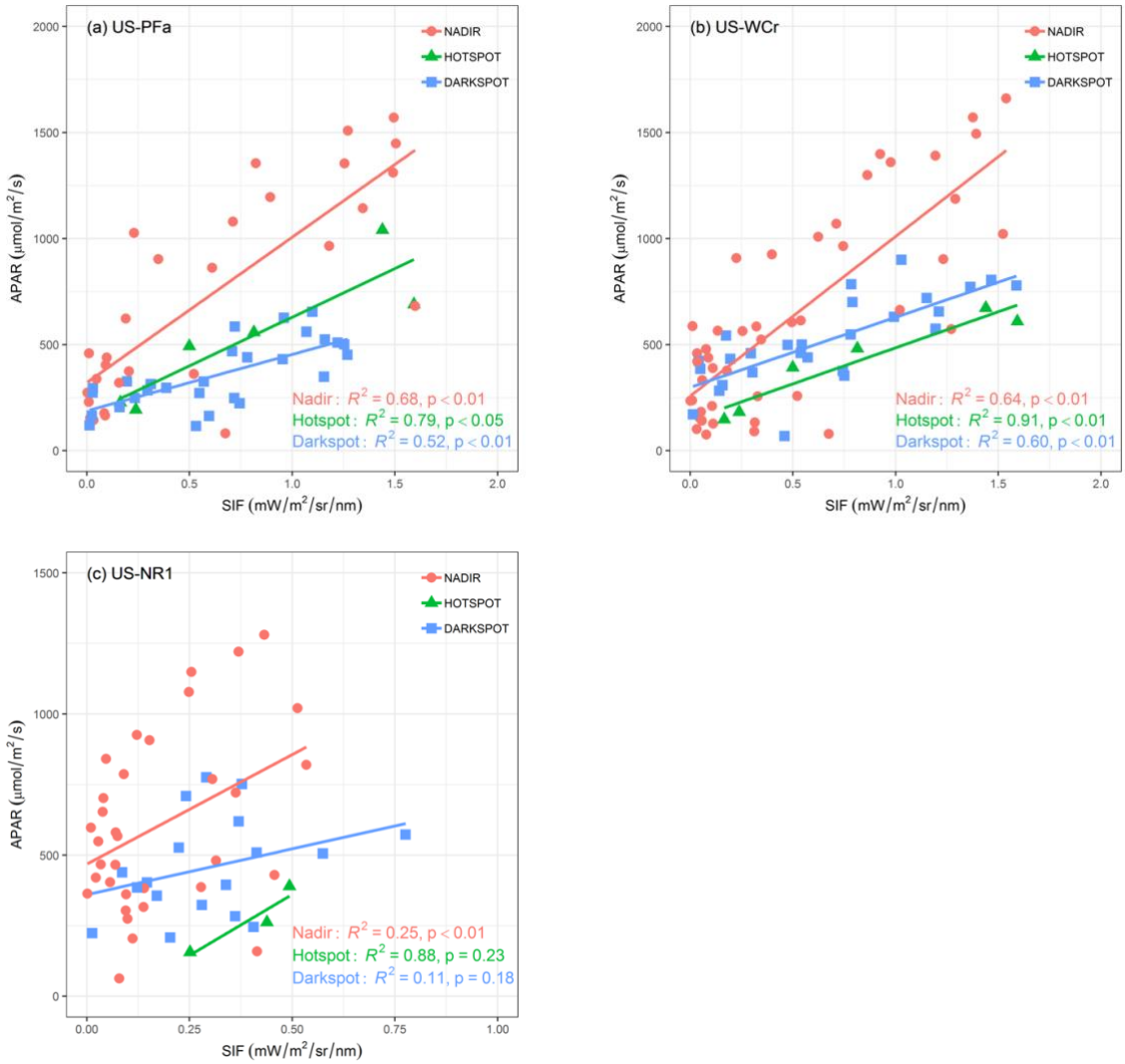


Figure 4.4. The relationship between normalised APAR and OCO-2 SIF at 757 nm in nadir, hot spot and dark spot views for (a) US-PFa, (b) US-WCr and (c) US-NR1. Coloured lines mean the linear regression line for each direction.

### 4.4.4. The correlation between LUE and normalised SIF yield for the nadir, hot spot and dark spot viewing directions

In order to minimise the APAR effects on GPP and SIF, we calculated the LUE ($LUE = GPP/APAR$) to check the relationship between SIF yield and LUE in the nadir, hot spot and dark spot directions for US-PFa, US-WCr and US-NR1 (Figure 4.5 (a) – (c)). In the nadir direction, $SIF_{yield}$ showed high correlation with LUE ($R_2$ = 0.43, p<0.01) at US-PFa but patterns of $SIF_{yield}$ and LUE were not significant in US-WCr and US-NR1 ($R_2$ = 0.07 and 0.1, respectively). In the hot spot direction, $SIF_{yield}$ was significantly positively correlated with LUE in US-PFa and US-WCr ($R_2$ = 0.58 and 0.71, respectively), but for

US-NR1, the correlation was negative and the p-value was more than 0.5. For the dark spot direction, the relationship of $SIF_{yield}$ and LUE had a larger $R_2$ than the nadir direction in US-WCr and US-NR1, but this was less than in the hot spot direction (US-WCr). Compared to non-normalised $SIF_{yield}$ and LUE in the nadir direction, normalised $SIF_{yield}$ from the hot spot direction can more easily explain the 15% and 64% of LUE change in US-PFa and US-WCr, respectively (Figure 4.5 (a)-(b)). Considering that the observed SIF at the nadir direction consisted of both sunlit and sun shade crown areas, it suggested that the pattern of $SIF_{yield}$ and LUE are not the same in sunlit and sun shade crown areas, and sunlit $SIF_{yield}$ might be more sensitive to variations of LUE than other view directions.

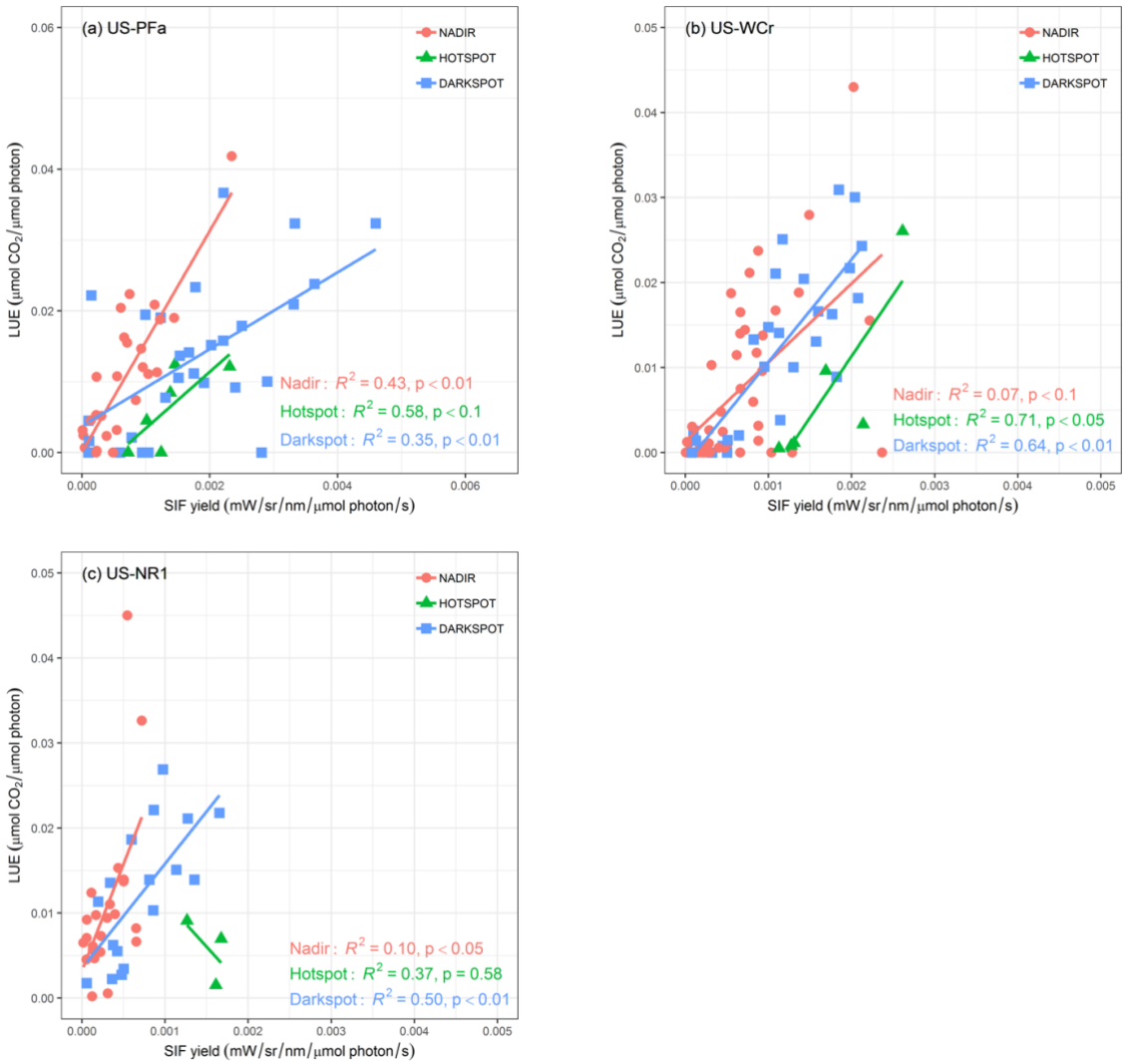


Figure 4.5. The relationship between LUE and normalised OCO-2 SIF yield in the nadir, hot spot and dark spot directions for (a) US-PFa, (b) US-WCr and (c) US-NR1. Coloured lines mean the linear regression line for each view direction.

## 4.5. Discussion

### 4.5.1. View zenith angle effects on the SIF variations

Based on our findings, different VZA of OCO-2 observations leads to different patterns of SIF:GPP and SIF:APAR. We used the three dimensional radiation transfer model, FLiES-SIF (see chapter 2 for more details), to simulate the SIF at the 767 nm in different view zenith angles with fixed SZA and SAA (Figure 4.6). Simulation results suggested that the SIF signal was similar to reflectance, as it had BRDF effects. At the solar principal plane, SIF reached the peak when VZA is coincidental to SZA (VZA = -20°). At the nadir direction (VZA = 0°), SIF was lower than SIF viewed at the hot spot direction and was higher than the dark spot direction (VZA = 20°), however, the SIF value was not the lowest at the dark spot direction. This finding can explain that OCO-2 SIF retrievals are higher at the hot spot and lower at the dark spot direction (Figure 4.2 (a), (c)) and it shows similar properties to reflectance. The results are consistent with the field measurements and one dimensional model simulations (Liu et al. 2016; Van der Tol et al. 2009).

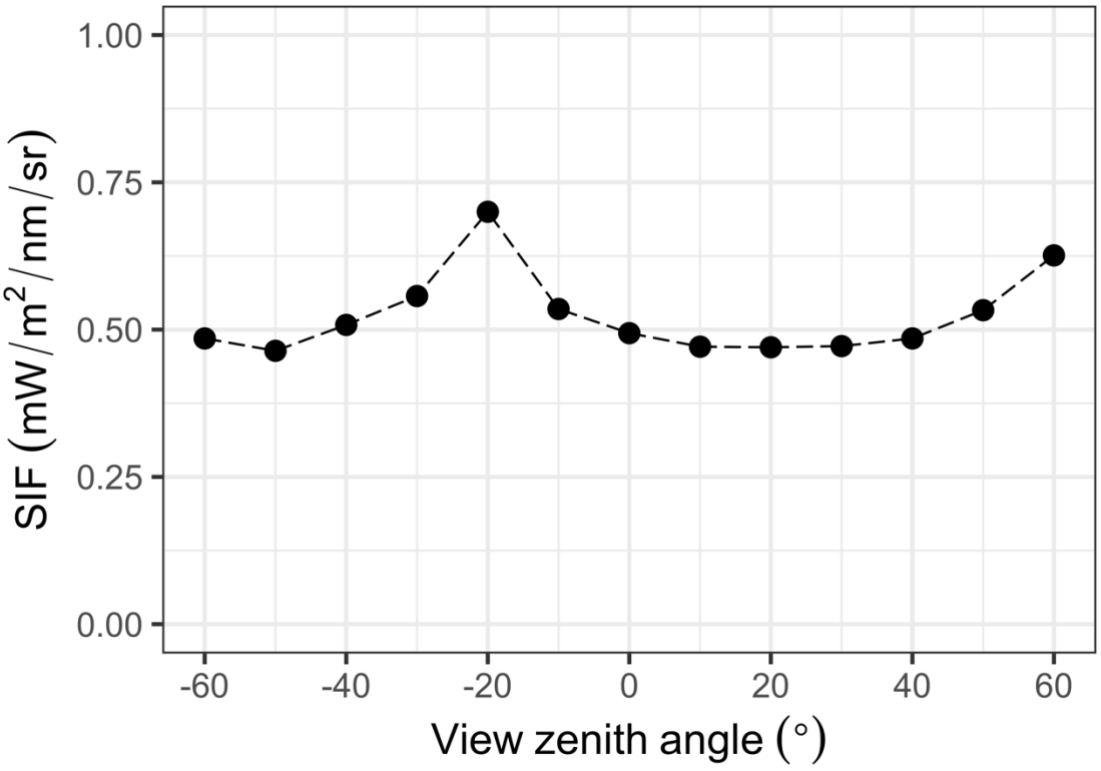


Figure 4.6. FLiES-SIF model simulated SIF at 757 nm at the solar principal plane, and solar zenith angle was set to 20°. SIF value has been scaled from 0 to 1 mW/m2/sr/nm.

Negative values of the VZA mean a backward direction, the positive values signify a forward direction.

### 4.5.2. Normalised SIF of OCO-2 data

In order to minimise the different SZA positions influencing SIF observations, we normalised the SIF by SZA ($SIF_{normalized} = SIF / \cos SZA$) (Köhler, Guanter, et al. 2018). We found the relationship between $SIF_{normalised}$ and $GPP_{EC}$ decreased slightly when compared to non-angular normalization of SIF and $GPP_{EC}$ (Figure 4.7 (a), (b)). The coefficient of determination was decreased by 0.03. This insignificant change means the method, which normalised SIF by SZA, does not effectively influence the relationship between SIF and $GPP_{EC}$. The dataset mainly consisted of SIF retrievals from the nadir direction and dark spot direction, and limited change of SZA (36±12°), and fixed OCO-2 local overpass time had less effect on the correlation of this pattern. In other words, normalizing SIF by SZA can not remove too many angle effects from solar positions.

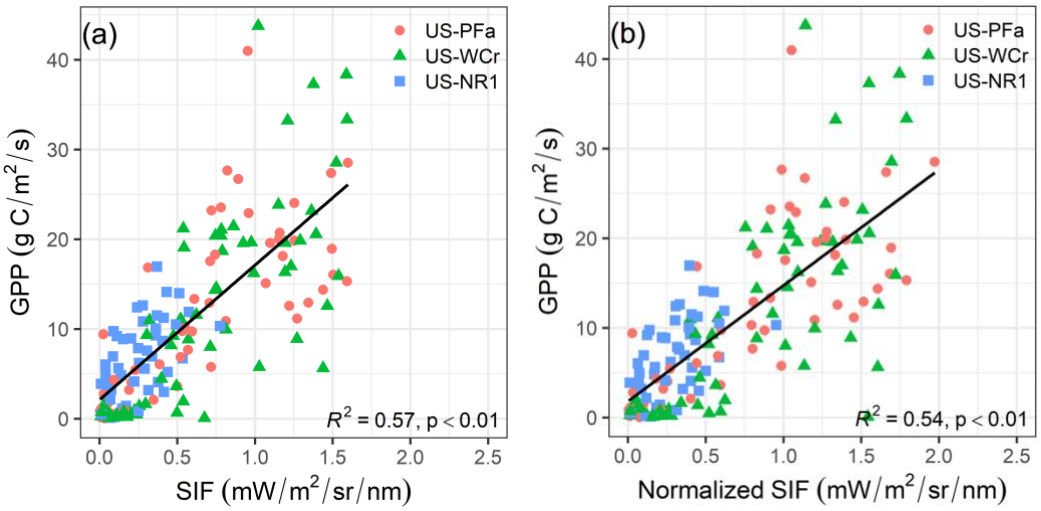


Figure 4.7. (a) The correlation between OCO-2 SIF and $GPP_{EC}$ for three study sites. (b) The correlation between GPP and normalised SIF by SZA for three study sites. The black line means the linear regression line.

In addition, we checked the relationships between LUE:$SIF_{yield}$ and normalised LUE and $SIF_{yield}$ for the total SIF retrievals in our study sites (Figure 4.8 (a), (b)). The results showed that the normalised $SIF_{yield}$ was better correlated with the LUE than the original $SIF_{yield}$ ($R_2$ = 0.39 and 0.48 for normalised and non-normalised $SIF_{yield}$, respectively).

In the previous study, the relationship between $SIF_{yield}$ and LUE could be positive or negative under different light conditions or other environmental stresses (Demmig & Björkman 1987), hence, the relationship between LUE and $SIF_{yield}$ might be different under light-saturating or light-limiting conditions. These conditions could be varied with a different ecosystem and species, and we found normalised $SIF_{yield}$ is positively correlated with LUE for these vegetation types ($R_2$ = 0.39, 0.17 and 0.11, p-value < 0.05, for mixed forest, deciduous broadleaf forest and evergreen needle leaf forest, respectively).

In the hot spot direction, the light easily saturates vegetation before midday on a sunny day. The positive pattern of LUE: $SIF_{yield}$ is consistent with an earlier study (Alton, North & Los 2007). Because of light saturation, with the increase of the PAR, the LUE and $SIF_{yield}$ both tend to decrease, hence, the positive pattern of LUE and $SIF_{yield}$ appeared in the hot spot direction. Furthermore, even though light conditions are strongest in the midday, the positive correlation of LUE and $SIF_{yield}$ still was confirmed (Figure 4.7 (a)). This is consistent with the previous study (Wieneke et al. 2018a), and Van de tol suggested that this relationship can be positive when light is saturated (Van der Tol et al. 2014). In addition, based on diurnal SIF measurements for crops(Pinto et al. 2016), $SIF_{yield}$ normally would experience three periods in a day: increasing capacity, downwards regulation and recovery. During the increasing capacity period, which happens in the morning, $SIF_{yield}$ increases dramatically and LUE decreases with the increase of PAR, hence, the correlation between $SIF_{yield}$ and LUE is negative. During the period of downward regulation, in vegetation experiencing light saturation before PAR reaches the peak, the correlation of $SIF_{yield}$ and LUE is positive ($SIF_{yield}$ decreases with light saturation and LUE decreases with the increasing PAR). However, during the recovery period, the pattern would turn to negative vaues because $SIF_{yield}$ drops slightly, and LUE tends to increase due to the decrease of PAR, hence, OCO-2 observation overpass time may belong to the down regulation period. It contributed to the weak but positive correlation between $SIF_{yield}$ and LUE. Other findings also suggested that the vegetation could adjust their structural and physiological functions to adapt to light saturate conditions (Schlau-Cohen & Berry 2015).

The diffuse PAR can be detected much more in dark spot directions than in hot spot directions. Based on Yang's study for the deciduous broadleaf forest, the LUE and $SIF_{yield}$ both increased while diffused PAR fractions accounted more in total incident of PAR

(Yang et al. 2015b), hence, the pattern of LUE and $SIF_{yield}$ was also significantly positive for all sites in the dark spot direction. In addition, the measuring time of OCO-2 SIF guarantees high diffuse PAR from the shaded crown area (solar intensity is strong at midday), the pattern of LUE and $SIF_{yield}$ would change to negative in the light-limiting time (early morning or late afternoon) (Van der Tol et al. 2014). Due to PAR dropping while the light is limited in the afternoon, and $SIF_{yield}$ decreasing as well, but LUE increasing, the relationship would change to negative (Miao et al. 2018). This phenomenon suggests that more studies should check the relationship over diurnal and seasonal scales (Guan et al. 2018). Even when considering the path of photons through the canopy, lower incident radiation leads to lower SIF emission, so the SIF from the deep shaded leaf are is lower than SIF from the top and middle shaded layers (Pinto et al. 2016).

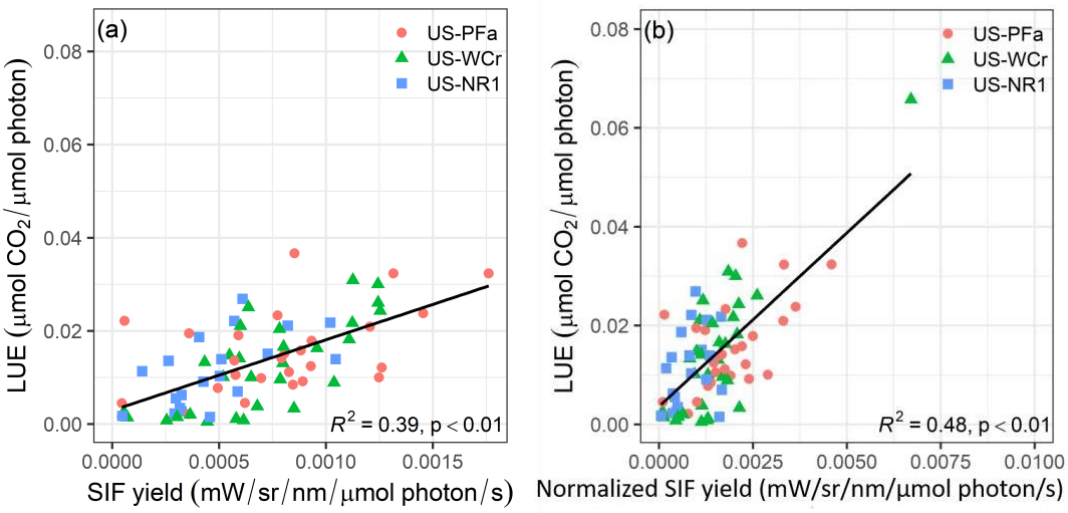


Figure 4.8. (a) The correlation between OCO-2 SIF yield and LUE for three study sites. (b) The correlation between normalised LUE and normalised SIF yield by APAR for three study sites. The black line means the linear regression line.

### 4.5.3. Relationship between environmental factors and SIF observations in different view observations

We checked the relative contribution from environmental factors (VPD, Ta, SWC, PAR, and NEE) to different SIF view directions in US-PFa, US-WCr and US-NR1 (Figure 4.9). In the nadir direction, the NEE contributed nearly a half (47.97%) to the SIF variation. Air temperature accounted for 29.81% which was less than NEE. Interestingly, PAR is

not the significant factor which effects SIF in the nadir direction (only 8.65%, the third in order).

In the hot spot direction, the PAR contributed the most to the sunlit SIF (34.06%). The apparent results suggested that PAR was the main contributor to the SIF variation for the sunlit crown area. Because the leaves are exposed to the the direct sunlight, the SIF is mainly driven by direct PAR. The strong direct PAR leads to higher SIF emission (Damm et al. 2015a). Sunlit leaf contributes mostly to GPP, but the NEE is less prominent in the hot spot direction (19.11%). It can be seen that sunlit SIF is highly correlated with GPP (Figure 4.3). With the high temperature and VPD at midday, the respiration is low and the ability of leaf stomatal conductance decreases, so the Reco is limited at the sunlit crown area (Reddy, Baker & Hodges 1991). However, in the meantime the GPP increases, so the negative pattern between NEE and Reco may lower the importance of Reco to the variation of sunlit SIF ($NEE = GPP + R_{eco}$).

In the dark spot direction, without the direct PAR effects, the air temperature and VPD might replace PAR as the main factors that affect SIF variation. Ta appeared to be the most crucial factor of the SIF variation (42.51%). NEE and VPD similarly contributed to the SIF change (24.55% and 26.03%, respectively). PAR contributed less to sun shade SIF variation when compared with the hotspot spot direction. It implied the PAR does not dominate the SIF variation for sun shade leaves. As the most important factor, Ta dominated the SIF variation in the dark spot and this may because the sun shade crown area avoids the effects of light-saturation. Hence, SIF variation in the sun shade crown area might be more sensitively responsive to the Ta and VPD because strong positive correlation between SIF and VPD ($R_2$ = 0.69) was found (Shan et al. 2019). In addition, Van der tol used the SCOPE model to simulate the temperature from the sun shade area and found Ta was cooler than the sunlit area in the dense tree area (Van der Tol et al. 2009), hence, cooler temperatures may influence the variations of SIF in the sun shade area.

As with Shan's findings, SIF and VPD both decreased at the midday at the diurnal scale. Because the canopy stomatal conductance was much more sensitive to the variation of VPD, and influenced by the SIF variations (Shan et al. 2019). It is possible that before SIF was affected by light saturation, the stomatal conductance might already respond to

the high temperatures and constrain the plant transpiration. This is worth further investigation and more experiments to should be carried out in future.

Finally, it should be noted that the soil water content is the factor which is the weakest factor influencing SIF variation in all viewing directions. It suggests that SWC does not directly or timely affect SIF for the deciduous broadleaf forest, mixed forest and evergreen needle leaf forest.

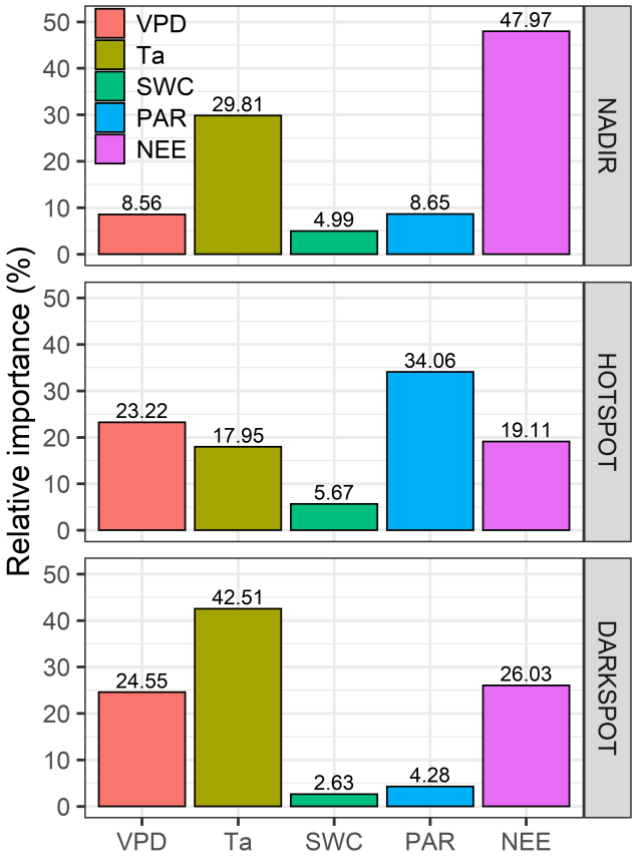


Figure 4.9. Relative importance of VPD, Ta, SWC, PAR and NEE for SIF viewing in nadir, hot spot and dark spot direction.

### 4.5.4. Applications of remotely sensed SIF observations

Normally, the SIF satellite (GOME-2 and TROPOMI) observes at the nadir direction. Based on our findings, it might underestimate the SIF: $GPP_{EC}$ relationship (Figure 4.3 (a)-(c)). In addition, our finding suggests that VZA influence on the pattern of SIF and $GPP_{EC}$ is limited (Figure 4.7). SIF: $GPP_{EC}$ relationship is prone to influence by the sensor view positions.

Previous study normalised OCO-2 and GOME-2 incident PAR and SIF bands, and the results showed the times series of these two satellite agrees well (Köhler, Guanter, et al. 2018). However, SIF variation changes dramatically over the course of a day and the correlation between $SIF_{yield}$ and LUE also changed under light condition variations, so satellite observations may hide the SIF responding to environmental stress. Some studies suggested scaled SIF, from instantaneous to daily by a multiplied scale factor, would also miss the changing of clouds, temperature and other environmental factors (Zhang, Xiao, et al. 2018).

At OCO-2 local overpass time, sunlit $SIF_{yield}$ decreases due to the light saturation, and sun shade SIF yield may also under recovery because of the high VPD and low canopy stomatal conductance, therefore, decreasing LUE leads to a positive pattern. If the satellite local overpass time is before the light saturation of the vegetation, the pattern should be different. For example, the GOME-2 overpass time is at 9:30, the SIF yield would be increased but LUE would decrease because of the increasing of PAR, however, the coarse spatial resolution of GOME-2 data would minimise or ignore this pattern.

Considering the field measurement, the BRDF effect will influence the SIF retrieval. Because of the fixed angle of the sensor, with the movement of the solar and limited field of view (FOV), the sensor would monitor the area with both sun shade leaf and sunlit leaf in a day, their different patterns would affect the results, and their NPQ (Non-photochemical quenching) would be different (Schlau-Cohen & Berry 2015). These issues bring uncertainties to field measurements, for example; at the leaf level, sunlit leaf's NPQ is higher than that of the shaded leaf (Majer et al. 2014). Hence, the fluorescence yield of the sunlit leaf is less than that of the sun shade leaf under the same weather conditions, therefore identification as to whether the leaf is a sunlit or sun shade leaf would be important. Furthermore, it is important to note the bidirectional effects of SIF. At the canopy level, vegetation itself can adapt to the variation of light conditions, for example, the soybean can adjust their leaves' inclination to respond to the direction and intensity of sunlit (Miao et al. 2018). Also, while the plants suffer stress, the SIF from sunlit leaf might show a stronger performance than a sun shade leaf because it is natural for a sunlit leaf to experience light saturation and this might hide the main stress. Hence, SIF from sun shade might be more suitable for studying the plant response to environmental stress. Further field measurements are needed to explore this issue.

## 4.6. Conclusion

In this study, we found there existed a strong relationship between SIF and GPP at the hot spot direction for all three sites, US-PFa, US-WCr and US-NR1 ($R_2$ = 0.95, 0.95 and 0.88, respectively). This suggests that the hot spot SIF can better explain GPP changes than SIF from other viewing directions. We also utilized a 3-D radiative transfer model, FLiES, to calculate the relative APAR for the different view observations. The results showed that correlations between SIF and normalised APAR, normalised $SIF_{yield}$ and LUE (at all viewing directions) become stronger than the non-normalized $SIF_{yield}$ ($R_2$ increased from 0.39 to 0.48 for $SIF_{yield}$:LUE). We also found a positive relationship between $SIF_{yield}$ and LUE at both hot spot and dark spot directions. It implies the positive pattern existing in light-saturating or light-limiting conditions. Moreover, the flux data was used to check the relative importance for SIF in the nadir, hot spot and dark spot directions. PAR and Ta are the primary contributors to the SIF variations in the hot spot direction and dark spot direction, respectively. Soil water content contributed less to these three directions. In summary, these findings will be of benefit to the study of the BRDF effect on the SIF variations. Also, the normalised method will be useful to study the relationship between $SIF_{yield}$ and LUE at the regional scale.

# Chapter 5. Sun-induced chlorophyll fluorescence is influenced by the understory reflectance based on two scenarios

## Abstract

Sun-induced chlorophyll fluorescence (SIF) has been widely used to explore the relationship with plant photosynthesis activity and to estimate gross primary productivity (GPP). SIF is sensitive to environmental stress, such as heat and water deficit stress. However, SIF and GPP have presented strong correlations in dense canopy areas, but weaker correlations have been found over sparsely vegetated areas ($R^2$ is lower than 0.2). Hence, it is important to identify factors that affect SIF emission and scattering amidst variations of canopy structures as well as possible impacts of the canopy understory. In this study, we investigated two scenarios that potentially may affect the transfer of fluorescence photons; (1) $SIF_{SI}$: emitted fluorescence photons reflected by the understory and (2) $SIF_{SII}$: reflected photons from the active understory leaves to emit photons. Moreover, a database was generated to cover 3150 conditions of five variable factors, including fractions of vegetation cover (FVC), understory reflectance ($\rho_u$), leaf density ($d_{leaf}$), total chlorophyll content (Cab) and leaf structure (N). A three-dimensional model, FLiES-SIF, was applied to the database to conduct SIF simulations following the rules of the two understory scenarios. The results showed that $\rho_u$ was the critical factor that impacted both $SIF_{SI}$ and $SIF_{SII}$. Understory reflectance also influenced canopy SIF, especially in sparse vegetation areas. Leaf structure did not significantly affect SIF for the two scenarios. A strong correlation between $SIF_{SI+SII}$ and all five factors was found ($R^2$ = 0.42 and 0.49 for red and far-red SIF, respectively). This latest study will improve our understanding of fluorescence transfer between overstory and understory layers and the analysis of error and uncertainties in observed SIF measurements.

## 5.1. Introduction

Sun-induced chlorophyll fluorescence (SIF) is the latest approach to detect photosynthetic activities from the leaf on a global scale (Frankenberg & Berry 2018; Porcar-Castell et al. 2014; Ryu, Berry & Baldocchi 2019). The fluorescence is generated during the photosynthesis (part of the energy escapes to space as fluorescence) (Schlau-Cohen & Berry 2015). Usually, the fluorescence quantum yield accounts for only 1% of the total energy (Frankenberg & Berry 2018). Spectrum SIF (chlorophyll a and b) mainly exists between 640 and 850 nm (Gu et al. 2019b), which covers the red and far-red spectrum. The shape of the SIF spectrum contains two peaks; one is at 685 nm (red SIF), another is at 740 nm (far-red SIF). The far-red SIF contains information of both photosystem I (PSI)

and photosystem II (PSII), and the red SIF only carries the information of photosystem II (Yang et al. 2015b). With the distinctive characteristics of the red spectrum and far-red spectrum, SIF is similarly inherits its specification, which suggests red SIF is prone to be absorbed by leaves (Damm et al. 2015a; Van Wittenberghe et al. 2015). This trait contributes to the distinctive scattering effect of red SIF and far-red SIF.

As the newest approach for detecting photosynthetic activity, SIF has several applications spatially and temporally. Due to the close relationship between photosynthetic activity and SIF, SIF is used to estimate gross primary productivity (GPP) (Guanter et al. 2014a; Sun et al. 2018). Researchers have found there is an existing universal linear regression of GPP and SIF among diverse vegetation function types (Li et al. 2018). Wang found SIF can be used to study the phenology and accurately confirm the status of vegetation growing seasons in northern Australia (Wang et al. 2019). Additionally, SIF can be used to estimate the crop's productivity and reflect the vegetation health conditions relative to extreme events (Song et al. 2018a).

Many satellites have been launched to monitor SIF from space. GOME-2 as the most popular SIF satellite provides two bands of SIF (687 and 760 nm) in 40 $km^2$ (Joiner et al. 2013; Joiner et al. 2016). The coarse spatial resolution cannot present the "true" relationship between SIF and GPP in sparse vegetation areas and errors occur in pixels that include several vegetation types. In addition, the degradation of the GOME-2 sensor makes it not suitable for long-term observations. OCO-2 provides SIF data in 740 nm from 2014 (Sun et al. 2017), and its spatial resolution is 1.29 km × 2.25 km, but the discontinued observations cause difficulties for time series analysis. TROPOMI is the latest launched SIF satellite (Guanter et al. 2015; Köhler, Frankenberg, et al. 2018), and provides almost daily revisits and acceptable spatial resolution (7 km × 3.5 km). However, monitoring from space brings many uncertainties. First, SIF varies dramatically over a day (Paul-Limoges et al. 2018; Pinto et al. 2016; Wieneke et al. 2018a; Yang, Ryu, et al. 2018), scaling the instantaneous SIF to daily SIF cannot reveal the true conditions of the vegetation. Second, the mixed multi-vegetation types are prone to involve errors which would impact long-term analysis (Aasen et al. 2019; Magney et al. 2019).

Currently, some models can simulate the SIF for various purposes. The SCOPE (Soil Canopy Observation, Photochemistry and Energy fluxes) model is the most widely used one-dimensional radiative transfer model (Tol et al. 2009). Due to the complex vegetation structures, it cannot reveal the distribution of photons vertically. FluorWPS and

FluorFlight as the newly developed three-dimensional models can simulate SIF for heterogeneous vegetation (Hernández-Clemente et al. 2017; Zhao et al. 2016). They are both based on the Monte Carlo and ray-tracing methods and adapted excite-fluorescence matrix (EF-Matrix). However, FluorWPS has been validated for crops, but it currently awaits development to be able to validate different vegetation types, and neither model analyses the effects from the canopy understory.

SIF is not only influenced by leaf properties (chlorophyll content and leaf structure) but also affected by environmental factors, such as radiation, air temperature and vapour pressure deficit (VPD) (Shan et al. 2019). The chlorophyll content of leaf has been confirmed that it affects both red and far-red SIF. The SIF signal is primarily affected by absorbed photosynthetically active radiation (APAR), which is a proper proxy for APAR in the deciduous broadleaf forest (Yang et al. 2015b), but is not suitable for evergreen needle forest (Magney et al. 2019). The canopy structure (LAI) showed a positive correlation with the SIF emission (Yang et al. 2017).

Many SIF studies were focused on canopy structure and environmental factors, but the understory effects on SIF observations have been ignored by researchers. Yang used the SCOPE model to identify the relationship between reflectance and the fraction of scattering SIF, and he assumed the no photons were reflected from the understory (Yang & Van Der Tol 2018). This assumption might lead to misunderstanding in the case of sparsely vegetated areas. Similarly, Zeng assumed the soil was non-reflective when he was studying the escape ratio (Zeng et al. 2019). Additionally, when monitoring the understory SIF, researchers found that the understory SIF also contributed to the total observed SIF but with less seasonal variations (Kato et al. 2018). This implies the understory SIF contribution still needs exploration.

In this study, we aimed to examine how the canopy understory influences observed SIF coupled with leaf properties and canopy structures. We implemented a new developed SIF module for a three-dimensional radiative model (FLiES) to generate a database covering 3150 conditions. Moreover, we checked understory influences based on two scenarios. Our objectives were to (i) identify scenarios which would affect the observed SIF from the understory and generate a database for examining different conditions, (ii) study the canopy structure, leaf properties and understory reflectance influences on certain scenarios, (iii) summarize the relationships between the effects and factors, and apply the relationship to analysis of implicit factors affecting the SIF observation in sparse

and dense vegetation areas. This research will be useful for understanding how the understory layer contributes to the SIF variations.

## 5.2. Definition for two scenarios

In this section, we described two scenarios which was set up for studying how understory layer affects SIF. One is that a fluorescence photon has left the leaf, and is observed when it is reflected by the understory layer. It is observed by the sensor at the top of the canopy (TOC). The other scenario is when the non-fluorescence photon is reflected from the understory layer and activates the leaf to emit fluorescence. We used $SIF_{SI}$ to present the SIF observation based on the rule of scenario I, $SIF_{SII}$ a represented the SIF observation based on the rule of scenario II (Figure 5.1).

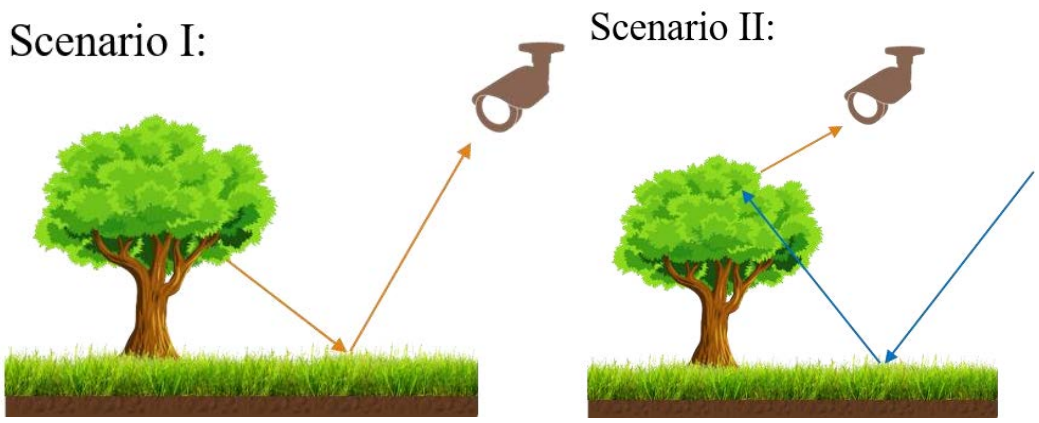


Figure 5.1. Descriptions for scenario I and II.

### 5.2.1. Scenario I

Based on the rule of scenario I, a fluorescence photon's energy is less than the fluorescence emitted from the canopy because of the reflection from the understory. However, the incoming fluorescence is complex as for the emitted fluorescence may come from the leaf from a backwards or forwards direction which is generated by the backward and forward EF-Matrix. The scattering fluorescence may be reflected by leaf or stem and transmit from the thin leaf. Note, fluorescence is a variant spectrum. The red fluorescence may reach the understory less due to the high absorption of the leaf. Compared to the red fluorescence, the scattered far-red fluorescence reflected by the understory may be more easily observed by the sensor.

### 5.2.2. Scenario II

For scenario II, fluorescence is activated by the non-fluorescent photon from the understory (we assumed no fluorescence was emitted from the understory). After reflecting from the understory, deeper leaves of the canopy (close to the ground) are prone to be illuminated by the reflected photon and have a lower chance of experiencing light-saturation because of the energy consumption from reflection at the understory. When considering the multiple scattering at the understory layer, the first-ordering of photons carried much more energy than multiply scattered photons, and they contribute to the more considerable fluorescence which are activated by the 1-ordering of a photon at the leaf level. Due to the fact that this scenario does not involve the scattering effect of a fluorescence photon, the observation of the red fluorescence and far-red fluorescence is not distinct.

In addition, canopy structure and leaf properties would affect SIF in these two scenarios. For example, under the high fraction of vegetation cover (FVC), the canopy intercepting ($i_0$) would lower the probability of a photon being reflected from the understory layer. The lower canopy chlorophyll content ($c_{ab}$) will decrease the fluorescence emission and reflectance. Furthermore, it will impact on the fluorescence transferrance in both scenarios, hence, we will use a three-dimensional model to simulate SIF under these two scenarios and examine the fluorescence effected by the understory.

## 5.3. Theoretical basis

### 5.3.1. Incident radiation on canopy and understory

Fluorescence is mainly activated by photosynthesis active radiation (PAR), which ranges from 400 to 750 nm. Based on our defined scenarios, incidental PAR comes from direct sunbeams without any collision with leaf or stem or being reflected by the understory, hence, the incidental PAR for the scenario I and II can be written as equation 5-1 and 5-2, respectively.

$$E_c(\lambda) = i_0 E(\lambda) \tag{5-1}$$

$$E_u(\lambda) = (1 - i_0) E(\lambda) \rho_u(\lambda) \tag{5-2}$$

$i_0$ is the intercepting canopy, it varies with the FVC, leaf density (total one side leaf area per unit volume) and leaf inclination. $E(\lambda)$ presenteds incidental irradiance for spectrum

$\lambda$. The incidental irradiance from the understory layer ($E_u(\lambda)$) is multiplied by understory reflectance ($\rho_u(\lambda)$).

Fluorescence from the canopy to understory can be written as the summary of emitting fluorescence ($f_e(\lambda_f)$) and scatter fluorescence ($f_s(\lambda_f)$) at the wavelength $\lambda_f$. $f_e$ equals to the backward and forward excited-fluorescence matrix ($M_f, M_b$) multiplied by the incidental radiation. We used the symbol $M$ to present the summary of $M_f$ and $M_b$.

$$f_c(\lambda_f) = f_e(\lambda_f) + f_s(\lambda_f) \tag{5-3}$$

$$f_e(\lambda_f) = E_l(\lambda_f) \int_{400}^{750} [M_f(\lambda_f, \lambda_e) + M_b(\lambda_f, \lambda_e)]\, d\lambda_e = E_l(\lambda_f) M(\lambda_f) \tag{5-4}$$

$$f_s(\lambda_f) = f(\lambda_f) \rho p_+ + f(\lambda_f) \tau p_- \tag{5-5}$$

$$E_l(\lambda) = B_s P_s E(\lambda) \tag{5-6}$$

$E_l(\lambda)$ means the radiation at the leaf level and the given observation direction. $B_s$ means whether the fluorescence can be observed by the sensor ($B_s = 1$ means be observed, 0 means not). $P_s$ means the projection of the leaf in the view direction. $p_+$ means the probability of fluorescence reflection, $p_-$ means the probability of fluorescence transmission.

## 5.3.2. Formula description for the scenario I

Based on the description of scenario I, the fluorescence radiance ($f_{SI}(\lambda_f)$) can be written as,

$$f_{SI}(\lambda_f) = [f_e(\lambda_f) + f_s(\lambda_f)] P_{SI} \rho_u(\lambda)\, B_o \tag{5-7}$$

It means the fraction of downward fluorescence reflected by the understory can be seen by the sensor. $B_o = 1$ means reflected fluorescence can be captured by the sensor, $B_o = 0$ means it is hindered by a canopy. $P_{SI}$ means the fraction of fluorescence downwards to the understory. Hence, the $f_{SI}$ is mainly affected by understory reflectance and $P_{SI}$. $P_{SI}$ is varied with the FVC.

## 5.3.3. Formula description for Scenario II

The fluorescence ($f_{SII}(\lambda_f)$) which is activated by reflected photons from the understory is shown in the following formula

$$f_{SII}(\lambda_f) = E_u(\lambda) f_e(\lambda_f) P_{SII} B_o \tag{5-8}$$

$$\begin{aligned} f_{SII}(\lambda_f) &= E_u(\lambda) P_{SII} B_o P_s \int_{400}^{750} \left[ M_f(\lambda_f, \lambda_e) + M_b(\lambda_f, \lambda_e) \right] d\lambda_e \\ &= E_u(\lambda) P_{SII} B_o P_s M(\lambda_f) \end{aligned} \tag{5-9}$$

Where $P_{SII}$ is the fraction of reflected fluorescence which can reach the canopy. Hence, $f_{SII}$ is primarily affected by canopy interception, understory reflectance and Cab.

## 5.4. FLiES SIF simulation method

We examined these two scenarios with the FLiES-SIF model and generated a database which covered a large number of variations of canopy structure, understory reflectance and leaf properties. For each scenario, we saved the results of first-order interactions and multiple interactions in order to identify the fluorescence's energy consumption with increasing interactions. Red and far-red fluorescence (685 and 740 nm, respectively) were selected to check their variations with different situations. These two fluorescence bands are widely used in applications for detecting canopy stress (Köhler, Frankenberg, et al. 2018).

### 5.4.1. FLIES SIF model and ray-tracing frame

The FLiES-SIF model is a newly developed SIF module (see Chapter 2 for more details) for the three-dimensional radiative transfer model FLiES (Forest Light Environmental Simulator, version 2.48) (Kobayashi & Iwabuchi 2008). The FLiES model, based on Monte Carlo and ray tracing method, is suitable to identify the travelling condition of fluorescence in the 3D scene. Based on the setting of the FLiES model, it consists of four layers: atmosphere, canopy, understory and soil. Before the simulation, a large number of photons are uniformly distributed at the top of the 3D scene. Processed by the atmosphere model, every photon carries its weight and travels in a given direction. When a photon collision with the leaf in canopy layers occurs, the SIF module will check the photon's wavelength, and calculate excited fluorescence based on the incident photon's weight, direction, backward or forward EF-Matrix and normalisation of the leaf surface. The newly generated fluorescence photons will be pushed to a stack and their information stored. Later, they will be simulated when a current non-fluorescence photon escapes the scene or consumes all its weight by reflection, transmission and absorption. The

fluorescence in the stack will be transferred, which follows the ray tracing rules of a standard photon in the 3D scene until its weight is consumed or it escapes out of the scene.

In order to simplify the simulation, we assumed the understory vegetation layer could not emit fluorescence when a photon reaches this layer. The reflectance of the understory layer and soil layer was set at the same value. Whether a reflected fluorescence or non-fluorescence photon returns to the canopy depends on the FVC and the direction it is reflected.

### 5.4.2. Database generation

The input database for FLiES-SIF model consists of 3150 conditions (Table 5.1). It includes 15 combinations of leaf properties and 42 combinations of canopy structures (FVC and $d_{leaf}$). We set the PPFD (Photosynthetic photon flux density), solar zenith angle and azimuth angle as the default. The viewing mode is from nadir. In order to present the variations of FVC in the 3D scene, we randomly distributed trees in a 30×30 $m^2$ area based on fractions to present the FVC varying from 5% to 100%. The shape of the crown is set to cone, and the radius of the crown ranges from 3 to 6 meters. The height of the trees is the same. The leaf inclination is a uniform distribution.

Table 5.1. Database for FLiES-SIF model simulations

| Parameter | Explanation | Values | Unit |
|---|---|---|---|
| N | Leaf structure parameter | 1, 1.5, 2 | - |
| $C_{ab}$ | Chlorophyll a and b content | 5, 10, 20, 40, 80 | $\mu g cm^{-2}$ |
| $C_{car}$ | Carotenoid content | One quarter of $C_{ab}$ | $\mu g cm^{-2}$ |
| $C_w$ | Water thickness | 0.02 | cm |
| $C_m$ | Dry matter | 0.01 | $g cm^{-2}$ |
| FVC | Fraction of vegetation cover | 0.05, 0.1, 0.2, 0.4, 0.6, 0.8, 1 | - |
| $\rho_u$ | Understory reflectance | 0.1, 0.2, 0.3, 0.4, 0.45 | - |
| $d_{leaf}$ | Leaf density | 0.1, 0.2, 0.4, 0.6, 0.8, 1 | $m^2/m^2$ |
| $\theta_s$ | Solar zenith angle | 30 | degree |
| $\theta_a$ | Solar azimuth angle | 0 | degree |
| PPFD | Photosynthetic photon flux density | 600 | $\mu mol m^{-2} s^{-1}$ |

The reflectance and transmittance of the leaf and EF-Matrix were generated with biochemical parameters (N, $C_{ab}$, $C_{car}$, $C_w$, $C_m$) by the PROSPECT (Feret et al. 2008) and FLUSPECT models (Vilfan et al. 2016), respectively. The fluorescence radiance contribution to Scenario I and II will be saved during the simulation.

## 5.5. Results

### 5.5.1. The variation of SIF with Cab, $d_{leaf}$, $\rho_u$ and FVC

Figure 5.2 shows the SIF variation with total chlorophyll content at 680 nm and 740 nm. We can see that total SIF, scatter SIF and emit SIF at 680 nm decreased with the increasing of Cab because of the high absorption of leaves for the red SIF. In addition, a lower Cab of the leaf can lead to high reflection of fluorescence because of the negative correlation between Cab and reflectance at the red spectrum light (Shiklomanov et al. 2016). The total SIF mainly consisted of the emitting SIF at Cab ranging from 40 to 80 µgcm-2.

Compared to the red SIF, the far-red SIF presented a positive pattern with Cab. The scatter SIF showed a similar pattern to emitting SIF, however, they reached the peak and kept stable from 40 µgcm-2 of Cab. The value of scattered SIF at the far-red region was much more than the red SIF hence, the influence that Cab had on both red and far-red SIF was between 5 to 40 µgcm-2.

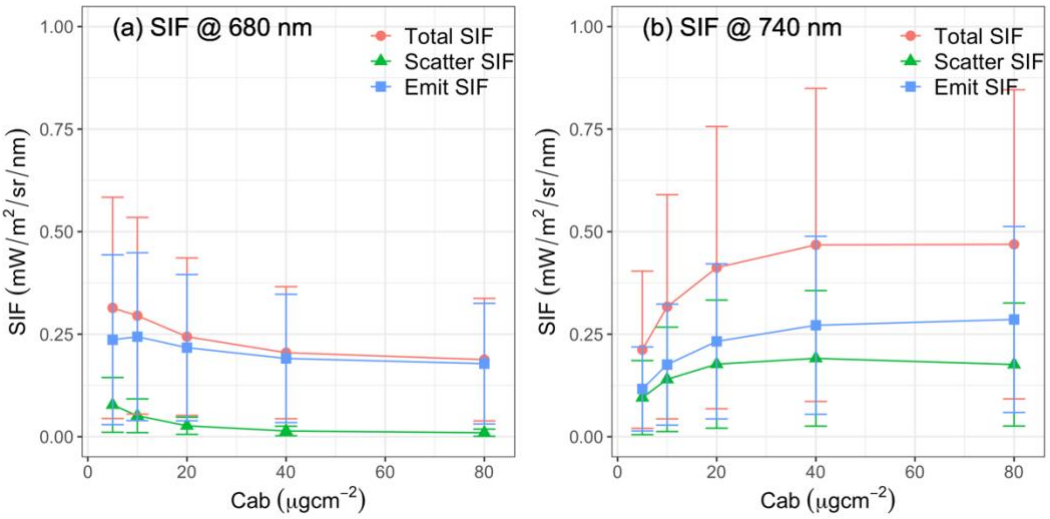


Figure 5.2. FLiES-SIF model simulated total SIF, scatter SIF, emit SIF based on the variation of total chlorophyll content at (a) 680 nm and (b)740 nm.

Figure 5.3 shows the SIF variation with the leaf density at 680 and 740 nm. Red SIF and far-red SIF showed the same trend with increases in leaf density. They increased with the lower leaf density to dense leaf of the canopy. Scatter SIF stood for a tiny fraction of total SIF at 680 nm. Oppositely, scatter SIF accounted for one-third of the far-red total SIF. Hence, Figure 5.3 suggested that the observed red and far-red fluorescence was higher at the leaf dense area.

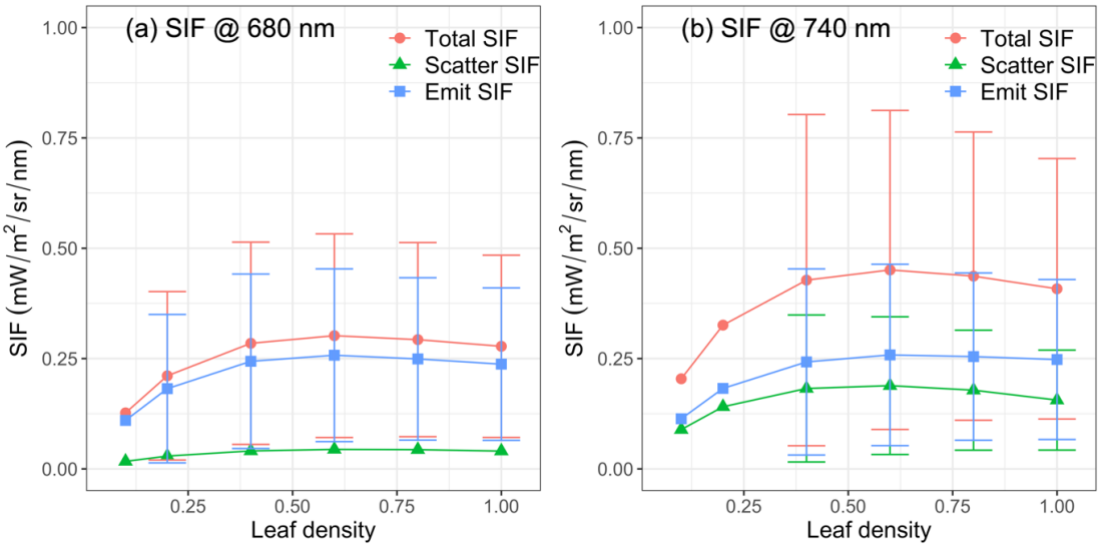


Figure 5.3. FLiES-SIF model simulated total SIF, scatter SIF, emit SIF based on the variation of leaf density at (a) 680 nm and (b) 740 nm.

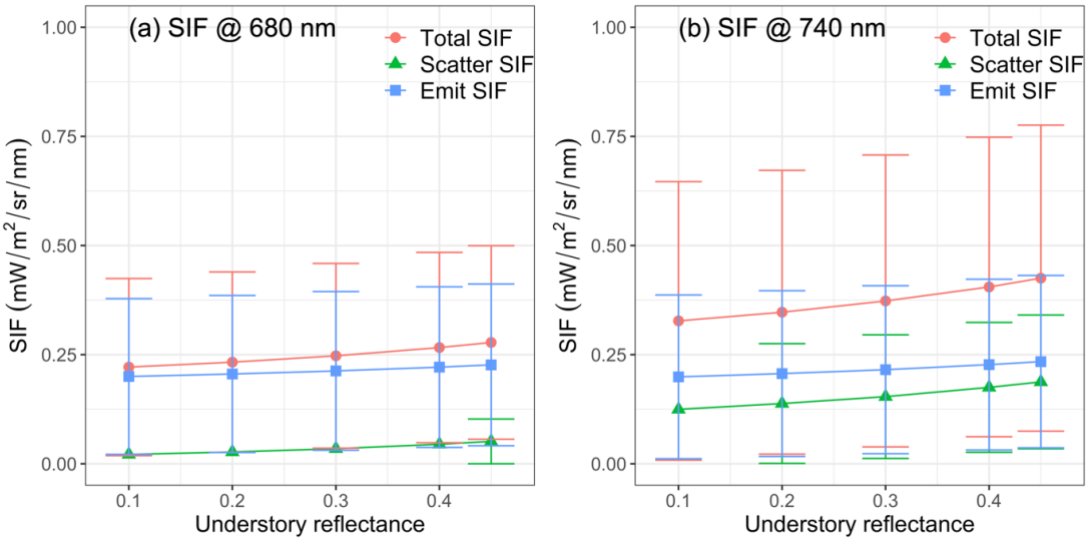


Figure 5.4. FLiES-SIF model simulated total SIF, scatter SIF, emit SIF based on the variation of understory reflectance at (a) 680 nm and (b) 740 nm.

Compared to the leaf density and Cab influences on SIF, the effects of the understory reflectance were less on both red and far-red total SIF. The variation of red SIF was 0.19±0.04 mW/m2/sr/nm, 0.28±0.08 mW/m2/sr/nm for far-red SIF.

Among several factors (Cab, leaf density, understory reflectance, and FVC), FVC is the factor which mostly influences SIF variations in both red and far-red SIF (Figure 5.5). The variation of red SIF was 0.21±0.26 mW/m2/sr/nm, 0.32±0.4 mW/m2/sr/nm for far-red SIF. At the lower vegetation cover area, it suggested that there was less leaf emissions of fluorescence by light activation. At the dense canopy area, more leaf can be illuminated by the sun, and more fluorescence can be observed by sensor. However, we noted the scatter SIF at 680 nm was slightly raised with the increase of the FVC (Figure 5.5 (a)). It suggested that red scatter SIF is limited even though more red SIF was emitted at the dense canopy area. This phenomenon is helpful for studying the total SIF due to the large ratio of the emit SIF and total SIF at 680 nm.

In summary, scattered SIF and emitted SIF responded in a similar fashion to the variation of the structure and leaf properties in the far-red region, however, the red scattered SIF cannot explain the change in these factors due to the high absorption of the leaf. Moreover, red SIF has a negative pattern with the leaf chlorophyll content.

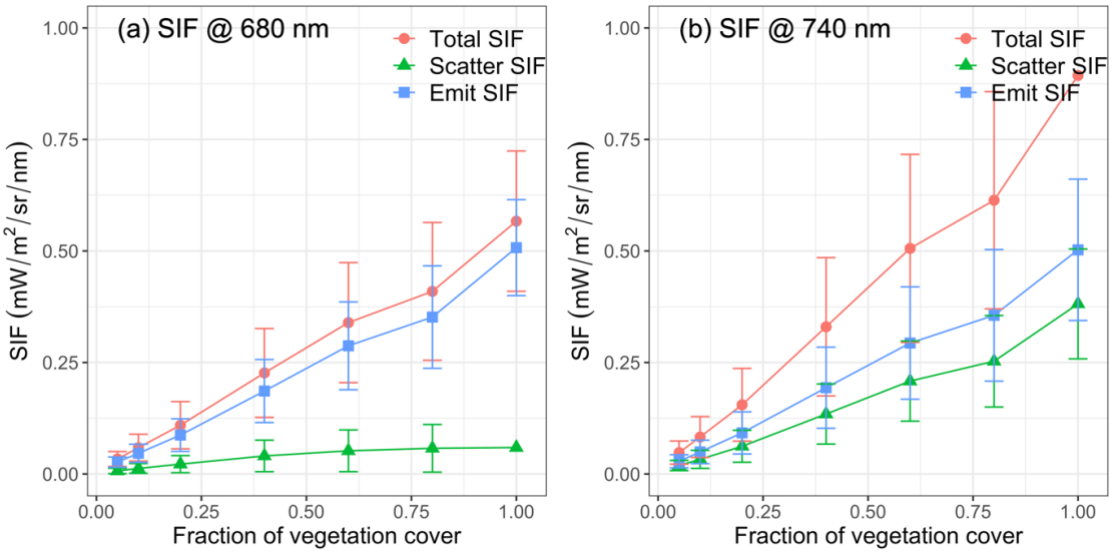


Figure 5.5. FLiES-SIF model simulated total SIF, scatter SIF, emit SIF based on the variation of total chlorophyll content at (a) 680 nm and (b)740 nm.

### 5.5.2. Environmental factors effects on red and far-red SIF for scenarios I and II

In this section, we examined the understory effects on SIF in scenarios I and II for variations of understory reflectance, the fraction of vegetation cover, leaf density and total chlorophyll content. We focused on the changing of the scattered SIF in the scenario I, because the observed fluorescence photon, which is reflected from the soil, belongs to the scatter SIF. However, for scenario II we only checked the emitted SIF due to the reflected photon from the soil that activated leaf to emit SIF.

#### 5.5.2.1. Understory reflectance effects on red and far-red SIF

Figure 5.6 presents the understory reflectance effects on the observed SIF in scenario I and scenario II. For scenario I, the reflected red and far-red SIF increased with the increase of understory reflectance, however, the fraction of red SIF and far-red SIF showed different results. We saw that red SIF is about half of the total observed scattered SIF. It suggested that the understory reflected red SIF and this contributed to almost three-quarters of the total scattered SIF and one-fifth of the total SIF when understory reflectance was high (understory reflectance = 0.45, Figure 5.6 (e)). Compare to the red SIF, the far-red SIF in scenario I stood at only 30% (understory reflectance = 0.45, Figure 5.6 (f)) of the total scattered SIF. It suggested that the scattered far-red SIF, was emitted mainly from the canopy, not from the understory. In scenario II, with the increasing of the understory reflectance, both red and far-red SIF was increased (Figure 5.6 (c), (d)), which showed a similar pattern. Moreover, the mean fraction of emitting SIF was rather low (Figure 5.6 (g), (h)).

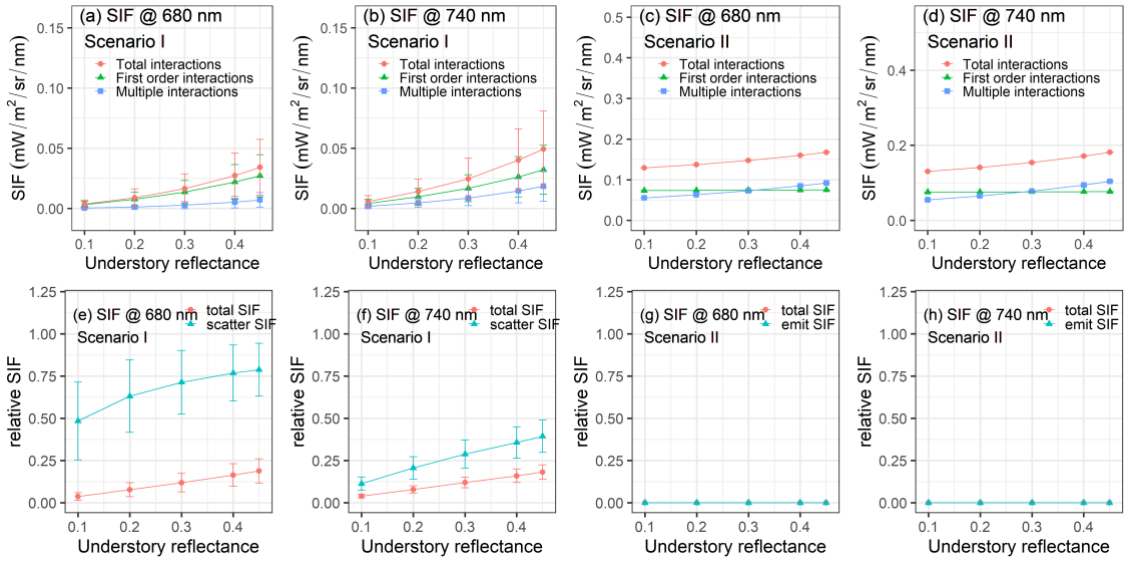


Figure 5.6. The scenario I and II's understory reflectance influence on the SIF variation (a)-(d) and its proportion of total and emit SIF (e)-(h) at 680 nm and 740 nm.

### 5.5.2.2. Fraction of vegetation cover effects on red and far-red SIF

In scenario I, both red and far-red SIF increased when FVC was less than 40% and it kept stable until it was full covered by a canopy. At the sparse FVC area, the red scattered SIF accounted for 75% of the total scattered SIF and 18% of the total SIF (FVC = 10 %, Figure 5.7 (e)). However, the fraction of red and far-red SIF declined when the FVC was high. This may because the reflected fluorescence photons were hindered by the dense canopy area. The negative correlation between the scattered SIF and the fraction of scattered SIF suggests that more scattered SIF cannot be captured by the sensor even though the scattered SIF was higher in the dense area. In scenario II, the pattern of red and far-red SIF was the same with each other. Emitted SIF increased with FVC, however, the fraction of emitting SIF was low (almost 0% of the total emitted SIF, Figure 5.7 (g), (h)). It suggested that the FVC cannot explain the variation of the emitted SIF in scenario II. The reason may be because emitted SIF and the SIF was activated by understory reflected photon, so were both raised along with the increase of FVC.

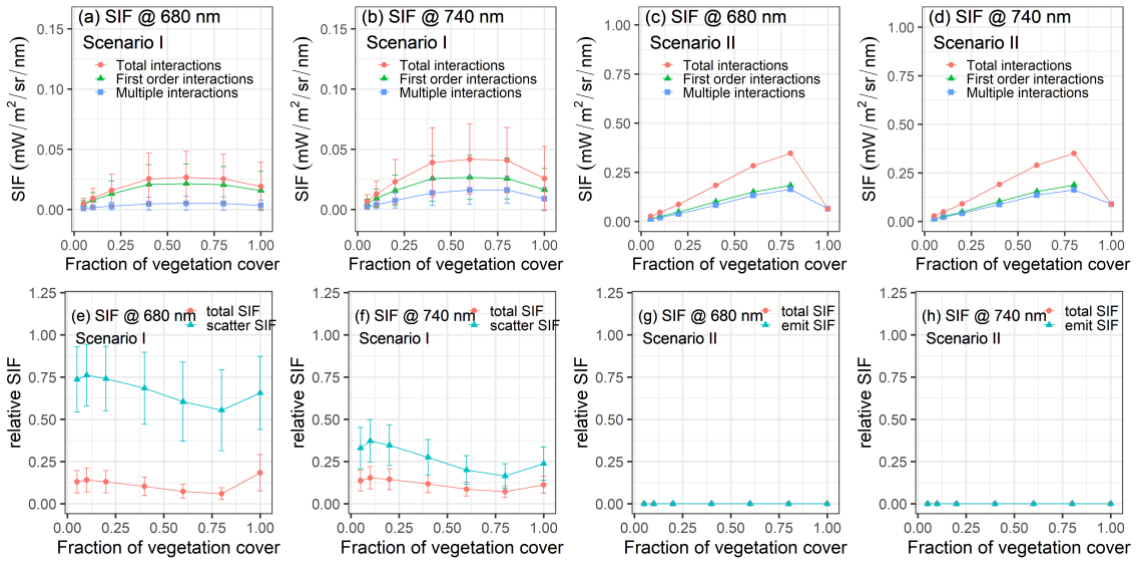


Figure 5.7. The scenario I and II's fraction of vegetation cover influenced on the SIF variation (a)-(d) and its proportion of total and emitted SIF (e)-(h) at 680 nm and 740 nm.

### 5.5.2.3. Leaf density effects on red and far-red SIF

Figure 5.8 (a)-(b), (e)-(f) presents how leaf density effects red and far-red SIF in scenario I. It can be seen that SIF increased slightly until leaf density reached 60%. The almost flat line of the portion of scattering SIF suggests the scattered SIF was reflected from the understory and the scattered SIF at the canopy both varied with the leaf density. In scenario II, the emitting SIF were affected by photons reflected from understory and presented the convex shape (Figure 5.8 (c)-(d)). When leaf density was less than 40%, the SIF showed a positive correlation with the leaf density, however, the pattern displayed a negative trend when leaf density exceeded 50%. We noted that the fraction of emitting SIF in scenario II showed an upward trend with the more dense leaf canopies (Figure 5.8 (h), (g)). It suggested that emitted SIF from canopy primarily contributed to the total emitted SIF in low FVC.

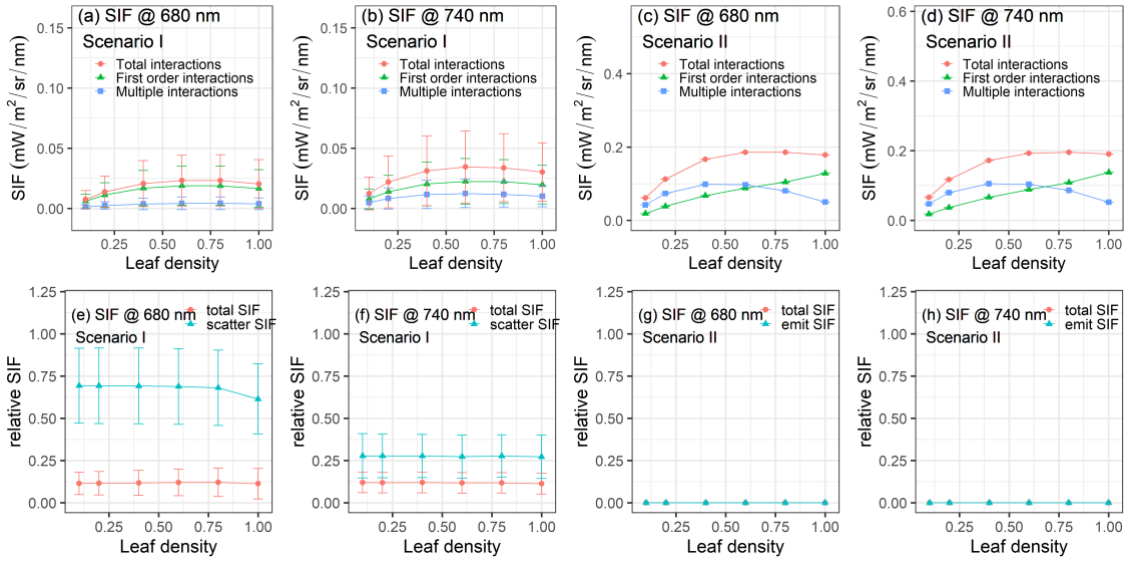


Figure 5.8. The scenario I and II's leaf density influenced on the SIF variation (a)-(d) and its proportion of total and emitting SIF (e)-(h) at 680 nm and 740 nm.

### 5.5.2.4. Leaf chlorophyll total content effects red and far-red SIF

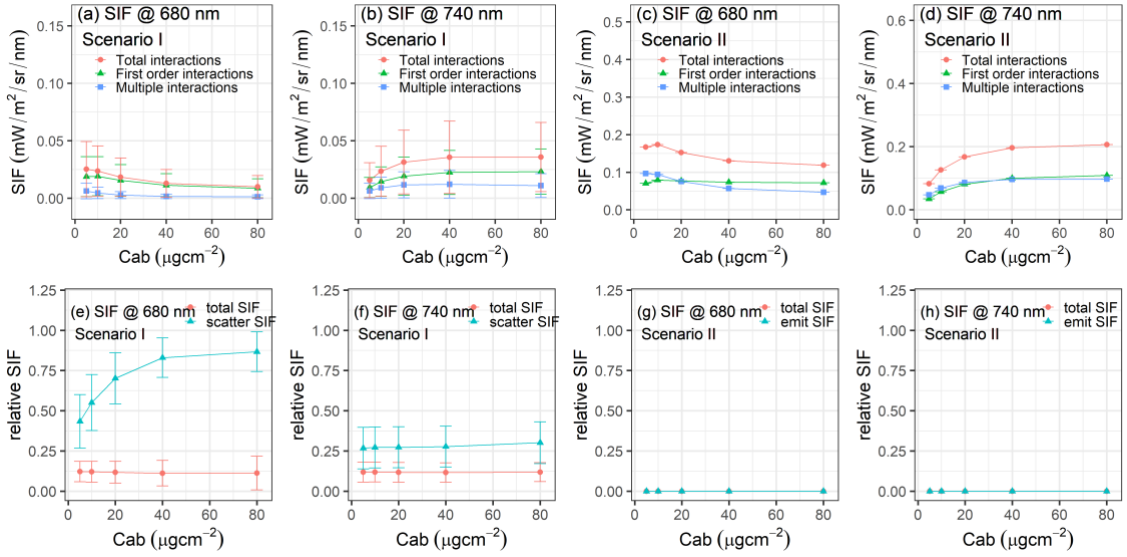


Figure 5.9. Scenario I and II's total chlorophyll content influence on the SIF variation (a)-(d) and its proportion of total and emitted SIF (e)-(h) at 680 nm and 740 nm.

Red SIF and far-red SIF presented different patterns with the variation of Cab (Figure 5.9). The red SIF decreased with the growth of the Cab. The fraction of scattered red SIF reached almost 80% of the total scattered SIF (Figure 5.9 (e)), but it still accounted for less of the total SIF. This positive pattern cannot be seen for far-red SIF. Far-red SIF stopped increasing when Cab reached 40 μgcm-2. Moreover, the fraction of scattered far-

red SIF kept at 26 percent and 18 percent for the total SIF in scenario I (Figure 5.9 (f)). In scenario II, the pattern of red and far-red emitted SIF was similar (Figure 5.9 (c), (d)).

### 5.5.3. Canopy layer's properties affect SIF at the scenario I and II

In this section, we examined how overstory properties coupled with FVC impacts on the SIF variations in the scenario I and II.

#### 5.5.3.1. Leaf density effects on red and far-red SIF

Figure 5.10 shows that leaf density did not effectively influence SIF until leaf density reached 40%. In general, the higher the leaf density and understory reflectance were, the higher SIF value was in scenario I for red SIF (Figure 5.10). Compared to scenario I, SIF variation in scenario II was higher when leaf density was equal to 0.4 $m^2/m^2$ but dropped when leaf density was equal to 1 $m^2/m^2$ because at higher FVC, fewer photons could reach the understory. Also, the understory reflectance is the efficiency factor that affect SIF in various conditions.

We note the far-red SIF in the scenario I was higher than red SIF with different conditions. This might be caused by the EF-Matrix. With the same conditions, the far-red SIF would be higher than red SIF. When leaf density and FVC reached the maximum, the SIF increased to its peak (SIF = 0.75 $mW/m^2/sr/nm$) in scenario I (Figure 5.12 (f)), but for scenario II, the maximum SIF (SIF = 0.3 $mW/m^2/sr/nm$) appeared when the leaf density equalled 0.4 $m^2/m^2$ and FVC equalled 0.8 (Figure 5.12 (c)).

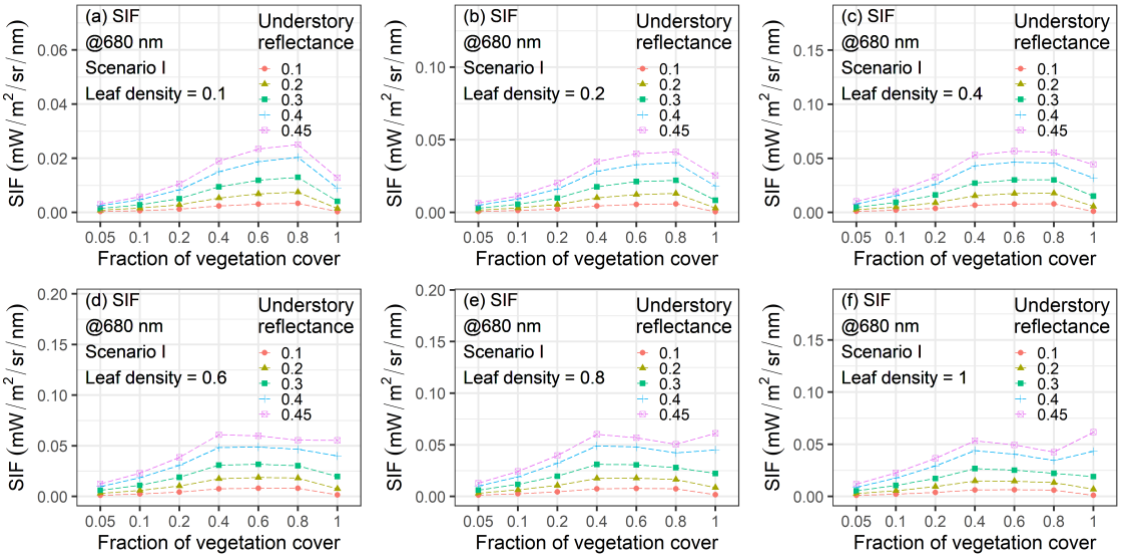


Figure 5.10. Variations of Red SIF as influenced by FVC, understory reflectance, and leaf density in scenario I. The points represent the average SIF value of given conditions.

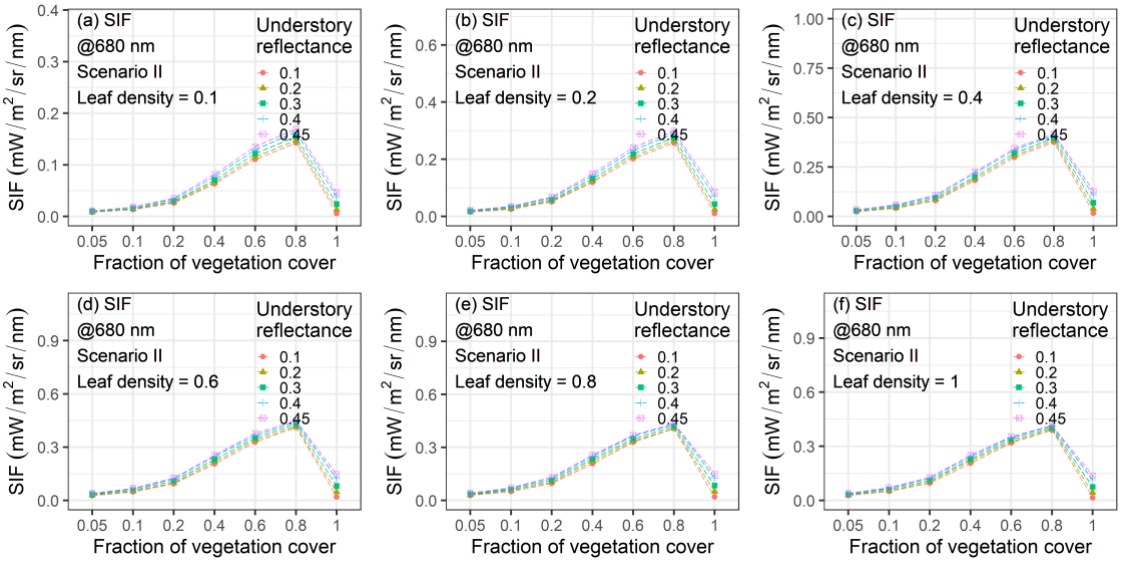


Figure 5.11. Variations of Red SIF as influenced by FVC, understory reflectance and leaf density in scenario II. The points represent the average SIF value of given conditions.

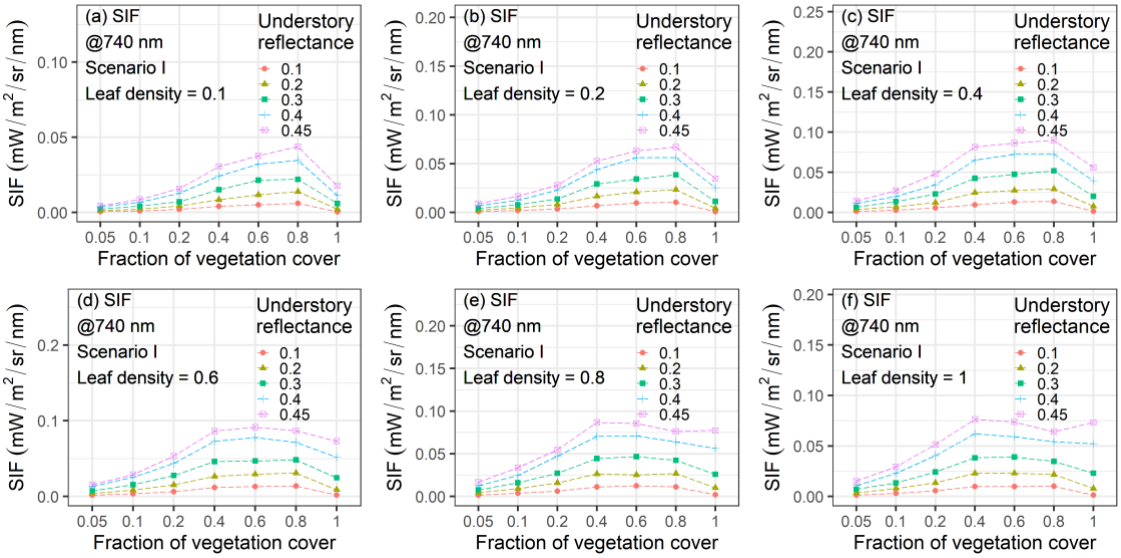


Figure 5.12. Variations of far-red SIF was influenced by FVC, understory reflectance, and leaf density in scenario I. The points represent the average SIF value of given conditions.

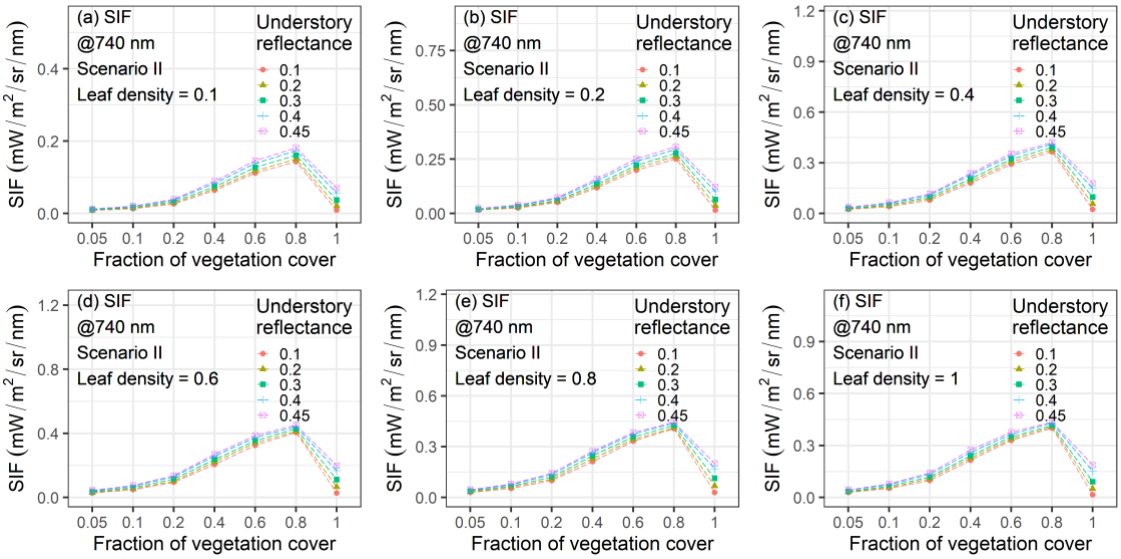


Figure 5.13. Variations of far-red SIF was influenced by FVC, understory reflectance and leaf density in scenario II. The points represent the average SIF value of given conditions.

### 5.5.3.2. Cab effects on red and far-red SIF

Figure 5.14 and Figure 5.15 clearly show that red SIF decreased with the increase of Cab in both scenarios I and II. It was caused by the negative correlation between red SIF and chlorophyll content. We can see that the red SIF reached its peak (SIF = 0.06 mW/m2/sr/nm) when understory reflectance was equal to 0.45, Cab equal to 5 µgcm-2 and FVC equal to 0.6 in scenario I (Figure 5.14 (a)). Similarly, the maximum of red SIF in

scenario II was 0.24 mW/m2/sr/nm with understory reflectance equal to 0.1, Cab equal to 20 µgcm-2 and FVC equal to 0.4 (Figure 5.14 (a)).

In regard to the far-red SIF, it did not increase under the variation of Cab in both scenarios I and II. When Cab exceeded 40 µgcm-2, far-red SIF stopped responding to the increasing of Cab. Scenario I's Far-red SIF reached the maximum (SIF = 0.1 mW/m2/sr/nm) when Cab was equal to 80 µgcm-2, understory reflectance equal to 0.45 and FVC equal to 0.8 (Figure 5.16 (e)). The maximum of far-red SIF in scenario II was 0.0005 mW/m2/sr/nm when understory reflectance was equal to 0.1, Cab equal to 20 µgcm-2 and FVC equal to 0.4 (Figure 5.16 (e)).

In summary, the relationship between SIF (scenario I and II), leaf density and FVC was not linear, however, red SIF negatively correlated with Cab, and far-red positively correlated with Cab when Cab was less than 40 µgcm-2.

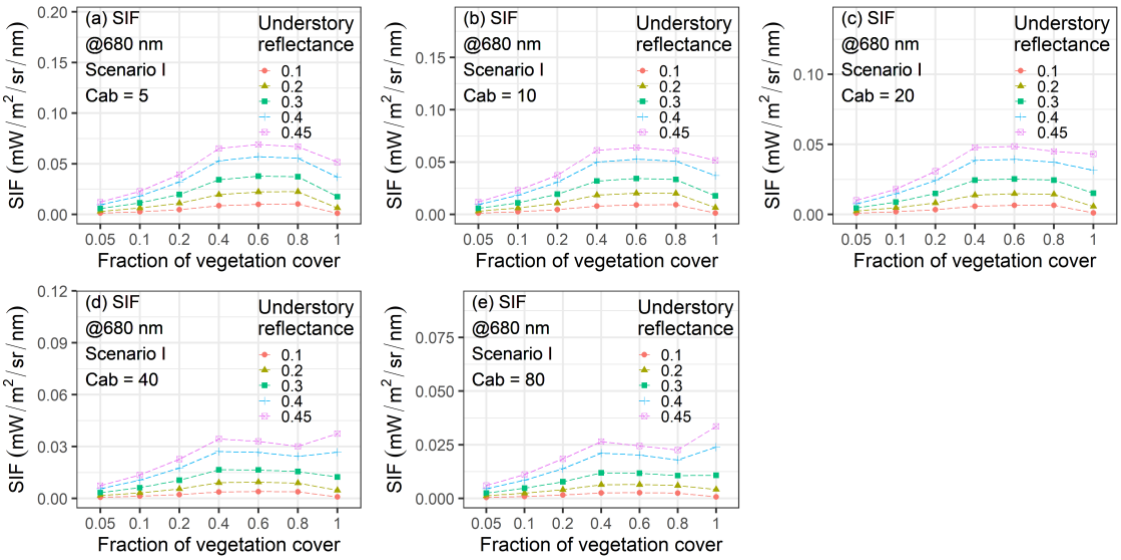


Figure 5.14. Variations of Red SIF was influenced by FVC, understory reflectance and total chlorophyll content in scenario I. The points represent the average SIF value of given conditions.

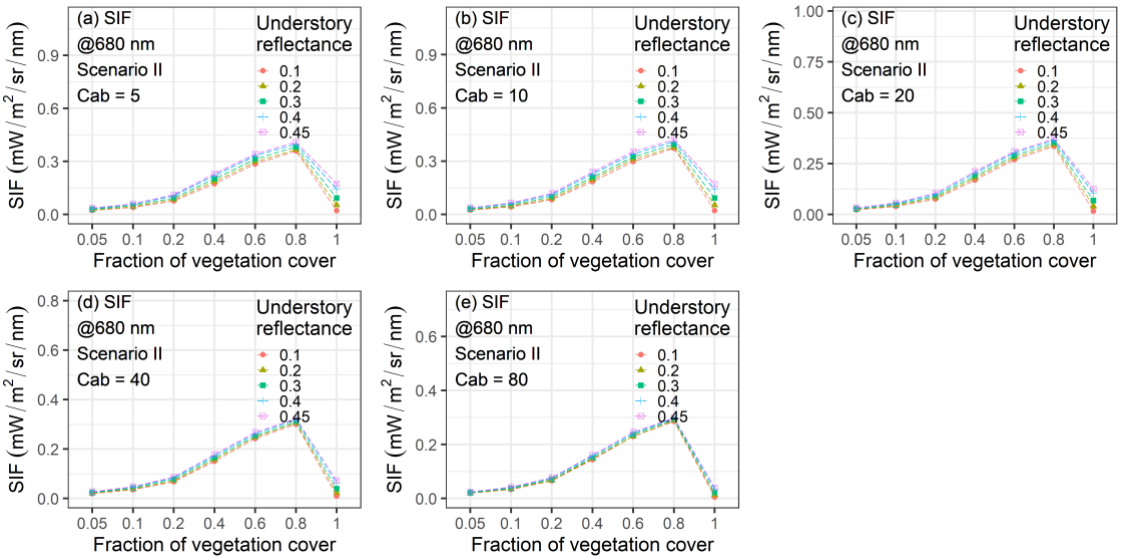


Figure 5.15. Variations of Red SIF as influenced by FVC, understory reflectance and total chlorophyll content in scenario II. The points represent the average SIF value of given conditions.

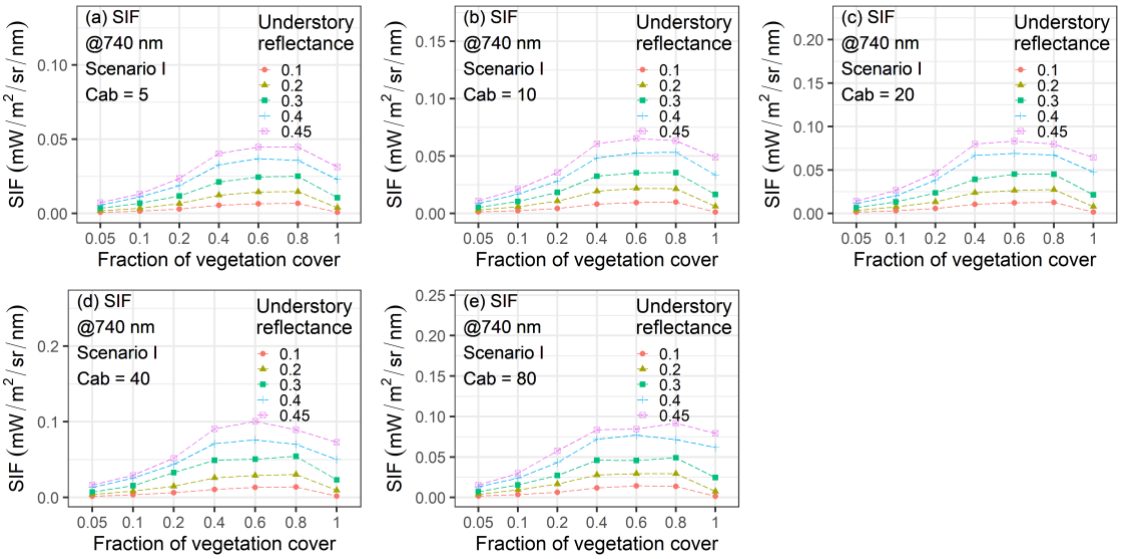


Figure 5.16. Variations of far-red SIF as influenced by FVC, understory reflectance and total chlorophyll content in scenario I. The points represent the average SIF value of given conditions.

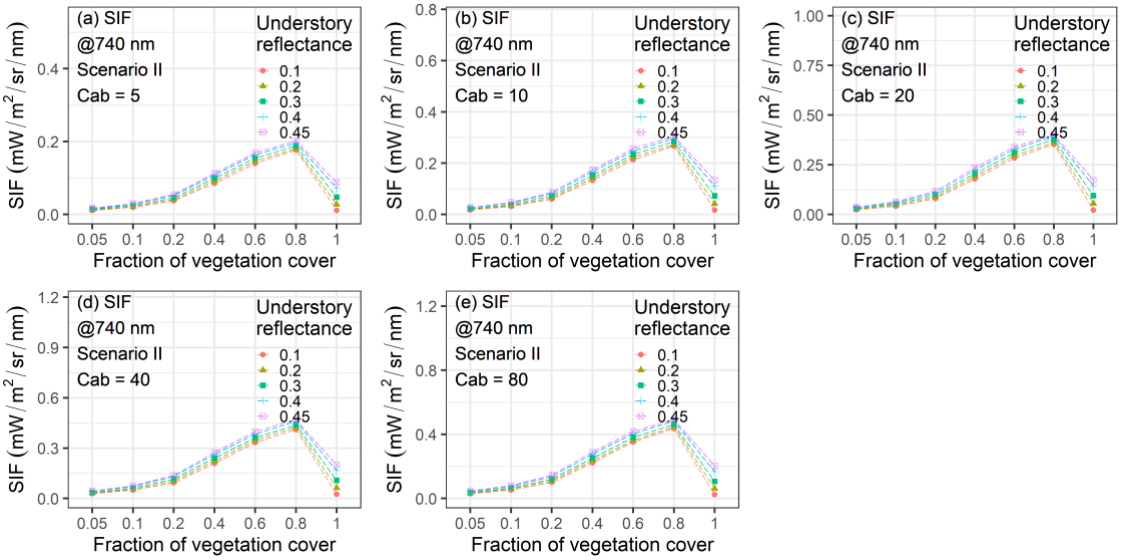


Figure 5.17. Variations of far-red SIF as influenced by FVC, understory reflectance and total chlorophyll content in scenario II. The points represent the average SIF value of given conditions.

### 5.5.4. Regression model for SIF and vegetation structures

Table 5.2 reports the correlation between SIF (total SIF of two scenarios in red and far-red region) and scenario factors. There were no existing linear relationships between SIF: Cab, SIF: FVC, SIF: $\rho_u$ and SIF:$d_{leaf}$ for those scenarios. We noted that the leaf properties and canopy structure could not explain the variation of SIF in scenarios I and II. The maximum $R^2$ of red and far-red SIF appeared ($R^2$ = 0.45 and 0.42, respectively) when considering all factors (FVC, $d_{leaf}$, $\rho_u$, Cab and N). The coefficient of determination decreased with the removal of correlation factors. The $R^2$ is higher for far-red SIF than red SIF. Moreover, the weakest correlation was SIF and leaf density ($R^2$ = 0.03 and 0.03 for red and far-red SIF, respectively), which suggested that leaf density does not affect these two scenarios.

The relative importance (RI) of each factor is shown in Figure 5.18. $\rho_u$ was the most significant factor for the summary of scenario I and II (RI = 64.56% and 72.11% for red SIF and far-red SIF, respectively). This suggested FVC could mostly explain how SIF was affected by the underground layer. The RIs of $d_{leaf}$ and N were less than 2%, which indicated that they contribute less. However, $\rho_u$ is still the most critical factor (RI = 64.7% and 72.42% for red and far-red SIF, respectively) in the scenario I group. Because the SIF was mainly reflected by the understory layer in this group, hence the close relationship

between understory reflectance and observed SIF from the understory increased the importance of $\rho_u$. In the scenario II group, FVC controlled the how many photons could be reflected from the canopy layer, which led to the high RI (20.42%, 19.59% for red and far-red SIF, respectively.).

Table 5.2. The regression model for SIF and canopy structures and understory properties. X indicates red SIF or far-red SIF. SIF was the total of scenario I and II. All the p-value was less than 0.01.

| Relation | Red SIF | Far-red SIF |
|---|---|---|
| | $R_2$ | $R_2$ |
| X + Cab | 0.1 | 0.05 |
| X + Cab + N | 0.11 | 0.05 |
| X + FVC | 0.02 | 0.04 |
| X + $\rho_u$ | 0.29 | 0.3 |
| X + $d_{leaf}$ | 0.03 | 0.03 |
| X + FVC + $d_{leaf}$ | 0.05 | 0.07 |
| X + FVC + $\rho_u$ | 0.31 | 0.35 |
| X + FVC + $\rho_u$ + $d_{leaf}$ | 0.35 | 0.38 |
| X + FVC + $d_{leaf}$ + Cab | 0.15 | 0.12 |
| X + FVC + $d_{leaf}$ + Cab + N | 0.16 | 0.12 |
| X + FVC + $\rho_u$ + $d_{leaf}$ + Cab + N | 0.45 | 0.42 |

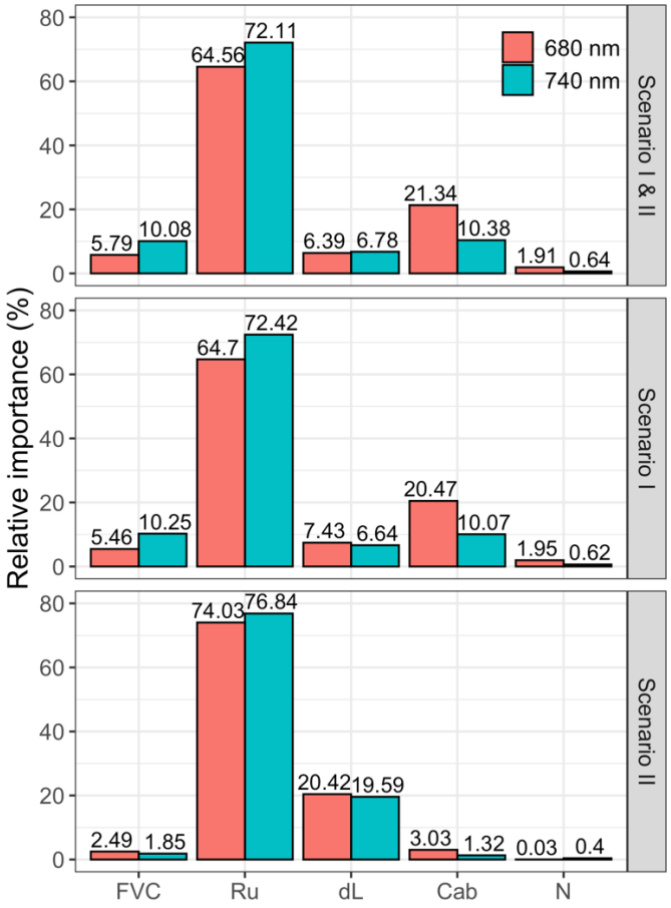


Figure 5.18. Relative importance analysis for Scenarios I and II

## 5.6. Discussion

### 5.6.1. Scattering SIF and soil SIF

The ratio of scattering SIF and emitting SIF has been studied by field measurements and model simulations (Yang & Van Der Tol 2018; Zeng et al. 2019). Yang used the SCOPE model to determine that there was an existing relation between reflectance and the ratio of scattering of SIF (Yang & Van Der Tol 2018). In simulations, he assumed the understory did not reflect any photons, however, our studies showed the contribution from understory SIF ($SIF_{SI}$ and $SIF_{SII}$) could not be ignored as it accounted for almost 50% of the total observed SIF. Also, many more photons can be reflected from the understory due to the low light interceptions and sparse leaf distribution. Hence, Yang's study would be suitable for a mature forest but might underestimate scattering SIF in sparse vegetation areas, such as savanna and young forest with the low FVC and light interception. The ratio of scattering SIF needs further field measurements to validate.

### 5.6.2. Soil effects in savanna

SIF is highly correlated with GPP in various vegetation functional types, including evergreen broadleaf forest, deciduous broadleaf forest and cropland. However, that relationship is poor in central Australia (Alice Springs and Ti Tree East). Based on the previous study, the determination of coefficients are only 0.22 and 0.39 for OCO-2 and GOME-2 SIF with monthly eddy covariance GPP, respectively (Wang et al. 2019). However, MODIS EVI presented a better $R_2$ than SIF ($R_2$ = 0.49). In the central savanna area of Australia, the average Cab was almost 29±4$\mu gcm^{-2}$, FVC is 14±9%. The $d_{leaf}$ was assumed to be at 60% in the wet season and 20% in the dry season. Dry soil has high reflectance (0.3), but the wet soil has low reflectance (0.12) (see Chapter 3).

In wet seasons, the understory SIF reflectance in far-red region is higher than in dry seasons due to the more fluorescence is emitted by the larger vegetation area than the dry season (Walther et al. 2019). High understory reflectance leads to more SIF being reflected in the dry season. However, the less emission of the fluorescence during the dry season weakens the affection that higher reflectance of the dry soil. Based on scenario I, the high understory reflectance coupled with low FVC contributes to the large proportion of reflected SIF from the understory and total observed SIF (Figure 5.7 (e)). With the increase of SIF radiance from the understory, the correlation between SIF and GPP would be higher as expected.

In dry seasons, the understory reflectance is lower than in the wet seasons, and leaf density is low as well, hence, the light can easily penetrate the canopy layer and reach the ground because of the low light interception. Vegetation growth is low during the dry season and the Cab is lower than 20 $\mu gcm^{-2}$ (see Chapter 3) however, the low interception would result in a higher escape ratio of fluorescence photons and the low understory reflectance would weaken the reflected fluorescence photons, hence, the observed fluorescence is less in scenario I (20% far-red SIF was from the scenario I). Additionally, fewer photons can be reflected to the canopy layer from the understory to activate fluorescence photons (based on scenario II), therefore, the weak fluorescence would become weaker in the dry season, hence, the weak relationship between SIF and GPP is caused by the understory reflectance and FVC.

### 5.6.3. Understory reflection effects in mature forest

Based on previous studies, SIF is highly correlated with GPP in mature forest, including evergreen broadleaf forest, deciduous broadleaf forest and needleleaf forest (Li et al. 2018). We checked the data from the Cumberland Plains site, located in eastern Australia (AU-CUM). The vegetation type of AU-CUM is an evergreen broadleaf forest. The $R_2$ of SIF and GPP was 0.5. FVC of AU-CUM is 51.55±8.85%, Cab is 28±6 $\mu gcm_{-2}$, usually $d_{leaf}$ is more than 50% for the mature forest.

Based on AU-CUM's properties, the canopy is fully covered above the ground. It is difficult for photons to penetrate the canopy and be reflected from the underground. The ratio of $SIF_{SI}$ and total SIF is extremely low in this condition (Figure 5.7 (f)). The $SIF_{SII}$ was not affected by the FVC and even the lower position of leaf emitted $SIF_{SII}$ cannot be directly observed by the sensor due to the high clumping index and high leaf density (Köhler, Guanter, et al. 2018). The most significant difference between mature forest and savanna is that the SIF emission in the forest is much higher than from the savanna. The correlation between FVC and SIF is positive indicating that emitted SIF could be observed in mature forest and the relationship between SIF and GPP is stronger than in savanna.

There are still uncertainties for $SIF_{SI}$ and $SIF_{SII}$ in mature forest for example, if there is an existing plant on the understory layer, a certain amount of fluorescence can be activated by the photons reaching the understory. Compared to SIF from the canopy layer, SIF is weaker from the understory layer, however, based on Chapter 3 studies, it cannot be ignored. This issue will strengthen the SIF observed in mature forest, even if it is more likely to be observed as scattered SIF than emitted SIF. Currently, the understanding of SIF emission from the understory layer is still unclear, so in order to understand the contributions of SIF from the understory, further field measurements are necessary.

### 5.6.4. Applications for remote sensing

Many studies aimed to discover the total emitted SIF from the canopy by using the escape ratio ($\varphi_{esc}$ = observed SIF / total emit SIF). The far-red SIF can show a strong correlation with reflectance to estimate the $\varphi_{esc}$, but this does not hold for the red SIF. Our studies found that the red $SIF_{SI}$ accounted for 70% of the total scattering SIF under both low FVC and leaf density. Hence, we can adapt this finding in a savanna to predict the scattering

SIF, and furthermore estimate the total of the emitted red SIF. By adapting the relationship that we found in section 5.4, we can produce a global underground SIF effect calculator. This would contribute to improving the estimating GPP by SIF and minimising the errors in sparse vegetation areas. This relationship requires parameters of Cab, $d_{leaf}$, FVC and $\rho_u$. The Cab can be predicted by chlorophyll index (CVI, WDVI and $CI_{green}$) (Fernandez-Baco et al. 1998; Gitelson et al. 2005). FVC can be retrieved from the landcover data (Kottek et al. 2006; Rubel et al. 2017). The underground reflectance may be measured from the surface reflectance of non-vegetation covered satellite pixels. Lastly, the leaf density can be retrieved from the LAI data coupled with canopy height (Lalic & Mihailovic 2004).

## 5.7. Conclusion

In this study, we designed two scenarios to identify the effects on SIF from understory layers. The first was that emitted fluorescence was observed which was reflected from the understory layer, and the second is that photons reflected from understory activated leaf emitted fluorescence. We implemented a FLiES-SIF model and used the ray-tracing method to identify and calculate SIF emission and scattering effects. A database was built covering almost all realistic scenarios which contained 3150 conditions using variations of FVC, $d_{leaf}$, $\rho_u$, Cab and N. Results suggested that the $\rho_u$ is the primary critical factor that would influence the $SIF_{SI}$ and $SIF_{SII}$ in both 680 and 740 nm. Compared to red SIF, far-red SIF presented a strong correlation with the five factors. A high correlation was found between $SIF_{SI}$ and $SIF_{SII}$ with those factors ($R_2$ = 0.42 and 0.49 for red and far-red SIF, respectively). Our findings also analysed the SIF influenced by FVC and $\rho_u$ in sparse vegetation areas and mature forest and it suggested that observed SIF in sparse vegetation was much more influenced by the FVC and understory reflectance and furthermore contributes to underestimating the relationship between SIF and GPP.

# Chapter 6. Conclusions

## 6.1. Summary of key methodology and conclusions

Photosynthetic activity is key to study vegetation responses to global warming and environmental stress. SIF is a new approach that is able to estimate the vegetation photosynthetic activity, particularly when plants are impacted by environmental stress. In order to understand the relationship between SIF and GPP across multiple scales, a three-dimensional model was developed to simulate SIF at various light conditions, vegetation structure and understory reflectance. It not only provides the trend of SIF in the long-term but also identifies the sensitivity of SIF under seasonal variations of environmental factors.

In this thesis, I used SIF to interpret the photosynthetic variations for various vegetation types by using the FLiES-SIF model. I assessed the relationship between SIF and GPP for various vegetation functional types. Further, field measured SIF data was applied to validate model simulations. Biochemical parameters were derived from Sentinel-2 and Landsat surface reflectance for this study. Remotely sensed SIF data, including GOME-2 and OCO-2, were used to validate the FLiES-SIF simulation and identify variations of SIF in multiple viewing angles. LiDAR data was also used to retrieve vegetation structure for modelling.

In summary, I developed a SIF module for the FLiES model based on the FLiES original ray-tracing framework and then validated FLiES-SIF with field measured SIF data at Harvard forest from 2013 to 2014. I then applied FLiES-SIF to partition the SIF signal to tree and grass layers at three flux tower sites representing different vegetation types in Australia. In addition, I also used the FLiES-SIF model coupled with a database containing large variations of input parameters, to assess whether SIF observed at TOC was affected by understory reflectance and canopy structure. Lastly, I implemented the FLiES model to normalize the OCO-2 SIF data at various viewing angles.

### 6.1.1. The development and validation of the new three-dimensional SIF model

A SIF module for the FLiES model was developed and validated with field measured SIF at Harvard Forest. The module was based on the ray-tracing framework and the Monte Carlo method. It integrated with EF-matrix to calculate the SIF emission at the leaf scale and implemented a light adjusting model. I also applied a machine learning method, Gaussian Process Regression, to generate a model, which was used to predict the

biochemical parameters from Landsat surface reflectances. Vegetation structure was derived from the LiDAR data. I compared the field measured SIF with FLiES-SIF, SCOPE and DART model's simulations from 2013 to 2014 in sunny days and cloudy days, which presented strong and weak light conditions. Lastly, I applied FLiES-SIF to separate the emitted SIF and scattered SIF.

Our results showed (1) the trained model could predict biochemical parameters in an excellent performance, and the biochemical parameters presented the seasonality. especially, the $CI_{green}$ index showed the high correlation with predicted total chlorophyll content ($R_2$ = 0.9); (2) all simulated SIF (FLiES-SIF, SCOPE and DART) well agreed with the measured canopy SIF from 2013 to 2014, they showed an obvious seasonal trend; (3) the range of FLiES-SIF simulations better approximated the field measurements, when compared with other model simulations; (4) the linear regression showed the $R_2$ of FLiES-SIF and field measured SIF was higher than the other models ($R_2$ = 0.8, 0.76 and 0.56 for FLiES-SIF, DART and SCOPE, respectively); (5) the APAR was mostly correlated with FLiES-SIF ($R_2$ = 0.92); (6) the emitted SIF was more correlated with LUE in sunny days.

### 6.1.2. Partition SIF signal to tree and grass layers

Observations of SIF are concentrated on top-of-canopy, however, the seasonality and influence of the understory SIF is still uncertain. This lack of knowledge about seasonality changes of understory SIF may underestimate the contribution of understory vegetation species to total ecosystem carbon dynamics. Hence, in order to better represent ecosystem function and predict their response to disturbances and future climate change, it would be advantageous to partition the energy flux into overstory and understory layers, and further investigate the response of the two vegetation layers to variations of environmental factors. I aimed to use the surface reflectance of the finest spatial resolution satellite to retrieve the critical biochemical data and then used the FLiES-SIF model to partition the overstory and understory SIF.

Our results showed (1) different seasonal patterns of understory SIF existed among AU-TTE, AU-LIT and AU-CUM; (2) model simulated SIF presented a similar seasonal pattern with EVI, $GPP_{EC}$ and GOME-2 SIF; (3) the radiation and canopy cover impacted the SIF emissions from tree or grass layers; (4) overstory and understory SIF showed a strong relationship with PAR and GPP in open shrubland (AU-TTE); (5) overstory SIF

showed less variation, but understory SIF accounted for 50% of the total SIF in the wet season for tropical savanna (AU-LIT); (6) in the evergreen forest, the contribution of understory SIF to total SIF was less than the overstory SIF, and it showed a weak relationship with canopy cover. Hence, the incoming radiation is not the primary reason leading to less SIF emission. In shrubland and tropical savanna, SIF was more sensitive with canopy cover.

### 6.1.3. Normalized OCO-2 SIF by 3D SIF model

The SIF signal, which is similar to reflectance, is affected by the direction of the viewing measurement. Satellite observations also confirmed this issue: normalised GOME-2 SIF at the hot spot direction was strongly correlated with sunlit GPP. However, the coarse spatial resolution of GOME-2 data makes it challenging to validate this at the site scale. OCO-2 data provided multiple viewing directions of SIF at finer resolution. Nadir, hotspot and darkspot groups were defined and used to filter SIF observations from the OCO-2 SIF dataset. The FLiES model was applied to normalized APAR and SIF yield. I assessed the BRDF effects on relationships of SIF:GPP and SIF yield:LUE, and discussed the essential factors that impact on SIF measurements from the sunlit and sunshade crown areas.

The results showed (1) the hotspot effect was confirmed in OCO-2 SIF target observations; (2) there was a strong relationship of SIF and GPP at the hot spot direction for US-PFa, US-WCr and US-NR1 ($R_2$ = 0.95, 0.95 and 0.88, respectively), and the hot spot SIF can explain more variations in GPP than in other defined viewing groups; (3) relationships of SIF and normalised APAR, normalised $SIF_{yield}$ and LUE converge and become much closer related than in the original data ($R_2$ increased 0.08 for $SIF_{yield}$:LUE) when normalised by the FLiES model; (4) a positive relationship between $SIF_{yield}$ and LUE at both hot spot and dark spot directions, suggesting that the positive pattern for $SIF_{yield}$ and LUE exists in light-saturating or light-limiting conditions; (5) PAR and Ta were the primary contributors to SIF variations in the hot spot group and dark spot group, respectively; (6) the SWC contributed less to these three groups.

### 6.1.4. SIF signal affected by understory layer

I aimed to identify that SIF observed at the top of canopy was mostly affected by understory reflectance and vegetation structure. Many SIF studies were focused on

canopy structure and light conditions which affected SIF, but how the understory affects SIF observations has been ignored by researchers. I generated a database for FLiES-SIF model to study this issue based on two scenarios. The database covered 3150 conditions by variations of FVC, $d_{leaf}$, $\rho_u$, Cab and N.

Our results showed (1) the understory reflectance was the primary critical factor influencing $SIF_{SI}$ and $SIF_{SII}$ in both 680 and 740 nm; (2) compared to red SIF, far-red SIF presented a strong correlation with the five factors (FVC, $d_{leaf}$, $\rho_u$, Cab and N); (3) a high correlation was found for the total of $SIF_{SI}$ and $SIF_{SII}$ with those factors ($R^2$ = 0.42 and 0.49 for red and far-red SIF, respectively).

## 6.2. Research limitations and future research directions

Chapter 2 described the development and validation of a 3D SIF radiative transfer model. The model performance and robust simulation scheme would be helpful to simulating SIF for various purposes. Comparisons of 1D model and 3D model running times and complexity of parameter settings would increase the difficulty of model usability. In addition, the progress of photosynthesis is not only related to the radiation and biochemical parameters, but also to temperature, leaf level photochemical processes and meteorological impacts. Additionally, the FOV of field measurements only covered limited canopy area, while the simulations could be applied to a 30 * 30 $m^2$ area. The mismatch of spatial resolutions needs to be assessed in the future.

Chapter 3 presented the study for partitioning SIF signal to overstory and understory layers. This study would improve our understanding of how SIF variation of over- and understory layer's in sparse or dense canopy cover areas. Radiative transfer model concerns the radiation distribution, but it cannot simulate ecological flux exchanges. Hence, simulating SIF in the overstory and understory layers should concern only the local ecological environment. In the savanna, precipitation and radiation influenced plant productivity, hence, the cloud cover and diffuse radiation may affect the understory SIF emission. I noted that retrieving biochemical parameters relied on the satellite observations, so that it cannot simulate SIF in cloudy days directly. With continuing precipitation, the grass would grow rapidly and its structure would change as well, hence, if we want to know more about the changes in the understory layer, field observations should also be employed.

Chapter 4 showed the study of the relationship between SIF and GPP in various viewing directions, and I found there existed a strong relationship of SIF and GPP at the hot spot direction for US-PFa, US-WCr and US-NR1 ($R_2$ = 0.95, 0.95 and 0.88, respectively). However, there are still many uncertainties in this study. Firstly, in order to gather enough observations of OCO-2, I set a large threshold of for darkspot observation group. This added error as some observations only close to, and not exactly meeting the darkspot definition. Secondly, I did not partition the LUE for each viewing group due to the lack of an effective method for calculating the GPP at a fixed viewing direction. Hence, I only assessed the relationship for total LUE and SIF yield from each view group.

Chapter 5 presented the study for fluorescence and non-fluorescence photons from the understory affecting the SIF observations. The model simulations showed that observed SIF over sparse vegetated areas was much more influenced by the FVC and understory reflectance. During the simulation, I set no SIF emission from the understory layer, however, it has been ascertained that understory SIF cannot be ignored in savanna due to the rapid growth of grass in the wet season. Hence, this needs further measurement to monitor SIF emission from both overstory and understory in order to identify the impact of understory reflectance for various vegetation functional types.

## 6.3. Conclusions

In this thesis, a three-dimensional radiative transfer SIF model was developed and validated. I used this model to assess the relationship between SIF and plant photosynthetic activity across different spatial and temporal scales. The outcomes of this research have helped to identify SIF variations with canopy structure, light conditions and viewing angles. This thesis highlights the advantage of FLiES-SIF in capturing vegetation photosynthetic activity of ecosystems with complex canopy structures. This will significantly improve our understanding of vegetation responses to climate change.

# Chapter 7. Bibliography

Aasen, H., Van Wittenberghe, S., Medina, N.S., Damm, A., Goulas, Y., Wieneke, S., Hueni, A., Malenovský, Z., Alonso, L. & Pacheco-Labrador, J. 2019, 'Sun-induced chlorophyll fluorescence II: Review of passive measurement setups, protocols, and their application at the leaf to canopy level', *Remote Sensing*, vol. 11, no. 8, p. 927.

Alonso, L., Gómez-Chova, L., Vila-Francés, J., Amorós-López, J., Guanter, L., Calpe, J. & Moreno, J. 2008, 'Improved Fraunhofer Line Discrimination method for vegetation fluorescence quantification', *IEEE Geoscience and Remote Sensing Letters*, vol. 5, no. 4, pp. 620-4.

Alton, P., North, P. & Los, S. 2007, 'The impact of diffuse sunlight on canopy light-use efficiency, gross photosynthetic product and net ecosystem exchange in three forest biomes', *Global Change Biology*, vol. 13, no. 4, pp. 776-87.

Bailey, B.N. & Mahaffee, W.F. 2017, 'Rapid measurement of the three-dimensional distribution of leaf orientation and the leaf angle probability density function using terrestrial LiDAR scanning', *Remote Sensing of Environment*, vol. 194, pp. 63-76.

Baker, N.R. 2008, 'Chlorophyll fluorescence: a probe of photosynthesis in vivo', *Annu. Rev. Plant Biol.*, vol. 59, pp. 89-113.

Baldocchi, D., Falge, E., Gu, L., Olson, R., Hollinger, D., Running, S., Anthoni, P., Bernhofer, C., Davis, K. & Evans, R. 2001, 'FLUXNET: A new tool to study the temporal and spatial variability of ecosystem-scale carbon dioxide, water vapor, and energy flux densities', *Bulletin of the American Meteorological Society*, vol. 82, no. 11, pp. 2415-34.

Bassow, S.L. & Bazzaz, F.A. 1998, 'HOW ENVIRONMENTAL CONDITIONS AFFECT CANOPY LEAF-LEVEL PHOTOSYNTHESIS IN FOUR DECIDUOUS TREE SPECIES', *Ecology*, vol. 79, no. 8, pp. 2660-75.

Bauerle, W.L., Oren, R., Way, D.A., Qian, S.S., Stoy, P.C., Thornton, P.E., Bowden, J.D., Hoffman, F.M. & Reynolds, R.F. 2012, 'Photoperiodic regulation of the seasonal pattern of photosynthetic capacity and the implications for carbon cycling', *Proceedings of the National Academy of Sciences*, vol. 109, no. 22, pp. 8612-7.

Beer, C., Reichstein, M., Tomelleri, E., Ciais, P., Jung, M., Carvalhais, N., Rödenbeck, C., Arain, M.A., Baldocchi, D. & Bonan, G.B. 2010, 'Terrestrial gross carbon

dioxide uptake: global distribution and covariation with climate', *Science*, vol. 329, no. 5993, pp. 834-8.

Beringer, J., Hutley, L., Tapper, N., Coutts, A., Kerley, A. & O'grady, A. 2003, 'Fire impacts on surface heat, moisture and carbon fluxes from a tropical savanna in northern Australia', *International Journal of Wildland Fire*, vol. 12, no. 4, pp. 333-40.

Beringer, J., Hutley, L.B., Abramson, D., Arndt, S.K., Briggs, P., Bristow, M., Canadell, J.G., Cernusak, L.A., Eamus, D. & Edwards, A.C. 2015, 'Fire in Australian savannas: from leaf to landscape', *Global change biology*, vol. 21, no. 1, pp. 62-81.

Beringer, J., Hutley, L.B., Tapper, N.J. & Cernusak, L.A. 2007, 'Savanna fires and their impact on net ecosystem productivity in North Australia', *Global Change Biology*, vol. 13, no. 5, pp. 990-1004.

Berry, J. 2018, '3.10 Solar Induced Chlorophyll Fluorescence: Origins, Relation to Photosynthesis and Retrieval'.

Braswell, B., Schimel, D.S., Linder, E. & Moore, B. 1997, 'The response of global terrestrial ecosystems to interannual temperature variability', *Science*, vol. 278, no. 5339, pp. 870-3.

Burns, S., Maclean, G., Blanken, P., Oncley, S., Semmer, S. & Monson, R. 2016, 'The Niwot Ridge Subalpine Forest US-NR1 AmeriFlux site–Part 1: Data acquisition and site record-keeping, 2016', *Geoscientific Instrumentation, Methods and Data Systems*, vol. 5, p. 451.

Calderón, R., Navas-Cortés, J.A., Lucena, C. & Zarco-Tejada, P.J. 2013, 'High-resolution airborne hyperspectral and thermal imagery for early detection of Verticillium wilt of olive using fluorescence, temperature and narrow-band spectral indices', *Remote Sensing of Environment*, vol. 139, pp. 231-45.

Camps-Valls, G., Verrelst, J., Munoz-Mari, J., Laparra, V., Mateo-Jimenez, F. & Gomez-Dans, J. 2016, 'A survey on gaussian processes for earth-observation data analysis: A comprehensive investigation', *IEEE Geoscience and Remote Sensing Magazine*, vol. 4, no. 2, pp. 58-78.

Cao, M. & Woodward, F.I. 1998, 'Dynamic responses of terrestrial ecosystem carbon cycling to global climate change', *Nature*, vol. 393, no. 6682, p. 249.

Chen, J.M., Menges, C.H. & Leblanc, S.G. 2005, 'Global mapping of foliage clumping index using multi-angular satellite data', *Remote Sensing of Environment*, vol. 97, no. 4, pp. 447-57.

Chevan, A. & Sutherland, M. 1991, 'Hierarchical partitioning', *The American Statistician*, vol. 45, no. 2, pp. 90-6.

Cogliati, S., Rossini, M., Julitta, T., Meroni, M., Schickling, A., Burkart, A., Pinto, F., Rascher, U. & Colombo, R. 2015, 'Continuous and long-term measurements of reflectance and sun-induced chlorophyll fluorescence by using novel automated field spectroscopy systems', *Remote Sensing of Environment*, vol. 164, pp. 270-81.

Cook, B.D., Davis, K.J., Wang, W., Desai, A., Berger, B.W., Teclaw, R.M., Martin, J.G., Bolstad, P.V., Bakwin, P.S. & Yi, C. 2004, 'Carbon exchange and venting anomalies in an upland deciduous forest in northern Wisconsin, USA', *Agricultural and Forest Meteorology*, vol. 126, no. 3-4, pp. 271-95.

Damm, A., Guanter, L., Paul-Limoges, E., Van der Tol, C., Hueni, A., Buchmann, N., Eugster, W., Ammann, C. & Schaepman, M. 2015a, 'Far-red sun-induced chlorophyll fluorescence shows ecosystem-specific relationships to gross primary production: An assessment based on observational and modeling approaches', *Remote Sensing of Environment*, vol. 166, pp. 91-105.

Damm, A., Guanter, L., Paul-Limoges, E., van der Tol, C., Hueni, A., Buchmann, N., Eugster, W., Ammann, C. & Schaepman, M.E. 2015b, 'Far-red sun-induced chlorophyll fluorescence shows ecosystem-specific relationships to gross primary production: An assessment based on observational and modeling approaches', *Remote Sensing of Environment*, vol. 166, pp. 91-105.

Daumard, F., Goulas, Y., Champagne, S., Fournier, A., Ounis, A., Olioso, A. & Moya, I. 2012, 'Continuous monitoring of canopy level sun-induced chlorophyll fluorescence during the growth of a sorghum field', *IEEE Transactions on Geoscience and Remote Sensing*, vol. 50, no. 11, pp. 4292-300.

Demmig, B. & Björkman, O. 1987, 'Comparison of the effect of excessive light on chlorophyll fluorescence (77K) and photon yield of O 2 evolution in leaves of higher plants', *Planta*, vol. 171, no. 2, pp. 171-84.

Dixon, R.K., Solomon, A., Brown, S., Houghton, R., Trexier, M. & Wisniewski, J. 1994, 'Carbon pools and flux of global forest ecosystems', *Science*, vol. 263, no. 5144, pp. 185-90.

Dobrowski, S.Z., Pushnik, J.C., Zarco-Tejada, P.J. & Ustin, S.L. 2005, 'Simple reflectance indices track heat and water stress-induced changes in steady-state chlorophyll fluorescence at the canopy scale', *Remote Sensing of Environment*, vol. 97, no. 3, pp. 403-14.

Dong, K., Jiang, H., Sun, R. & Dong, X. 2019, 'Driving forces and mitigation potential of global CO2 emissions from 1980 through 2030: Evidence from countries with different income levels', *Science of The Total Environment*, vol. 649, pp. 335-43.

DRAGONI, D., SCHMID, H.P., WAYSON, C.A., POTTER, H., GRIMMOND, C.S.B. & RANDOLPH, J.C. 2011, 'Evidence of increased net ecosystem productivity associated with a longer vegetated season in a deciduous forest in south-central Indiana, USA', *Global Change Biology*, vol. 17, no. 2, pp. 886-97.

Drolet, G., Middleton, E., Huemmrich, K., Hall, F., Amiro, B., Barr, A., Black, T., McCaughey, J. & Margolis, H. 2008, 'Regional mapping of gross light-use efficiency using MODIS spectral indices', *Remote Sensing of Environment*, vol. 112, no. 6, pp. 3064-78.

Drusch, M., Del Bello, U., Carlier, S., Colin, O., Fernandez, V., Gascon, F., Hoersch, B., Isola, C., Laberinti, P. & Martimort, P. 2012, 'Sentinel-2: ESA's optical high-resolution mission for GMES operational services', *Remote sensing of Environment*, vol. 120, pp. 25-36.

Dubayah, R.O. & Drake, J.B. 2000, 'Lidar remote sensing for forestry', *Journal of Forestry*, vol. 98, no. 6, pp. 44-6.

Eamus, D., Cleverly, J., Boulain, N., Grant, N., Faux, R. & Villalobos-Vega, R. 2013, 'Carbon and water fluxes in an arid-zone Acacia savanna woodland: An analyses of seasonal patterns and responses to rainfall events', *Agricultural and Forest Meteorology*, vol. 182, pp. 225-38.

Emmel, P. 2000, *Nouvelle formulation du modèle de Kubelka et Munk avec application aux encres fluorescentes*.

Emmel, P. & Hersch, R.D. 1998, 'Spectral colour prediction model for a transparent fluorescent ink on paper', *Color and Imaging Conference*, vol. 1998, Society for Imaging Science and Technology, pp. 116-22.

Engel, G.S., Calhoun, T.R., Read, E.L., Ahn, T.-K., Mančal, T., Cheng, Y.-C., Blankenship, R.E. & Fleming, G.R. 2007, 'Evidence for wavelike energy transfer through quantum coherence in photosynthetic systems', *Nature*, vol. 446, p. 782.

Falkowski, P., Scholes, R., Boyle, E., Canadell, J., Canfield, D., Elser, J., Gruber, N., Hibbard, K., Högberg, P. & Linder, S. 2000, 'The global carbon cycle: a test of our knowledge of earth as a system', *science*, vol. 290, no. 5490, pp. 291-6.

Fay, P.A., Kaufman, D.M., Nippert, J.B., Carlisle, J.D. & Harper, C.W. 2008, 'Changes in grassland ecosystem function due to extreme rainfall events: implications for responses to climate change', *Global Change Biology*, vol. 14, no. 7, pp. 1600-8.

Feret, J.-B., François, C., Asner, G.P., Gitelson, A.A., Martin, R.E., Bidel, L.P., Ustin, S.L., Le Maire, G. & Jacquemoud, S. 2008, 'PROSPECT-4 and 5: Advances in the leaf optical properties model separating photosynthetic pigments', *Remote sensing of environment*, vol. 112, no. 6, pp. 3030-43.

Fernandez-Baco, L., Figueroa, M., Luque, T. & Davy, A. 1998, 'Diurnal and seasonal variations in chlorophyll a fluorescence in two Mediterranean-grassland species under field conditions', *Photosynthetica*, vol. 35, no. 4, pp. 535-44.

Frank, D., Reichstein, M., Bahn, M., Thonicke, K., Frank, D., Mahecha, M.D., Smith, P., Van der Velde, M., Vicca, S. & Babst, F. 2015, 'Effects of climate extremes on the terrestrial carbon cycle: concepts, processes and potential future impacts', *Global Change Biology*, vol. 21, no. 8, pp. 2861-80.

Frankenberg, C. & Berry, J. 2018, 'Solar induced chlorophyll fluorescence: origins, relation to photosynthesis and retrieval'.

Frankenberg, C., Fisher, J.B., Worden, J., Badgley, G., Saatchi, S.S., Lee, J.E., Toon, G.C., Butz, A., Jung, M. & Kuze, A. 2011, 'New global observations of the terrestrial carbon cycle from GOSAT: Patterns of plant fluorescence with gross primary productivity', *Geophysical Research Letters*, vol. 38, no. 17.

Frankenberg, C., Köhler, P., Magney, T.S., Geier, S., Lawson, P., Schwochert, M., McDuffie, J., Drewry, D.T., Pavlick, R. & Kuhnert, A. 2018, 'The Chlorophyll Fluorescence Imaging Spectrometer (CFIS), mapping far red fluorescence from aircraft', *Remote Sensing of Environment*, vol. 217, pp. 523-36.

Frankenberg, C., O'Dell, C., Berry, J., Guanter, L., Joiner, J., Köhler, P., Pollock, R. & Taylor, T.E. 2014, 'Prospects for chlorophyll fluorescence remote sensing from the Orbiting Carbon Observatory-2', *Remote Sensing of Environment*, vol. 147, pp. 1-12.

Frankenberg, C., Pollock, R., Lee, R., Rosenberg, R., Blavier, J., Crisp, D., O'Dell, C., Osterman, G., Roehl, C. & Wennberg, P. 2015, 'The Orbiting Carbon Observatory

(OCO-2): spectrometer performance evaluation using pre-launch direct sun measurements', *Atmospheric Measurement Techniques*, vol. 8, no. 1, p. 301.

Gamon, J.A., Huemmrich, K.F., Wong, C.Y., Ensminger, I., Garrity, S., Hollinger, D.Y., Noormets, A. & Peñuelas, J. 2016, 'A remotely sensed pigment index reveals photosynthetic phenology in evergreen conifers', *Proceedings of the National Academy of Sciences*, vol. 113, no. 46, pp. 13087-92.

Ganapol, B.D., Johnson, L.F., Hammer, P.D., Hlavka, C.A. & Peterson, D.L. 1998, 'LEAFMOD: a new within-leaf radiative transfer model', *Remote Sensing of Environment*, vol. 63, no. 2, pp. 182-93.

Garbulsky, M.F., Peñuelas, J., Gamon, J., Inoue, Y. & Filella, I. 2011, 'The photochemical reflectance index (PRI) and the remote sensing of leaf, canopy and ecosystem radiation use efficiencies: A review and meta-analysis', *Remote Sensing of Environment*, vol. 115, no. 2, pp. 281-97.

Garzonio, R., Di Mauro, B., Colombo, R. & Cogliati, S. 2017, 'Surface Reflectance and Sun-Induced Fluorescence Spectroscopy Measurements Using a Small Hyperspectral UAS', *Remote Sensing*, vol. 9, no. 5, p. 472.

Gastellu-Etchegorry, J.-P., Demarez, V., Pinel, V. & Zagolski, F. 1996, 'Modeling radiative transfer in heterogeneous 3-D vegetation canopies', *Remote sensing of environment*, vol. 58, no. 2, pp. 131-56.

Gastellu-Etchegorry, J.-P., Lauret, N., Yin, T., Landier, L., Kallel, A., Malenovský, Z., Al Bitar, A., Aval, J., Benhmida, S. & Qi, J. 2017, 'DART: Recent advances in remote sensing data modeling with atmosphere, polarization, and chlorophyll fluorescence', *IEEE Journal of Selected Topics in Applied Earth Observations and Remote Sensing*, vol. 10, no. 6, pp. 2640-9.

Gitelson, A.A., Vina, A., Ciganda, V., Rundquist, D.C. & Arkebauer, T.J. 2005, 'Remote estimation of canopy chlorophyll content in crops', *Geophysical Research Letters*, vol. 32, no. 8.

Grömping, U. 2006, 'Relative importance for linear regression in R: the package relaimpo', *Journal of statistical software*, vol. 17, no. 1, pp. 1-27.

Gu, L., Baldocchi, D.D., Wofsy, S.C., Munger, J.W., Michalsky, J.J., Urbanski, S.P. & Boden, T.A. 2003, 'Response of a deciduous forest to the Mount Pinatubo eruption: Enhanced photosynthesis', *Science*, vol. 299, no. 5615, pp. 2035-8.

Gu, L., Han, J., Wood, J.D., Chang, C.Y.-Y. & Sun, Y. 2019a, 'Sun-induced Chl fluorescence and its importance for biophysical modeling of photosynthesis based on light reactions', *New Phytologist*, vol. 0, no. 0.

Gu, L., Han, J., Wood, J.D., Chang, C.Y.Y. & Sun, Y. 2019b, 'Sun - induced Chl fluorescence and its importance for biophysical modeling of photosynthesis based on light reactions', *New Phytologist*, p. 1.

Guan, K., Miao, G., Suyker, A., Yelu, Z., Yang, X., Wu, G., Ryu, Y., Dechant, B., Arkebauer, T.J., Walter-Shea, E.A., Gamon, J.A., Hmimina, G., Avenson, T., Moore, R. & Kim, H. 2018, 'Structural and Physiological Effects on the Relationship between Solar-Induced Fluorescence and Gross Primary Production: A Comparison Study between Nadir and Hemispherical Fluorescence Observations', *American Geophysical Union, Fall Meeting 2018*.

Guan, K., Pan, M., Li, H., Wolf, A., Wu, J., Medvigy, D., Caylor, K.K., Sheffield, J., Wood, E.F. & Malhi, Y. 2015, 'Photosynthetic seasonality of global tropical forests constrained by hydroclimate', *Nature Geoscience*, vol. 8, no. 4, p. 284.

Guanter, L., Aben, I., Tol, P., Krijger, J., Hollstein, A., Köhler, P., Damm, A., Joiner, J., Frankenberg, C. & Landgraf, J. 2015, 'Potential of the TROPOspheric Monitoring Instrument (TROPOMI) onboard the Sentinel-5 Precursor for the monitoring of terrestrial chlorophyll fluorescence', *Atmospheric Measurement Techniques*, vol. 8, no. 3, pp. 1337-52.

Guanter, L., Frankenberg, C., Dudhia, A., Lewis, P.E., Gómez-Dans, J., Kuze, A., Suto, H. & Grainger, R.G. 2012, 'Retrieval and global assessment of terrestrial chlorophyll fluorescence from GOSAT space measurements', *Remote Sensing of Environment*, vol. 121, pp. 236-51.

Guanter, L., Zhang, Y., Jung, M., Joiner, J., Voigt, M., Berry, J.A., Frankenberg, C., Huete, A.R., Zarco-Tejada, P. & Lee, J.-E. 2014a, 'Global and time-resolved monitoring of crop photosynthesis with chlorophyll fluorescence', *Proceedings of the National Academy of Sciences*, vol. 111, no. 14, pp. E1327-E33.

Guanter, L., Zhang, Y., Jung, M., Joiner, J., Voigt, M., Berry, J.A., Frankenberg, C., Huete, A.R., Zarco-Tejada, P. & Lee, J.-E. 2014b, 'Global and time-resolved monitoring of crop photosynthesis with chlorophyll fluorescence', *Proceedings of the National Academy of Sciences*, p. 201320008.

Gurney, K.R., Baker, D., Rayner, P. & Denning, S. 2008, 'Interannual variations in continental - scale net carbon exchange and sensitivity to observing networks estimated from atmospheric CO2 inversions for the period 1980 to 2005', *Global Biogeochemical Cycles*, vol. 22, no. 3.

He, L., Chen, J.M., Liu, J., Mo, G. & Joiner, J. 2017, 'Angular normalization of GOME-2 Sun - induced chlorophyll fluorescence observation as a better proxy of vegetation productivity', *Geophysical Research Letters*, vol. 44, no. 11, pp. 5691-9.

Heimann, M. & Reichstein, M. 2008, 'Terrestrial ecosystem carbon dynamics and climate feedbacks', *Nature*, vol. 451, p. 289.

Hernández-Clemente, R., North, P.R., Hornero, A. & Zarco-Tejada, P.J. 2017, 'Assessing the effects of forest health on sun-induced chlorophyll fluorescence using the FluorFLIGHT 3-D radiative transfer model to account for forest structure', *Remote Sensing of Environment*, vol. 193, pp. 165-79.

Hosgood, B., Jacquemoud, S., Andreoli, G., Verdebout, J., Pedrini, G. & Schmuck, G. 1995, 'Leaf optical properties experiment 93 (LOPEX93)', *Ispra Italy'European Commission, Joint Research Centre Institute of Remote Sensing Applications*.

Hu, J., Liu, L., Guo, J., Du, S. & Liu, X. 2018, 'Upscaling Solar-Induced Chlorophyll Fluorescence from an Instantaneous to Daily Scale Gives an Improved Estimation of the Gross Primary Productivity', *Remote Sensing*, vol. 10, no. 10, p. 1663.

Huete, A., Didan, K., Miura, T., Rodriguez, E.P., Gao, X. & Ferreira, L.G. 2002, 'Overview of the radiometric and biophysical performance of the MODIS vegetation indices', *Remote sensing of environment*, vol. 83, no. 1-2, pp. 195-213.

Hutley, L., O'grady, A. & Eamus, D. 2000, 'Evapotranspiration from Eucalypt open - forest savanna of Northern Australia', *Functional Ecology*, vol. 14, no. 2, pp. 183-94.

Iermak, I., Vink, J., Bader, A.N., Wientjes, E. & van Amerongen, H. 2016, 'Visualizing heterogeneity of photosynthetic properties of plant leaves with two-photon fluorescence lifetime imaging microscopy', *Biochimica et Biophysica Acta (BBA) - Bioenergetics*, vol. 1857, no. 9, pp. 1473-8.

Jaboyedoff, M., Oppikofer, T., Abellán, A., Derron, M.-H., Loye, A., Metzger, R. & Pedrazzini, A. 2012, 'Use of LIDAR in landslide investigations: a review', *Natural hazards*, vol. 61, no. 1, pp. 5-28.

Jacquemound, S., Bidel, L., Francois, C. & Pavan, G. 2003, 'ANGERS Leaf Optical Properties Database (2003)', *Data Set. Available online: http://ecosis. org (accessed on 5 June 2018)*.

Jeong, S.-J., Schimel, D., Frankenberg, C., Drewry, D.T., Fisher, J.B., Verma, M., Berry, J.A., Lee, J.-E. & Joiner, J. 2017, 'Application of satellite solar-induced chlorophyll fluorescence to understanding large-scale variations in vegetation phenology and function over northern high latitude forests', *Remote Sensing of Environment*, vol. 190, pp. 178-87.

Jiang, C., Ryu, Y., Fang, H., Myneni, R., Claverie, M. & Zhu, Z. 2017, 'Inconsistencies of interannual variability and trends in long-term satellite leaf area index products', *Global Change Biology*, vol. 23, no. 10, pp. 4133-46.

Joiner, J., Guanter, L., Lindstrot, R., Voigt, M., Vasilkov, A., Middleton, E., Huemmrich, K., Yoshida, Y. & Frankenberg, C. 2013, 'Global monitoring of terrestrial chlorophyll fluorescence from moderate-spectral-resolution near-infrared satellite measurements: methodology, simulations, and application to GOME-2', *Atmospheric Measurement Techniques*, vol. 6, no. 10, pp. 2803-23.

Joiner, J., Yoshida, Y., Guanter, L. & Middleton, E.M. 2016, 'New methods for the retrieval of chlorophyll red fluorescence from hyperspectral satellite instruments: simulations and application to GOME-2 and SCIAMACHY', *Atmospheric Measurement Techniques*, vol. 9, no. 8.

Kanniah, K., Beringer, J., Hutley, L., Tapper, N. & Zhu, X. 2009, 'Evaluation of Collections 4 and 5 of the MODIS Gross Primary Productivity product and algorithm improvement at a tropical savanna site in northern Australia', *Remote Sensing of Environment*, vol. 113, no. 9, pp. 1808-22.

Kato, T., Kobayashi, H., Sakai, Y., Noda, H., Miyauchi, T., Nasahara, K., Akitsu, T., Murayama, S. & Muraoka, H. 2018, 'Bottom-up and top-down approach investigations on solar induced fluorescence for estimating the photosynthesis at ecosystem scale by both ground-based measurement and modeling', *AGU Fall Meeting Abstracts*.

Kato, T., Tsujimoto, K., Nasahara, K., Akitsu, T., Murayama, S., Noda, H. & Muraoka, H. 2016, 'Detection of upward and downward Solar-induced chlorophyll fluorescence emissions at the forest floor in a cool-temperate deciduous broadleaf forest in Japan', *AGU Fall Meeting Abstracts*.

Kempeneers, P., Zarco-Tejada, P.J., North, P.R., de Backer, S., Delalieux, S., Sepulcre-Cantó, G., Morales, F., Van Aardt, J., Sagardoy, R. & Coppin, P. 2008, 'Model inversion for chlorophyll estimation in open canopies from hyperspectral imagery', *International Journal of Remote Sensing*, vol. 29, no. 17-18, pp. 5093-111.

Klosterman, S., Hufkens, K., Gray, J., Melaas, E., Sonnentag, O., Lavine, I., Mitchell, L., Norman, R., Friedl, M. & Richardson, A. 2014, 'Evaluating remote sensing of deciduous forest phenology at multiple spatial scales using PhenoCam imagery'.

Knyazikhin, Y., Martonchik, J.V., Myneni, R.B., Diner, D.J. & Running, S.W. 1998, 'Synergistic algorithm for estimating vegetation canopy leaf area index and fraction of absorbed photosynthetically active radiation from MODIS and MISR data', *Journal of Geophysical Research: Atmospheres*, vol. 103, no. D24, pp. 32257-75.

Kobayashi, H., Baldocchi, D.D., Ryu, Y., Chen, Q., Ma, S., Osuna, J.L. & Ustin, S.L. 2012, 'Modeling energy and carbon fluxes in a heterogeneous oak woodland: A three-dimensional approach', *Agricultural and Forest Meteorology*, vol. 152, pp. 83-100.

Kobayashi, H. & Iwabuchi, H. 2008, 'A coupled 1-D atmosphere and 3-D canopy radiative transfer model for canopy reflectance, light environment, and photosynthesis simulation in a heterogeneous landscape', *Remote Sensing of Environment*, vol. 112, no. 1, pp. 173-85.

Kobayashi, H., Suzuki, R. & Kobayashi, S. 2007, 'Reflectance seasonality and its relation to the canopy leaf area index in an eastern Siberian larch forest: Multi-satellite data and radiative transfer analyses', *Remote Sensing of Environment*, vol. 106, no. 2, pp. 238-52.

Koffi, E., Rayner, P., Norton, A., Frankenberg, C. & Scholze, M. 2015, 'Investigating the usefulness of satellite-derived fluorescence data in inferring gross primary productivity within the carbon cycle data assimilation system', *Biogeosciences*, vol. 12, no. 13, pp. 4067-84.

Köhler, P., Frankenberg, C., Magney, T.S., Guanter, L., Joiner, J. & Landgraf, J. 2018, 'Global Retrievals of Solar-Induced Chlorophyll Fluorescence With TROPOMI: First Results and Intersensor Comparison to OCO-2', *Geophysical Research Letters*, vol. 45, no. 19, pp. 10,456-10,63.

Köhler, P., Guanter, L. & Joiner, J. 2015a, 'A linear method for the retrieval of sun-induced chlorophyll fluorescence from GOME-2 and SCIAMACHY data', *Atmospheric Measurement Techniques*, vol. 8, no. 6, pp. 2589-608.

Köhler, P., Guanter, L. & Joiner, J. 2015b, 'A linear method for the retrieval of sun-induced chlorophyll fluorescence from GOME-2 and SCIAMACHY data'.

Köhler, P., Guanter, L., Kobayashi, H., Walther, S. & Yang, W. 2018, 'Assessing the potential of sun-induced fluorescence and the canopy scattering coefficient to track large-scale vegetation dynamics in Amazon forests', *Remote Sensing of Environment*, vol. 204, pp. 769-85.

Kottek, M., Grieser, J., Beck, C., Rudolf, B. & Rubel, F. 2006, 'World map of the Köppen-Geiger climate classification updated', *Meteorologische Zeitschrift*, vol. 15, no. 3, pp. 259-63.

Lalic, B. & Mihailovic, D.T. 2004, 'An empirical relation describing leaf-area density inside the forest for environmental modeling', *Journal of Applied Meteorology*, vol. 43, no. 4, pp. 641-5.

Lee, J.-E., Frankenberg, C., Tol, C.v.d., Berry, J.A., Guanter, L., Boyce, C.K., Fisher, J.B., Morrow, E., Worden, J.R., Asefi, S., Badgley, G. & Saatchi, S. 2013, 'Forest productivity and water stress in Amazonia: observations from GOSAT chlorophyll fluorescence', *Proceedings of the Royal Society B: Biological Sciences*, vol. 280, no. 1761, p. 20130171.

Li, X. & Xiao, J. 2019, 'A Global, 0.05-Degree Product of Solar-Induced Chlorophyll Fluorescence Derived from OCO-2, MODIS, and Reanalysis Data', *Remote Sensing*, vol. 11, no. 5, p. 517.

Li, X., Xiao, J. & He, B. 2018a, 'Chlorophyll fluorescence observed by OCO-2 is strongly related to gross primary productivity estimated from flux towers in temperate forests', *Remote Sensing of Environment*, vol. 204, pp. 659-71.

Li, X., Xiao, J. & He, B. 2018b, 'Higher absorbed solar radiation partly offset the negative effects of water stress on the photosynthesis of Amazon forests during the 2015 drought', *Environmental Research Letters*, vol. 13, no. 4, p. 044005.

Li, X., Xiao, J., He, B., Altaf Arain, M., Beringer, J., Desai, A.R., Emmel, C., Hollinger, D.Y., Krasnova, A. & Mammarella, I. 2018, 'Solar - induced chlorophyll fluorescence is strongly correlated with terrestrial photosynthesis for a wide

variety of biomes: First global analysis based on OCO - 2 and flux tower observations', *Global change biology*, vol. 24, no. 9, pp. 3990-4008.

Liu, L., Liu, X., Wang, Z. & Zhang, B. 2016, 'Measurement and analysis of bidirectional SIF emissions in wheat canopies', *IEEE Transactions on Geoscience and Remote Sensing*, vol. 54, no. 5, pp. 2640-51.

Liu, Y., Liu, R. & Chen, J.M. 2012, 'Retrospective retrieval of long-term consistent global leaf area index (1981–2011) from combined AVHRR and MODIS data', *Journal of Geophysical Research: Biogeosciences*, vol. 117, no. G4.

Lloyd, J. & Taylor, J. 1994, 'On the temperature dependence of soil respiration', *Functional ecology*, pp. 315-23.

LONG, S.P. 1991, 'Modification of the response of photosynthetic productivity to rising temperature by atmospheric CO2 concentrations: Has its importance been underestimated?', *Plant, Cell & Environment*, vol. 14, no. 8, pp. 729-39.

MacArthur, A., Robinson, I., Rossini, M., Davis, N. & MacDonald, K. 2014, 'A dual-field-of-view spectrometer system for reflectance and fluorescence measurements (Piccolo Doppio) and correction of etaloning', *Proceedings of the Fifth International Workshop on Remote Sensing of Vegetation Fluorescence*, pp. 22-4.

Magnani, F., Mencuccini, M., Borghetti, M., Berbigier, P., Berninger, F., Delzon, S., Grelle, A., Hari, P., Jarvis, P.G. & Kolari, P. 2007, 'The human footprint in the carbon cycle of temperate and boreal forests', *Nature*, vol. 447, no. 7146, p. 849.

Magney, T.S., Bowling, D.R., Logan, B.A., Grossmann, K., Stutz, J., Blanken, P.D., Burns, S.P., Cheng, R., Garcia, M.A. & Köhler, P. 2019, 'Mechanistic evidence for tracking the seasonality of photosynthesis with solar-induced fluorescence', *Proceedings of the National Academy of Sciences*, vol. 116, no. 24, pp. 11640-5.

Majer, P., Neugart, S., Krumbein, A., Schreiner, M. & Hideg, É. 2014, 'Singlet oxygen scavenging by leaf flavonoids contributes to sunlight acclimation in Tilia platyphyllos', *Environmental and Experimental Botany*, vol. 100, pp. 1-9.

McGaughey, R.J. 2009, 'FUSION/LDV: Software for LIDAR data analysis and visualization', *US Department of Agriculture, Forest Service, Pacific Northwest Research Station: Seattle, WA, USA*, vol. 123, no. 2.

Mercado, L.M., Bellouin, N., Sitch, S., Boucher, O., Huntingford, C., Wild, M. & Cox, P.M. 2009, 'Impact of changes in diffuse radiation on the global land carbon sink', *Nature*, vol. 458, no. 7241, p. 1014.

Meroni, M., Busetto, L., Colombo, R., Guanter, L., Moreno, J. & Verhoef, W. 2010, 'Performance of Spectral Fitting Methods for vegetation fluorescence quantification', *Remote Sensing of Environment*, vol. 114, no. 2, pp. 363-74.

Meroni, M. & Colombo, R. 2006, 'Leaf level detection of solar induced chlorophyll fluorescence by means of a subnanometer resolution spectroradiometer', *Remote Sensing of Environment*, vol. 103, no. 4, pp. 438-48.

Meroni, M., Rossini, M., Guanter, L., Alonso, L., Rascher, U., Colombo, R. & Moreno, J. 2009, 'Remote sensing of solar-induced chlorophyll fluorescence: Review of methods and applications', *Remote Sensing of Environment*, vol. 113, no. 10, pp. 2037-51.

Miao, G., Guan, K., Yang, X., Bernacchi, C.J., Berry, J.A., DeLucia, E.H., Wu, J., Moore, C.E., Meacham, K. & Cai, Y. 2018, 'Sun - Induced Chlorophyll Fluorescence, Photosynthesis, and Light Use Efficiency of a Soybean Field from Seasonally Continuous Measurements', *Journal of Geophysical Research: Biogeosciences*, vol. 123, no. 2, pp. 610-23.

Migliavacca, M., Perez - Priego, O., Rossini, M., El - Madany, T.S., Moreno, G., van der Tol, C., Rascher, U., Berninger, A., Bessenbacher, V. & Burkart, A. 2017, 'Plant functional traits and canopy structure control the relationship between photosynthetic CO 2 uptake and far - red sun - induced fluorescence in a Mediterranean grassland under different nutrient availability', *New Phytologist*, vol. 214, no. 3, pp. 1078-91.

Miller, J., Berger, M., Goulas, Y., Jacquemond, S., Loius, J., Mohammed, G., Moise, N., Moreno, J., Moya, I. & Pedrós, R. 2005, *Development of a vegetation fluorescence canopy model*, ESA Scientific and Technical Publications Branch, ESTEC.

Misson, L., Baldocchi, D., Black, T., Blanken, P., Brunet, Y., Yuste, J.C., Dorsey, J., Falk, M., Granier, A. & Irvine, M. 2007, 'Partitioning forest carbon fluxes with overstory and understory eddy-covariance measurements: A synthesis based on FLUXNET data', *Agricultural and Forest Meteorology*, vol. 144, no. 1-2, pp. 14-31.

Monteith, J. 1972, 'Solar radiation and productivity in tropical ecosystems', *Journal of applied ecology*, vol. 9, no. 3, pp. 747-66.

Monteith, J.L. 1977, 'Climate and the efficiency of crop production in Britain', *Philosophical Transactions of the Royal Society of London. B, Biological Sciences*, vol. 281, no. 980, pp. 277-94.

Moore, C.E., Beringer, J., Donohue, R.J., Evans, B., Exbrayat, J.F., Hutley, L.B. & Tapper, N.J. 2018, 'Seasonal, interannual and decadal drivers of tree and grass productivity in an Australian tropical savanna', *Global change biology*, vol. 24, no. 6, pp. 2530-44.

Moore, C.E., Beringer, J., Evans, B., Hutley, L.B., McHugh, I. & Tapper, N.J. 2016, 'The contribution of trees and grasses to productivity of an Australian tropical savanna', *Biogeosciences*, vol. 13, no. 8, pp. 2387-403.

Moya, I., Camenen, L., Evain, S., Goulas, Y., Cerovic, Z.G., Latouche, G., Flexas, J. & Ounis, A. 2004, 'A new instrument for passive remote sensing: 1. Measurements of sunlight-induced chlorophyll fluorescence', *Remote Sensing of Environment*, vol. 91, no. 2, pp. 186-97.

Myneni, R., Knyazikhin, Y. & Park, T. 2016, 'MOD15A2H MODIS Leaf Area Index/FPAR 8-Day L4 Global 500m SIN Grid V006. NASA EOSDIS Land Processes DAAC'.

Myneni, R.B., Ross, J. & Asrar, G. 1989, 'A review on the theory of photon transport in leaf canopies', *Agricultural and Forest Meteorology*, vol. 45, no. 1, pp. 1-153.

Nakaji, T., Ide, R., Oguma, H., Saigusa, N. & Fujinuma, Y. 2007, 'Utility of spectral vegetation index for estimation of gross CO2 flux under varied sky conditions', *Remote Sensing of Environment*, vol. 109, no. 3, pp. 274-84.

Nakaji, T., Kosugi, Y., Takanashi, S., Niiyama, K., Noguchi, S., Tani, M., Oguma, H., Nik, A.R. & Kassim, A.R. 2014, 'Estimation of light-use efficiency through a combinational use of the photochemical reflectance index and vapor pressure deficit in an evergreen tropical rainforest at Pasoh, Peninsular Malaysia', *Remote sensing of environment*, vol. 150, pp. 82-92.

Nichol, C.J., Drolet, G., Porcar-Castell, A., Wade, T., Sabater, N., Middleton, E.M., MacLellan, C., Levula, J., Mammarella, I. & Vesala, T. 2019, 'Diurnal and Seasonal Solar Induced Chlorophyll Fluorescence and Photosynthesis in a Boreal Scots Pine Canopy', *Remote Sensing*, vol. 11, no. 3, p. 273.

Olioso, A., Méthy, M. & Lacaze, B. 1992, 'Simulation of canopy fluorescence as a function of canopy structure and leaf fluorescence', *Remote Sensing of Environment*, vol. 41, no. 2, pp. 239-47.

Paul-Limoges, E., Damm, A., Hueni, A., Liebisch, F., Eugster, W., Schaepman, M.E. & Buchmann, N. 2018, 'Effect of environmental conditions on sun-induced fluorescence in a mixed forest and a cropland', *Remote Sensing of Environment*, vol. 219, pp. 310-23.

Pearcy, R.W. 1990, 'Sunflecks and photosynthesis in plant canopies', *Annual review of plant biology*, vol. 41, no. 1, pp. 421-53.

Pedrós, R., Goulas, Y., Jacquemoud, S., Louis, J. & Moya, I. 2010, 'FluorMODleaf: A new leaf fluorescence emission model based on the PROSPECT model', *Remote Sensing of Environment*, vol. 114, no. 1, pp. 155-67.

Penuelas, J., Filella, I. & Gamon, J.A. 1995, 'Assessment of photosynthetic radiation-use efficiency with spectral reflectance', *New Phytologist*, vol. 131, no. 3, pp. 291-6.

Pinto, F., Damm, A., Schickling, A., Panigada, C., Cogliati, S., Müller-Linow, M., Balvora, A. & Rascher, U. 2016, 'Sun-induced chlorophyll fluorescence from high-resolution imaging spectroscopy data to quantify spatio-temporal patterns of photosynthetic function in crop canopies', *Plant, cell & environment*, vol. 39, no. 7, pp. 1500-12.

Pitkänen, J., Maltamo, M., Hyyppä, J. & Yu, X. 2004, 'Adaptive methods for individual tree detection on airborne laser based canopy height model', *International Archives of Photogrammetry, Remote Sensing and Spatial Information Sciences*, vol. 36, no. 8, pp. 187-91.

Porcar-Castell, A., Tyystjärvi, E., Atherton, J., Van der Tol, C., Flexas, J., Pfündel, E.E., Moreno, J., Frankenberg, C. & Berry, J.A. 2014, 'Linking chlorophyll a fluorescence to photosynthesis for remote sensing applications: mechanisms and challenges', *Journal of experimental botany*, vol. 65, no. 15, pp. 4065-95.

Rascher, U., Alonso, L., Burkart, A., Cilia, C., Cogliati, S., Colombo, R., Damm, A., Drusch, M., Guanter, L., Hanus, J., Hyvärinen, T., Julitta, T., Jussila, J., Kataja, K., Kokkalis, P., Kraft, S., Kraska, T., Matveeva, M., Moreno, J., Muller, O., Panigada, C., Pikl, M., Pinto, F., Prey, L., Pude, R., Rossini, M., Schickling, A., Schurr, U., Schüttemeyer, D., Verrelst, J. & Zemek, F. 2015, 'Sun-induced

fluorescence – a new probe of photosynthesis: First maps from the imaging spectrometer HyPlant', *Global Change Biology*, vol. 21, no. 12, pp. 4673-84.

Rascher, U., Gioli, B. & Miglietta, F. 2008, 'FLEX—fluorescence explorer: a remote sensing approach to quantify spatio-temporal variations of photosynthetic efficiency from space', *Photosynthesis. Energy from the Sun*, Springer, pp. 1387-90.

Rasmussen, M. & Minteer, S.D. 2014, 'Photobioelectrochemistry: solar energy conversion and biofuel production with photosynthetic catalysts', *Journal of The Electrochemical Society*, vol. 161, no. 10, pp. H647-H55.

Reddy, V., Baker, D. & Hodges, H. 1991, 'Temperature effects on cotton canopy growth, photosynthesis, and respiration', *Agronomy Journal*, vol. 83, no. 4, pp. 699-704.

Reichstein, M., Ciais, P., Papale, D., Valentini, R., Running, S., Viovy, N., Cramer, W., Granier, A., Ogee, J. & Allard, V. 2007, 'Reduction of ecosystem productivity and respiration during the European summer 2003 climate anomaly: a joint flux tower, remote sensing and modelling analysis', *Global Change Biology*, vol. 13, no. 3, pp. 634-51.

Reichstein, M., Falge, E., Baldocchi, D., Papale, D., Aubinet, M., Berbigier, P., Bernhofer, C., Buchmann, N., Gilmanov, T. & Granier, A. 2005, 'On the separation of net ecosystem exchange into assimilation and ecosystem respiration: review and improved algorithm', *Global Change Biology*, vol. 11, no. 9, pp. 1424-39.

Richardson, A.D., Black, T.A., Ciais, P., Delbart, N., Friedl, M.A., Gobron, N., Hollinger, D.Y., Kutsch, W.L., Longdoz, B., Luyssaert, S., Migliavacca, M., Montagnani, L., Munger, J.W., Moors, E., Piao, S., Rebmann, C., Reichstein, M., Saigusa, N., Tomelleri, E., Vargas, R. & Varlagin, A. 2010, 'Influence of spring and autumn phenological transitions on forest ecosystem productivity', *Philosophical Transactions of the Royal Society B: Biological Sciences*, vol. 365, no. 1555, pp. 3227-46.

Rosema, A., Snel, J., Zahn, H., Buurmeijer, W. & Van Hove, L. 1998, 'The relation between laser-induced chlorophyll fluorescence and photosynthesis', *Remote sensing of environment*, vol. 65, no. 2, pp. 143-54.

Rosema, A., Verhoef, W., Schroote, J. & Snel, J.F.H. 1991, 'Simulating fluorescence light-canopy interaction in support of laser-induced fluorescence measurements', *Remote Sensing of Environment*, vol. 37, no. 2, pp. 117-30.

Rosenzweig, C., Iglesias, A., Yang, X.-B., Epstein, P.R. & Chivian, E. 2001, 'Climate change and extreme weather events; implications for food production, plant diseases, and pests', *Global change & human health*, vol. 2, no. 2, pp. 90-104.

Rubel, F., Brugger, K., Haslinger, K. & Auer, I. 2017, 'The climate of the European Alps: Shift of very high resolution Köppen-Geiger climate zones 1800–2100', *Meteorologische Zeitschrift*, vol. 26, no. 2, pp. 115-25.

Running, S.W., Nemani, R.R., Heinsch, F.A., Zhao, M., Reeves, M. & Hashimoto, H. 2004, 'A continuous satellite-derived measure of global terrestrial primary production', *Bioscience*, vol. 54, no. 6, pp. 547-60.

Running, S.W., Thornton, P.E., Nemani, R. & Glassy, J.M. 2000, 'Global terrestrial gross and net primary productivity from the Earth Observing System', *Methods in ecosystem science*, Springer, pp. 44-57.

Ryu, Y., Berry, J.A. & Baldocchi, D.D. 2019, 'What is global photosynthesis? History, uncertainties and opportunities', *Remote Sensing of Environment*, vol. 223, pp. 95-114.

Ryu, Y., Sonnentag, O., Nilson, T., Vargas, R., Kobayashi, H., Wenk, R. & Baldocchi, D.D. 2010, 'How to quantify tree leaf area index in an open savanna ecosystem: A multi-instrument and multi-model approach', *Agricultural and Forest Meteorology*, vol. 150, no. 1, pp. 63-76.

Schimel, D., Pavlick, R., Fisher, J.B., Asner, G.P., Saatchi, S., Townsend, P., Miller, C., Frankenberg, C., Hibbard, K. & Cox, P. 2015, 'Observing terrestrial ecosystems and the carbon cycle from space', *Global Change Biology*, vol. 21, no. 5, pp. 1762-76.

Schlau-Cohen, G.S. & Berry, J. 2015, 'Photosynthetic fluorescence, from molecule to planet', *Physics Today*, vol. 68, no. 66.

Shan, N., Ju, W., Migliavacca, M., Martini, D., Guanter, L., Chen, J., Goulas, Y. & Zhang, Y. 2019, 'Modeling canopy conductance and transpiration from solar-induced chlorophyll fluorescence', *Agricultural and Forest Meteorology*, vol. 268, pp. 189-201.

Shiklomanov, A.N., Dietze, M.C., Viskari, T., Townsend, P.A. & Serbin, S.P. 2016, 'Quantifying the influences of spectral resolution on uncertainty in leaf trait estimates through a Bayesian approach to RTM inversion', *Remote sensing of environment*, vol. 183, pp. 226-38.

Shinkarev, V.P. & Govindjee 1993, 'Insight into the relationship of chlorophyll a fluorescence yield to the concentration of its natural quenchers in oxygenic photosynthesis', *Proceedings of the National Academy of Sciences*, vol. 90, no. 16, pp. 7466-9.

Simard, M., Pinto, N., Fisher, J.B. & Baccini, A. 2011, 'Mapping forest canopy height globally with spaceborne lidar', *Journal of Geophysical Research: Biogeosciences*, vol. 116, no. G4.

Sims, D.A., Rahman, A.F., Cordova, V.D., El-Masri, B.Z., Baldocchi, D.D., Bolstad, P.V., Flanagan, L.B., Goldstein, A.H., Hollinger, D.Y. & Misson, L. 2008, 'A new model of gross primary productivity for North American ecosystems based solely on the enhanced vegetation index and land surface temperature from MODIS', *Remote sensing of Environment*, vol. 112, no. 4, pp. 1633-46.

Smith, W., Biederman, J., Scott, R., Moore, D., He, M., Kimball, J., Yan, D., Hudson, A., Barnes, M. & MacBean, N. 2018, 'Chlorophyll fluorescence better captures seasonal and interannual gross primary productivity dynamics across dryland ecosystems of southwestern North America', *Geophysical Research Letters*, vol. 45, no. 2, pp. 748-57.

Song, L., Guanter, L., Guan, K., You, L., Huete, A., Ju, W. & Zhang, Y. 2018a, 'Satellite sun-induced chlorophyll fluorescence detects early response of winter wheat to heat stress in the Indian Indo-Gangetic Plains', *Global change biology*, vol. 24, no. 9, pp. 4023-37.

Song, L., Guanter, L., Guan, K., You, L., Huete, A., Ju, W. & Zhang, Y. 2018b, 'Satellite sun-induced chlorophyll fluorescence detects early response of winter wheat to heat stress in the Indian Indo-Gangetic Plains', *Global change biology*.

Stenberg, P., Mõttus, M. & Rautiainen, M. 2016, 'Photon recollision probability in modelling the radiation regime of canopies — A review', *Remote Sensing of Environment*, vol. 183, pp. 98-108.

Stöckli, R., Rutishauser, T., Dragoni, D., O'keefe, J., Thornton, P., Jolly, M., Lu, L. & Denning, A. 2008, 'Remote sensing data assimilation for a prognostic phenology model', *Journal of Geophysical Research: Biogeosciences*, vol. 113, no. G4.

Sun, Y., Frankenberg, C., Jung, M., Joiner, J., Guanter, L., Köhler, P. & Magney, T. 2018, 'Overview of Solar-Induced chlorophyll Fluorescence (SIF) from the Orbiting

Carbon Observatory-2: Retrieval, cross-mission comparison, and global monitoring for GPP', *Remote sensing of environment*, vol. 209, pp. 808-23.

Sun, Y., Frankenberg, C., Wood, J.D., Schimel, D.S., Jung, M., Guanter, L., Drewry, D., Verma, M., Porcar-Castell, A. & Griffis, T.J. 2017, 'OCO-2 advances photosynthesis observation from space via solar-induced chlorophyll fluorescence', *Science*, vol. 358, no. 6360, p. eaam5747.

Sun, Y., Fu, R., Dickinson, R., Joiner, J., Frankenberg, C., Gu, L., Xia, Y. & Fernando, N. 2015a, 'Drought onset mechanisms revealed by satellite solar-induced chlorophyll fluorescence: Insights from two contrasting extreme events', *Journal of Geophysical Research: Biogeosciences*, vol. 120, no. 11, pp. 2427-40.

Sun, Y., Fu, R., Dickinson, R., Joiner, J., Frankenberg, C., Gu, L., Xia, Y. & Fernando, N. 2015b, 'Drought onset mechanisms revealed by satellite solar - induced chlorophyll fluorescence: Insights from two contrasting extreme events', *Journal of Geophysical Research: Biogeosciences*, vol. 120, no. 11, pp. 2427-40.

Tol, C., Verhoef, W., Timmermans, J., Verhoef, A. & Su, Z. 2009, 'An integrated model of soil-canopy spectral radiances, photosynthesis, fluorescence, temperature and energy balance', *Biogeosciences*, vol. 6, no. 12, pp. 3109-29.

Turner, D.P., Ritts, W.D., Cohen, W.B., Gower, S.T., Running, S.W., Zhao, M., Costa, M.H., Kirschbaum, A.A., Ham, J.M. & Saleska, S.R. 2006, 'Evaluation of MODIS NPP and GPP products across multiple biomes', *Remote sensing of environment*, vol. 102, no. 3-4, pp. 282-92.

Turner, D.P., Ritts, W.D., Cohen, W.B., Gower, S.T., Zhao, M., Running, S.W., Wofsy, S.C., Urbanski, S., Dunn, A.L. & Munger, J. 2003, 'Scaling gross primary production (GPP) over boreal and deciduous forest landscapes in support of MODIS GPP product validation', *Remote Sensing of Environment*, vol. 88, no. 3, pp. 256-70.

Van der Tol, C., Berry, J., Campbell, P. & Rascher, U. 2014, 'Models of fluorescence and photosynthesis for interpreting measurements of solar - induced chlorophyll fluorescence', *Journal of Geophysical Research: Biogeosciences*, vol. 119, no. 12, pp. 2312-27.

Van der Tol, C., Verhoef, W., Timmermans, J., Verhoef, A. & Su, Z. 2009, 'An integrated model of soil-canopy spectral radiances, photosynthesis, fluorescence, temperature and energy balance', *Biogeosciences*, vol. 6, no. 12, pp. 3109-29.

Van Wittenberghe, S., Alonso, L., Verrelst, J., Moreno, J. & Samson, R. 2015, 'Bidirectional sun-induced chlorophyll fluorescence emission is influenced by leaf structure and light scattering properties—A bottom-up approach', *Remote Sensing of Environment*, vol. 158, pp. 169-79.

Verhoef, W. 1998, *Theory of radiative transfer models applied in optical remote sensing of vegetation canopies*.

Verhoef, W. 2011, 'Modelling vegetation fluorescence observations', *7th EARSEL workshop of the Special Interest Group in imaging spectroscopy: final programme, 11-13 April 2011, Edinburgh, UK*.

Verma, M., Schimel, D., Evans, B., Frankenberg, C., Beringer, J., Drewry, D.T., Magney, T., Marang, I., Hutley, L. & Moore, C. 2017, 'Effect of environmental conditions on the relationship between solar - induced fluorescence and gross primary productivity at an OzFlux grassland site', *Journal of Geophysical Research: Biogeosciences*, vol. 122, no. 3, pp. 716-33.

Verrelst, J., Muñoz, J., Alonso, L., Delegido, J., Rivera, J.P., Camps-Valls, G. & Moreno, J. 2012, 'Machine learning regression algorithms for biophysical parameter retrieval: Opportunities for Sentinel-2 and-3', *Remote Sensing of Environment*, vol. 118, pp. 127-39.

Verrelst, J., van der Tol, C., Magnani, F., Sabater, N., Rivera, J.P., Mohammed, G. & Moreno, J. 2016, 'Evaluating the predictive power of sun-induced chlorophyll fluorescence to estimate net photosynthesis of vegetation canopies: A SCOPE modeling study', *Remote Sensing of Environment*, vol. 176, pp. 139-51.

Vilfan, N., Van der Tol, C., Muller, O., Rascher, U. & Verhoef, W. 2016, 'Fluspect-B: A model for leaf fluorescence, reflectance and transmittance spectra', *Remote sensing of environment*, vol. 186, pp. 596-615.

Walker, J. & Gillison, A. 1982, 'Australian savannas', *Ecology of tropical savannas*, Springer, pp. 5-24.

Walther, S., Duveiller, G., Jung, M., Guanter, L., Cescatti, A. & Camps - Valls, G. 2019, 'Satellite Observations of the Contrasting Response of Trees and Grasses to Variations in Water Availability', *Geophysical Research Letters*, vol. 46, no. 3, pp. 1429-40.

Walther, S., Voigt, M., Thum, T., Gonsamo, A., Zhang, Y., Köhler, P., Jung, M., Varlagin, A. & Guanter, L. 2016, 'Satellite chlorophyll fluorescence measurements reveal

large-scale decoupling of photosynthesis and greenness dynamics in boreal evergreen forests', *Global Change Biology*, vol. 22, no. 9, pp. 2979-96.

Wang, C., Beringer, J., Hutley, L.B., Cleverly, J., Li, J., Liu, Q. & Sun, Y. 2019, 'Phenology Dynamics of Dryland Ecosystems Along the North Australian Tropical Transect Revealed by Satellite Solar-Induced Chlorophyll Fluorescence', *Geophysical Research Letters*, vol. 46, no. 10, pp. 5294-302.

Wang, S., Huang, C., Zhang, L., Lin, Y., Cen, Y. & Wu, T. 2016, 'Monitoring and assessing the 2012 drought in the Great Plains: analyzing satellite-retrieved solar-induced chlorophyll fluorescence, drought indices, and gross primary production', *Remote Sensing*, vol. 8, no. 2, p. 61.

Wang, Y., Tian, Y., Zhang, Y., El-Saleous, N., Knyazikhin, Y., Vermote, E. & Myneni, R.B. 2001, 'Investigation of product accuracy as a function of input and model uncertainties: Case study with SeaWiFS and MODIS LAI/FPAR algorithm', *Remote Sensing of Environment*, vol. 78, no. 3, pp. 299-313.

Watson, R.T., Noble, I.R., Bolin, B., Ravindranath, N., Verardo, D.J. & Dokken, D.J. 2000, *Land use, land-use change and forestry: a special report of the Intergovernmental Panel on Climate Change*, Cambridge University Press.

WHITE, M.A., De BEURS, K.M., DIDAN, K., INOUYE, D.W., RICHARDSON, A.D., JENSEN, O.P., O'KEEFE, J., ZHANG, G., NEMANI, R.R., Van LEEUWEN, W.J.D., BROWN, J.F., De WIT, A., SCHAEPMAN, M., LIN, X., DETTINGER, M., BAILEY, A.S., KIMBALL, J., SCHWARTZ, M.D., BALDOCCHI, D.D., LEE, J.T. & LAUENROTH, W.K. 2009, 'Intercomparison, interpretation, and assessment of spring phenology in North America estimated from remote sensing for 1982–2006', *Global Change Biology*, vol. 15, no. 10, pp. 2335-59.

Whitley, R.J., MACINNIS-NG, C.M., Hutley, L.B., Beringer, J., Zeppel, M., Williams, M., Taylor, D. & Eamus, D. 2011, 'Is productivity of mesic savannas light limited or water limited? Results of a simulation study', *Global Change Biology*, vol. 17, no. 10, pp. 3130-49.

Wieneke, S., Burkart, A., Cendrero-Mateo, M., Julitta, T., Rossini, M., Schickling, A., Schmidt, M. & Rascher, U. 2018a, 'Linking photosynthesis and sun-induced fluorescence at sub-daily to seasonal scales', *Remote Sensing of Environment*, vol. 219, pp. 247-58.

Wieneke, S., Burkart, A., Cendrero-Mateo, M.P., Julitta, T., Rossini, M., Schickling, A., Schmidt, M. & Rascher, U. 2018b, 'Diurnal and seasonal patterns of photosynthesis and its relationship to F687, F760 and a revised PRI', *EGU General Assembly Conference Abstracts*, vol. 20, p. 14562.

Wieneke, S., Burkart, A., Cendrero-Mateo, M.P., Julitta, T., Rossini, M., Schickling, A., Schmidt, M. & Rascher, U. 2018c, 'Linking photosynthesis and sun-induced fluorescence at sub-daily to seasonal scales', *Remote Sensing of Environment*, vol. 219, pp. 247-58.

Wohlfahrt, G., Gerdel, K., Migliavacca, M., Rotenberg, E., Tatarinov, F., Müller, J., Hammerle, A., Julitta, T., Spielmann, F. & Yakir, D. 2018a, 'Sun-induced fluorescence and gross primary productivity during a heat wave', *Scientific reports*, vol. 8, no. 1, p. 14169.

Wohlfahrt, G., Gerdel, K., Migliavacca, M., Rotenberg, E., Tatarinov, F., Müller, J., Hammerle, A., Julitta, T., Spielmann, F.M. & Yakir, D. 2018b, 'Sun-induced fluorescence and gross primary productivity during a heat wave', *Scientific Reports*, vol. 8, no. 1, p. 14169.

Wu, J., Kobayashi, H., Stark, S.C., Meng, R., Guan, K., Tran, N.N., Gao, S., Yang, W., Restrepo - Coupe, N. & Miura, T. 2018, 'Biological processes dominate seasonality of remotely sensed canopy greenness in an Amazon evergreen forest', *New Phytologist*, vol. 217, no. 4, pp. 1507-20.

Wu, X., Xiao, X., Zhang, Y., He, W., Wolf, S., Chen, J., He, M., Gough, C.M., Qin, Y. & Zhou, Y. 2018, 'Spatiotemporal Consistency of Four Gross Primary Production Products and Solar - Induced Chlorophyll Fluorescence in Response to Climate Extremes Across CONUS in 2012', *Journal of Geophysical Research: Biogeosciences*, vol. 123, no. 10, pp. 3140-61.

Wutzler, T., Lucas-Moffat, A., Migliavacca, M., Knauer, J., Sickel, K., Šigut, L., Menzer, O. & Reichstein, M. 2018, 'Basic and extensible post-processing of eddy covariance flux data with REddyProc', *Biogeosciences Discussions*.

Yang, H., Yang, X., Zhang, Y., Heskel, M.A., Lu, X., Munger, J.W., Sun, S. & Tang, J. 2017, 'Chlorophyll fluorescence tracks seasonal variations of photosynthesis from leaf to canopy in a temperate forest', *Global change biology*, vol. 23, no. 7, pp. 2874-86.

Yang, K., Ryu, Y., Dechant, B., Berry, J.A., Hwang, Y., Jiang, C., Kang, M., Kim, J., Kimm, H. & Kornfeld, A. 2018, 'Sun-induced chlorophyll fluorescence is more strongly related to absorbed light than to photosynthesis at half-hourly resolution in a rice paddy', *Remote Sensing of Environment*, vol. 216, pp. 658-73.

Yang, P. & Van Der Tol, C. 2018, 'Linking canopy scattering of far-red sun-induced chlorophyll fluorescence with reflectance', *Remote sensing of environment*, vol. 209, pp. 456-67.

Yang, X., Shi, H., Stovall, A., Guan, K., Miao, G., Zhang, Y., Zhang, Y., Xiao, X., Ryu, Y. & Lee, J.-E. 2018, 'FluoSpec 2—An Automated Field Spectroscopy System to Monitor Canopy Solar-Induced Fluorescence', *Sensors*, vol. 18, no. 7, p. 2063.

Yang, X., Tang, J., Mustard, J.F., Lee, J.-E., Rossini, M., Joiner, J., Munger, J.W., Kornfeld, A. & Richardson, A.D. 2015a, 'Solar-induced chlorophyll fluorescence that correlates with canopy photosynthesis on diurnal and seasonal scales in a temperate deciduous forest', *Geophysical Research Letters*, vol. 42, no. 8, pp. 2977-87.

Yang, X., Tang, J., Mustard, J.F., Lee, J.E., Rossini, M., Joiner, J., Munger, J.W., Kornfeld, A. & Richardson, A.D. 2015b, 'Solar-induced chlorophyll fluorescence that correlates with canopy photosynthesis on diurnal and seasonal scales in a temperate deciduous forest', *Geophysical Research Letters*, vol. 42, no. 8, pp. 2977-87.

Yoshida, Y., Joiner, J., Tucker, C., Berry, J., Lee, J.E., Walker, G., Reichle, R., Koster, R., Lyapustin, A. & Wang, Y. 2015, 'The 2010 Russian drought impact on satellite measurements of solar-induced chlorophyll fluorescence: Insights from modeling and comparisons with parameters derived from satellite reflectances', *Remote Sensing of Environment*, vol. 166, pp. 163-77.

Yu, L., Wen, J., Chang, C., Frankenberg, C. & Sun, Y. 2019, 'High-Resolution Global Contiguous SIF of OCO-2', *Geophysical Research Letters*, vol. 46, no. 3, pp. 1449-58.

Zarco-Tejada, P.J., González-Dugo, V. & Berni, J.A.J. 2012, 'Fluorescence, temperature and narrow-band indices acquired from a UAV platform for water stress detection using a micro-hyperspectral imager and a thermal camera', *Remote Sensing of Environment*, vol. 117, pp. 322-37.

Zeng, Y., Badgley, G., Dechant, B., Ryu, Y., Chen, M. & Berry, J.A. 2019, 'A practical approach for estimating the escape ratio of near-infrared solar-induced chlorophyll fluorescence', *Remote Sensing of Environment*.

Zhang, Y., Guanter, L., Berry, J.A., Joiner, J., van der Tol, C., Huete, A., Gitelson, A., Voigt, M. & Köhler, P. 2014, 'Estimation of vegetation photosynthetic capacity from space - based measurements of chlorophyll fluorescence for terrestrial biosphere models', *Global Change Biology*, vol. 20, no. 12, pp. 3727-42.

Zhang, Y., Guanter, L., Berry, J.A., van der Tol, C., Yang, X., Tang, J. & Zhang, F. 2016, 'Model-based analysis of the relationship between sun-induced chlorophyll fluorescence and gross primary production for remote sensing applications', *Remote Sensing of Environment*, vol. 187, pp. 145-55.

Zhang, Y., Joiner, J., Alemohammad, S.H., Zhou, S. & Gentine, P. 2018, 'A global spatially contiguous solar-induced fluorescence (CSIF) dataset using neural networks', *Biogeosciences*, vol. 15, no. 19, pp. 5779-800.

Zhang, Y., Joiner, J., Gentine, P. & Zhou, S. 2018, 'Reduced solar - induced chlorophyll fluorescence from GOME - 2 during Amazon drought caused by dataset artifacts', *Global change biology*, vol. 24, no. 6, pp. 2229-30.

Zhang, Y., Song, C., Band, L.E., Sun, G. & Li, J. 2017, 'Reanalysis of global terrestrial vegetation trends from MODIS products: Browning or greening?', *Remote Sensing of Environment*, vol. 191, pp. 145-55.

Zhang, Y., Xiao, X., Wu, X., Zhou, S., Zhang, G., Qin, Y. & Dong, J. 2017, 'A global moderate resolution dataset of gross primary production of vegetation for 2000–2016', *Scientific data*, vol. 4, p. 170165.

Zhang, Y., Xiao, X., Zhang, Y., Wolf, S., Zhou, S., Joiner, J., Guanter, L., Verma, M., Sun, Y. & Yang, X. 2018, 'On the relationship between sub-daily instantaneous and daily total gross primary production: Implications for interpreting satellite-based SIF retrievals', *Remote sensing of environment*, vol. 205, pp. 276-89.

Zhao, F., Dai, X., Verhoef, W., Guo, Y., van der Tol, C., Li, Y. & Huang, Y. 2016, 'FluorWPS: a Monte Carlo ray-tracing model to compute sun-induced chlorophyll fluorescence of three-dimensional canopy', *Remote sensing of environment*, vol. 187, pp. 385-99.

Zhao, M., Running, S.W. & Nemani, R.R. 2006, 'Sensitivity of Moderate Resolution Imaging Spectroradiometer (MODIS) terrestrial primary production to the

accuracy of meteorological reanalyses', *Journal of Geophysical Research: Biogeosciences*, vol. 111, no. G1.